Single-Molecule Imaging of Cholesterol-Dependent Cytolysin Assembly

A dissertation by

Michael Joseph Senior

Submitted in partial satisfaction

of the requirements for the degree of

Doctor of Philosophy

Linacre College, University of Oxford

Michaelmas 2015

Single-Molecule Imaging of Cholesterol-Dependent Cytolysin Assembly

Michael Joseph Senior,

Linacre College, University of Oxford

Submitted for the degree of Doctor of Philosophy, Michaelmas 2015

Abstract

Cholesterol-dependent cytolysins (CDCs) are amongst the primary virulence factors for several important pathogens. Their typical function is to lyse cells by forming large pores in target membranes, often up to 40 nm in diameter and comprised of around 30-50 subunits. Pores assemble from diffusing monomers bound to the target membrane, via a prepore intermediate. Previous work on the mechanism of pore assembly has focused on structural and ensemble fluorescence information, complemented by atomic force microscopy. The experiments described herein present the application of single-molecule total internal reflection fluorescence microscopy to the study of CDC assembly, using droplet interface bilayers as a felicitous *in vitro* system. This technique supported millisecond temporal resolution imaging of CDC monomers and individual CDC complexes assembling in parallel. The recorded videos enabled quantification of assembly kinetics and further insight into the governing mechanism of assembly.

Acknowledgements

I would like to thank some of the people who have supported me in the course of my DPhil.

Firstly, thank you to Dr Mark Wallace, for presenting at the DTC in the first place, and for accepting me into the lab. I am eternally grateful for your continued guidance and faith over the past few years, and for letting me take advantage of your extensive knowledge of biophysics.

Thank you also to the DTC for accepting me onto your excellent program, and to EPSRC for funding me.

Thank you to the current and former members of the Wallace group, for both your scientific input and friendship. You have made the DPhil experience highly interesting and extremely enjoyable. Special thanks to Bríd, for getting me started, and to Carina, for rereading the thesis and continuing the experiments. Special thanks also to John, for he is a special person.

Thank you to my collaborators Robert Gilbert and Alejandro Heuck, for expert academic support and for particularly enlightening discussions (not to mention the use of facilities and protein samples). Thanks also to Luke and Tao in the Gilbert group, for being patient, and for your vast expertise in molecular biology; it was good fun.

Thank you to my friends for putting it in perspective, in particular the St Mary's crew, the lads who lunch, and the badminton team (especially Chris, who is annoyingly good at sports).

Thank you, so much, to my family. To Helen and Hannah, for bringing more laughter and heated conversation to my life than I can cope with. To Mum, for getting me to where I am, and for always being proud. To Dad, for driving 20 miles before dawn so I could hand my homework in on time, for the most fair and intelligent advice, for being the rock and stability.

Thank you, immeasurably, to Amy, for never letting me lose sight, in work and life. Thank you for the encouragement and for being tolerant. Thank you for all the happiness along the way.

Declaration

The work described in this thesis was carried out between September 2012 and January 2016, in the laboratory of Dr Mark Wallace at the Chemistry Research Laboratory, University of Oxford. All the work described within this thesis is entirely my own. This work has not been submitted previously for any other degree at the University of Oxford or any other university.

Michael J. Senior

January 2016

Contents

1 Introduction **1**

1.1 Cholesterol-dependent cytolysins 3

1.1.1 CDC Pathogenesis 3

1.1.2 The CDC molecular mechanism of assembly 4

1.1.3 Structure influences the assembly mechanism 5

1.1.4 Oligomer-based assembly 8

1.1.5 The MACPF family of proteins 13

1.2 Remaining unknowns 14

1.3 Other pore-forming toxins and their assembly mechanisms 17

1.4 Single-molecule fluorescence to study CDCs 19

1.4.1 Basic principles of sm-fluorescence 20

1.4.2 Applying sm-fluorescence to CDCs 22

1.5 Droplet interface bilayers 23

1.5.1 DIBs as artificial bilayers 23

1.5.2 Alternative artificial bilayers 24

1.5.3 DIB versatility 28

1.6 Key findings from this thesis 29

1.7 Outlook 30

2 Creating a cholesterol-dependent cytolysin sample suitable for single-molecule fluorescence imaging **31**

2.1 Sample considerations . . . 32
2.1.1 Required features of the protein sample . . . 32
2.1.2 Implications for the primary sequence . . . 33
2.2 Cloning recombinant pneumolysin . . . 34
2.2.1 Sequencing the rPLY gene . . . 34
2.2.2 A new vector to aid purification . . . 35
2.2.3 Increasing the volume of DNA . . . 36
2.3 Expression of $rPLY^{his}$ . . . 38
2.3.1 Bacterial culture . . . 38
2.3.2 Expression trial . . . 38
2.4 Purification and labelling . . . 39
2.4.1 Purification by liquid chromatography . . . 39
2.4.2 Labelling trial . . . 44
2.4.3 Labelling and subsequent purification . . . 44
2.4.4 Monitoring protein purity . . . 46
2.5 Characterisation of labelled PLY . . . 46
2.5.1 Confirmation of biological activity . . . 48
2.5.2 Measuring the extent of labelling . . . 50
2.6 Summary of the labelled PLY sample . . . 53

3 Optimising bilayer construction and imaging for the study of cholesterol-dependent cytolysins 54

3.1 Droplet interface bilayer construction . . . 54
3.2 Tuning DIB properties to accommodate CDCs . . . 58
3.2.1 Lipid composition . . . 59
3.2.2 Perfringolysin O . . . 62
3.2.3 Applying protein to the bilayer . . . 65
3.2.4 Droplet solution conditions . . . 66
3.3 Imaging protocol . . . 67

3.4 Validating CDC function in DIBs 69
3.4.1 Electrophysiology protocol 70
3.4.2 Single-channel recordings of pore-forming toxins 72
3.4.3 Optical single-channel recording 75
3.5 Summary 77

4 Recording cholesterol-dependent cytolysin assembly in real time with millisecond temporal resolution 78

4.1 Protein complex detection by smTIRF 78
4.2 Capturing the assembly process 80
4.2.1 Typical features of PFO assembly 80
4.2.2 A concentration sweet spot 83
4.2.3 Comparing insertion events and assembled complexes 84
4.3 Variations on assembly 85
4.3.1 Features of assembly at low 2D protein concentration 85
4.3.2 Features of assembly at high 2D protein concentration 89
4.3.3 PLY assembly 90
4.3.4 Oligomer-based assembly 91
4.4 Photobleaching of CDC complexes 93
4.4.1 Brief introduction to photobleaching 93
4.4.2 Estimating CDC stoichiometry by stepwise photobleaching . . 93
4.4.3 Photobleaching with assembly 96
4.5 Preliminary results from two-colour imaging of oSCRs and labelled monomers 97

5 Quantifying cholesterol-dependent cytolysin assembly 100

5.1 Single particle tracking 100
5.2 Intensity extraction 103
5.3 Estimating stoichiometry of CDC complexes during assembly 105

5.3.1 Photobleaching estimates . . . 106
5.3.2 Tracking of single monomers . . . 107
5.3.3 Verification by steps in assembly traces . . . 109
5.4 Assembly and diffusion of individual CDC complexes . . . 110
5.4.1 Individual stoichiometry traces . . . 110
5.4.2 Diffusion of assembling CDC complexes . . . 112
5.4.3 Resolving steps in assembly . . . 114
5.5 Assembly mechanism . . . 116
5.5.1 Noise from fluorophores accounts for fluctuations in assembly . 116
5.5.2 Timescale of fluctuations in assembly matches monomer diffusion . . . 118
5.5.3 Oligomer-based assembly . . . 121
5.6 Dissecting CDC assembly kinetics . . . 123
5.6.1 Rate of complex appearance . . . 124
5.6.2 Average rate of assembly for a single PFO complex . . . 125
5.6.3 Monomer and oligomer collision rates . . . 129
5.6.4 Stoichiometric evolution of a PFO population . . . 131
5.7 Discussion . . . 133

6 Conclusions **135**

6.1 Summary of results . . . 135
6.2 Interpretation of results . . . 136
6.2.1 DIBs and smTIRF are powerful techniques . . . 136
6.2.2 Insight into CDC assembly mechanism and kinetics . . . 137
6.2.3 Comparison with previous findings . . . 139
6.3 Outlook . . . 140
6.3.1 Mathematical modelling of assembly . . . 140
6.3.2 Simultaneous measurements of function and assembly . . . 141
6.3.3 New techniques for the study of CDCs . . . 141

List of Figures

1.1 Crystal structure of an archetypal cholesterol-dependent cytolysin, perfringolysin O . . . 2
1.2 CDC-producing pathogens . . . 3
1.3 A summary of the CDC molecular mechanism of assembly . . . 5
1.4 Detailed structure of PFO . . . 6
1.5 Identifying the prepore intermediate . . . 7
1.6 Negative-stain EM of CDCs . . . 8
1.7 Reconstructions of the PLY prepore and pore from EM data . . . 9
1.8 Arcs do make holes . . . 11
1.9 Plastic LLO assembly . . . 12
1.10 Commonality between MACPF and CDC proteins . . . 13
1.11 Dynamics of the prepore to pore conversion resolved by AFM . . . 16
1.12 DIB approach to study αHL assembly . . . 18
1.13 αHL exhibits rapid assembly . . . 19
1.14 Essence of a droplet interface bilayer . . . 24
1.15 Alternative artificial bilayers . . . 26

2.1 Molecular weight of the lifted rPLY gene . . . 36
2.2 Amino acid sequence of the cloned $rPLY^{his}$ gene . . . 37
2.3 Expression trial for detection of $rPLY^{his}$ in bacterial culture . . . 39
2.4 Elution profile from several purification steps . . . 43
2.5 Measuring the extent of PEG labelling of $rPLY^{his}$ by SDS-PAGE . . . 45
2.6 Purity of eluate after each chromatographic step . . . 47
2.7 Haemolysis assay demonstrates protein activity . . . 50
2.8 Cy3B-labelled PLY detected by a UV gel . . . 51
2.9 Absorbance spectrum of Cy3B and lPLY . . . 52

3.1 Principles of DIB construction . . . 55
3.2 A bespoke droplet holder . . . 56
3.3 Magnified view of a droplet before and after DIB formation . . . 58
3.4 DOPC and POPC bilayers . . . 60
3.5 PFO characterisation . . . 64
3.6 Haemolysis assay with received PFO sample . . . 65
3.7 Nanolitre injector . . . 66
3.8 Experimental design for imaging CDC assembly . . . 68
3.9 Electrophysiology with a DIB . . . 70
3.10 αHL insertion events . . . 71
3.11 PLY insertion events . . . 73

3.12 PFO insertion events 74
3.13 Optical single-channel recording of αHL and PLY pores 76
3.14 Deconstructing SCCaFT data from a PLY pore 77

4.1 Individual CDC complexes on a DIB, detected by smTIRF 80
4.2 Typical smTIRF recordings of PFO assembly 81
4.3 Resolving single PFO monomers 86
4.4 Time-lapse recording of lPLY assembly 87
4.5 Assembly at low 2D protein concentration 88
4.6 Assembly at high 2D protein concentration 89
4.7 PLY assembly imaged by smTIRF 91
4.8 Oligomer-oligomer assembly 92
4.9 Counting subunits in PFO complexes by stepwise photobleaching . . 96
4.10 Two-colour oSCR and labelled PFO imaging 98

5.1 Frame from smTIRF assembly recording with superposed tracks . . . 102
5.2 Motion of CDC complexes revealed by single particle tracking 103
5.3 Intensity of bright spots estimated by Gaussian approximation 104
5.4 Estimating single-fluorophore intensity by tracking single labelled monomers 108
5.5 Common step-size in assembly traces validates single-fluorophore intensity estimate 109
5.6 Assembly and diffusion of individual CDC complexes 111
5.7 Negative correlation between diffusion and stoichiometry 113
5.8 Detecting steps in individual assembly traces 115
5.9 Fluctuations in assembly are explained by noise from a greater number of fluorophores 117
5.10 Lag time for steps in assembly traces matches monomer diffusion . . . 121
5.11 Quantitative oligomer-oligomer assembly 122
5.12 Rate of complex appearance 125
5.13 Average rate of assembly for a single PFO complex 128
5.14 Fitting the single-complex median assembly curve 129
5.15 Stoichiometric evolution of the *in silico*-synchronised PFO population 132
5.16 Stoichiometric evolution of the PFO population, over real time 133

Acronyms

αHL	α-haemolysin
γHL	γ-haemolysin
a488	Alexa Fluor® 488
a647	Alexa Fluor® 647
AFM	atomic force microscopy
ALO	anthrolysin O
CDC	cholesterol-dependent cytolysin
CNC	computer numerical control
DIB	droplet interface bilayer
DMSO	dimethyl sulfoxide
DOPC	1,2-dioleoyl-*sn*-glycero-3-phosphocholine
DPhPC	1,2-diphytanoyl-*sn*-glycero-3-phosphocholine
DTT	dithiothreitol
EM	electron microscopy
EMCCD	electron multiplying charge-coupled device
IMAC	immobilised metal ion affinity chromatography
IPTG	isopropyl β-D-1-thiogalactopyranoside
LB	Luria-Bertani
LLO	listeriolysin O
lPFO	1:1 labelled recombinant perfringolysin O, $PFO^{C459A,E167C}$-a488
lPFO-a647	1:1 labelled recombinant perfringolysin O, $PFO^{C459A,E167C}$-a647
lPLY	1:1 labelled recombinant pneumolysin, $PLY^{C428A,N\text{-}his\text{-}cys}$-Cy3B
MACPF	membrane attack complex/perforin
MQ	Milli-Q® water
MSD	mean squared displacement
OD	optical density
OPPF	Oxford Protein Production Facility
oSCR	optical single-channel recording
PBS	phosphate-buffered saline
PEG	polyethylene glycol
PFO	perfringolysin O
PFT	pore-forming toxin
PLY	pneumolysin
PMMA	poly(methyl methacrylate)

POPC	1-palmitoyl-2-oleoyl-*sn*-glycero-3-phosphocholine
psf	point spread function
rPFO	recombinant perfringolysin O, PFO^{C459A}
rPLY	recombinant pneumolysin, $PLY^{C428A,N\text{-}cys}$
rPLY^{his}	recombinant pneumolysin with a prepended hexahistidine tag, $PLY^{C428A,N\text{-}his\text{-}cys}$
SCCaFT	single-channel calcium fluorescent transient
SCR	single-channel recording
SDS-AGE	sodium dodecyl sulfate agarose gel electrophoresis
SDS-PAGE	sodium dodecyl sulfate polyacrylamide gel electrophoresis
SEC	size exclusion chromatography
SLB	supported lipid bilayer
SLO	streptolysin O
sm-fluorescence	single-molecule fluorescence
smTIRF	single-molecule total internal reflection fluorescence microscopy
SNR	signal-to-noise ratio
SPT	single-particle tracking
TIRF	total internal reflection fluorescence microscopy
TMH	transmembrane helix
X-Gal	5-bromo-4-chloro-3-indolyl-β-D-galactopyranoside

Chapter 1

Introduction

The cholesterol-dependent cytolysins (CDCs) are a family of proteins whose primary function is to lyse cells. They assemble into large multimeric rings that can puncture holes in target membranes, and in this capacity they are deployed by several genera of bacteria [1], allowing the bacteria to colonise host tissue or evade the immune system, for example [2–6]. Interest in these proteins has been substantial due to their ubiquity in pathogenic bacteria and their intriguing mechanism of pore formation. Investigations of CDCs have involved ensemble fluorescence [5, 7–12], molecular biology [9,12–14], x-ray crystallography (Figure 1.1) [15–19] and electron microscopy (EM) [9, 20–25]. Recently, atomic force microscopy (AFM) has joined this toolbox and deepened our understanding of the pore-forming mechanism [25–27].

Despite this wealth of information, arguably there is still a need for high-resolution, real-time imaging of CDC assembly at a timescale pertinent to oligomerisation. This thesis describes efforts to capture the assembly of CDCs with millisecond temporal resolution and 550 nm spatial resolution (this value is explained in Section 5.5.2). The experiments generated videos of multimeric protein assembly, which enabled quantification of the assembly process in detail.

Chapter 1 provides an introduction to CDC proteins, including their biological function, structure and mechanism of pore formation. The less well-understood

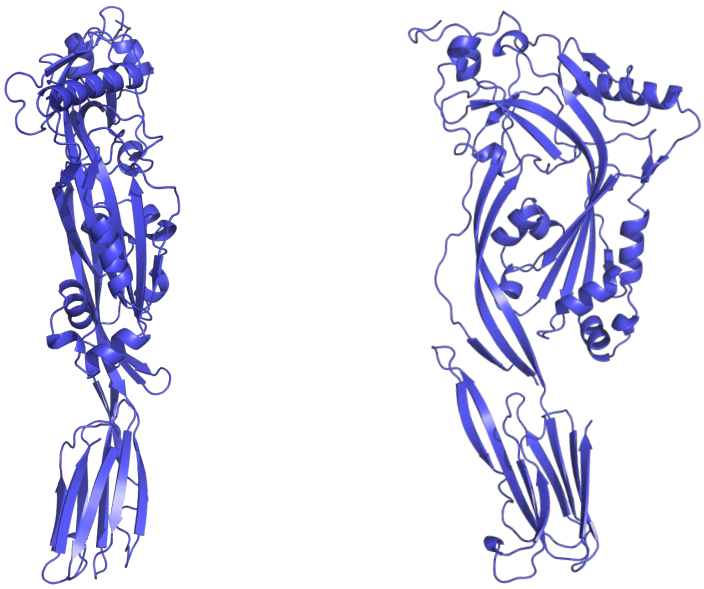


Figure 1.1: Crystal structure of an archetypal cholesterol-dependent cytolysin, perfringolysin O. Two perpendicular views of the molecule are presented, to illustrate its shape. Protein data bank ID: 1PFO [15]. (Further detail is supplied in Figure 1.4.)

features of CDCs are then discussed, along with the motivation for studying their assembly. Example investigations of the assembly of other pore-forming toxins (PFTs) are presented, and the experimental techniques used in this study are introduced, including the reasons for the choice of imaging technique and artificial bilayer system. Finally, key findings from the study are summarised.

Synthesis of a protein sample suitable for imaging is described in Chapter 2. Chapter 3 details an imaging protocol and assessment of functionality for CDCs on an artificial bilayer. Results from imaging CDCs at the single-complex level and with millisecond temporal resolution are presented in Chapter 4, including capture of CDC assembly. Chapter 5 describes the quantification of assembly kinetics and interpretation of the assembly mechanism based on videos of assembly.

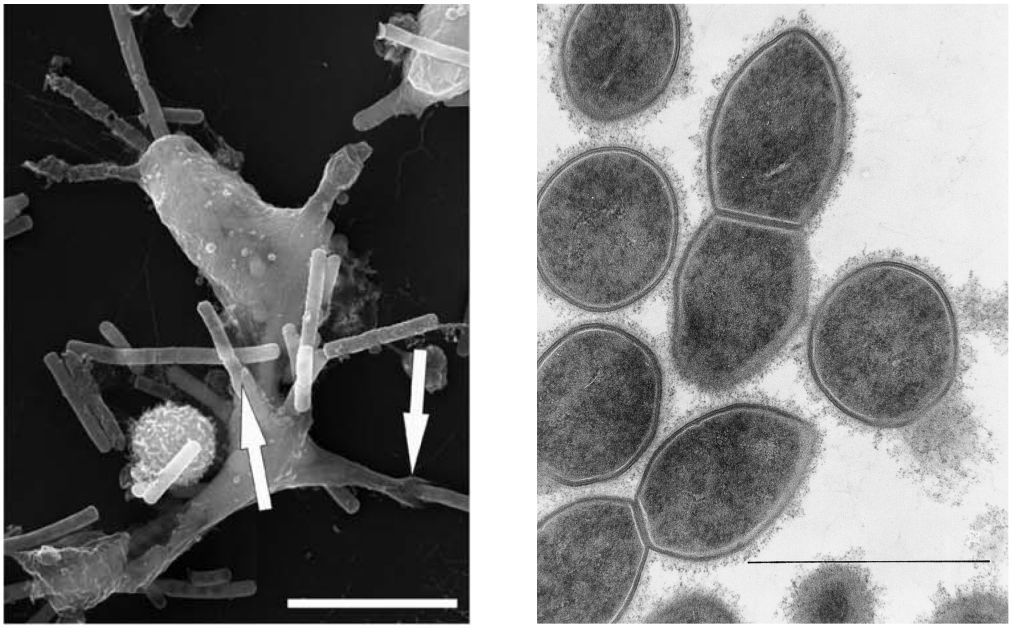


Figure 1.2: CDC-producing pathogens. *Left*, Scanning electron micrograph of neutrophils engulfing the vegetative form of rod-shaped *Bacillus anthracis* [28], the species that produces the CDC anthrolysin O. Arrows indicate phagocytosed bacteria. Scale bar 5 μm. *Right*, Electron micrograph of nonencapsulated *Streptococcus pneumoniae* [29], stained with ferritin-labelled antibody against phosphocholine. *S. pneumoniae* produces the CDC pneumolysin. Scale bar 1 μm.

1.1 Cholesterol-dependent cytolysins

1.1.1 CDC Pathogenesis

CDCs are amongst the primary virulence factors of several bacterial genera including *Bacillus*, *Clostridium*, *Listeria* and *Streptococcus* and are exploited for differing purposes depending on the pathogen [4]. Two CDC-expressing pathogens are illustrated in Figure 1.2.

Examples of CDC function include lysing target cells to prevent phagocytosis of *Streptococcus pyogenes* (streptolysin O (SLO)), and conversely, allowing *Listeria monocytogenes* to escape from phagosomes into the cytosol to replicate while maintaining an intact plasma membrane (listeriolysin O (LLO)) [4]. The typical lytic functions of CDCs are based on pore formation, and involve ion flux due to the imbalance realised upon rupture of the membrane barrier, induction of inflammatory effects, membrane blebbing and loss of cell contents [2, 4]. Some roles of CDCs

interestingly appear to go beyond simple lysis: enzyme translocation and delivery [30] (which does not appear to require pore formation [31]), lipid raft aggregation [32] and membrane remodelling [4,33], and controlling target cell transcriptional activity by histone-modification [34], for example.

The CDCs investigated in this study were pneumolysin (PLY) of *Streptococcus pneumoniae* and perfringolysin O (PFO) of *Clostridium perfringens*. PLY is not released by secretion, but by autolysis of the bacterium [29]. It is employed by *S. pneumoniae* in pneumonia, scepticaemia and meningitis. At high concentrations it forms pores that cause lysis by the mechanisms mentioned above. At sub-lytic concentrations it can induce inflammation by activating the complement pathway and enabling the bacteria to reach the blood of the target organism by disrupting the respiratory tract lining [29]. PFO is employed by *C. perfringens* to enhance the spread of tissue necrosis in gas gangrene [35]. It facilitates the escape of bacteria from phagosomes and induces blood clotting, though the exact mechanism is unclear and is interlinked with that of α-toxin [35].

Other notable diseases involving CDCs include listeriosis and gastroenteritis (LLO) [4, 36], anthrax (anthrolysin O (ALO)) [37] and pharyngitis (SLO) [3]. To summarise, CDCs support a wide range of pathogenicity and this is a fundamental reason for investigating them.

1.1.2 The CDC molecular mechanism of assembly

The CDC pores mentioned in Section 1.1.1 that lyse target membranes and induce inflammation are multimers that have assembled from single molecules. The discrete steps in this assembly process are understood primarily from structural investigations [9, 15, 20, 22, 24, 26] and ensemble fluorescence assays [8–11]. The steps are summarised in Figure 1.3; each stage is explored in detail in Section 1.1.3. Monomers, the single molecules expressed by bacteria that become the subunits of the pore and are exemplified in Figure 1.1, are typically secreted by the bacteria

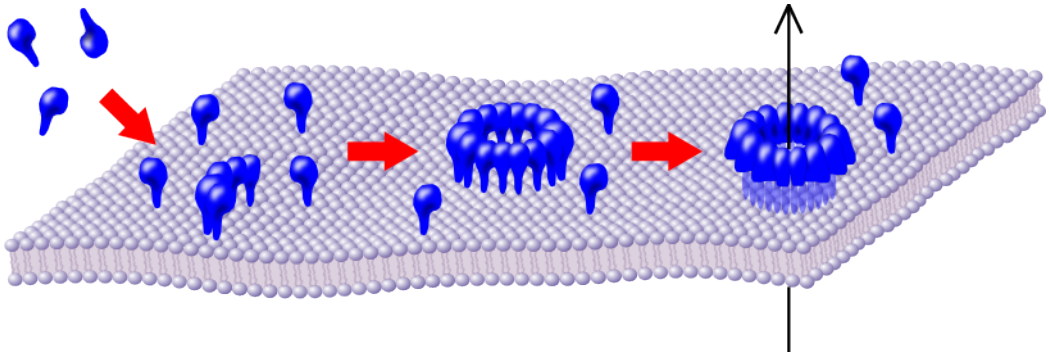


Figure 1.3: A summary of the CDC molecular mechanism of assembly. Monomers in solution bind to cholesterol in a target membrane. Once bound, they diffuse laterally and successful collisions lead to oligomerisation. 'On-pathway' oligomerisation of a single complex terminates with completion of the ring-shaped prepore. The monomers of the prepore undergo a cooperative structural transition to insert a β-barrel into the membrane and create a functional pore.

to bind to cholesterol in the membrane of a target cell. The bound monomers diffuse laterally across the target membrane, colliding with other monomers. Some collisions lead to the binding of monomers to each other and to oligomers (protein complexes comprised of several monomer subunits that have already formed by the same process of oligomerisation). For individual complexes, in the regular mode of pore formation, oligomerisation continues until the monomers form a complete ring termed a prepore [9, 24, 38]. Typically 30-50 monomer subunits comprise the prepore ring [21, 22, 39–42]. The monomers in a prepore then collectively rearrange their structure to insert a β-barrel into the membrane, creating a functional pore.

1.1.3 Structure influences the assembly mechanism

The structure of CDCs has a direct impact on their assembly mechanism and therefore an appreciation of their structure is essential in interpreting assembly data. Moreover, some of the most influential studies to date concerning CDC assembly have focused on the structure of the proteins.

Rossjohn et al. solved the crystal structure of PFO and revealed the 'key' shape of the monomer, encompassing 4 distinct domains each with a role in pore formation [15]. The features are highlighted in Figure 1.4.

Immunoglobin-like Domain 4 (D4) binds to cholesterol in target membranes via

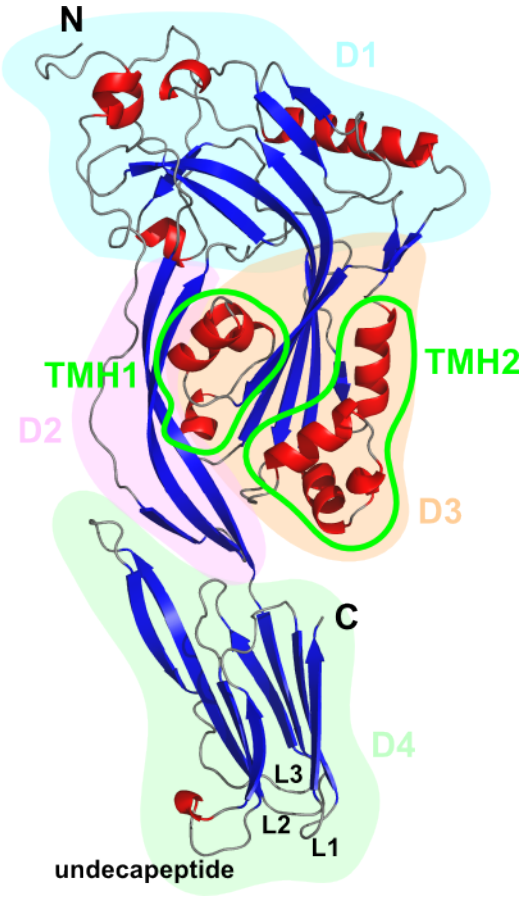


Figure 1.4: Detailed structure of PFO. Features of interest are highlighted: domains 1 to 4 (D1-D4); transmembrane helices 1 and 2 (TMH1 and TMH2); N and C termini; loops L1-L3 and the undecapeptide loop connecting β-strands in domain 4. The threonine-leucine cholesterol recognition motif is in L1 [43]. β-sheets are in blue, α-helices in red. Created with inspiration from Kacprzyk-Stokowiec et al. [44].

two amino acids in loop 1 [43, 45] (not via the highly conserved undecapeptide loop as previously suggested [23, 46]). The monomers are anchored to the membrane by hydrophobic loops 2 and 3 [41, 45]. (CD59-binding CDCs bind by an alternative mechanism [16, 42, 47] but are beyond the scope of this thesis.) Membrane binding triggers conformational changes in D3 necessary for oligomerisation [41, 48].

For the view in Figure 1.4, β-strand 5 (β5) is the short right-most β-strand in the kinked β-sheet in D1-D3 [41]. Upon membrane binding, the hydrogen bonds between β5 and the adjacent β4 are disrupted, allowing β1 of an incoming monomer to bind to β4 by π-stacking interactions (Figure 1.10 contains further detail) [5, 41, 49]. Hotze et al. recently suggested that for PFO the displacement of β5 to expose

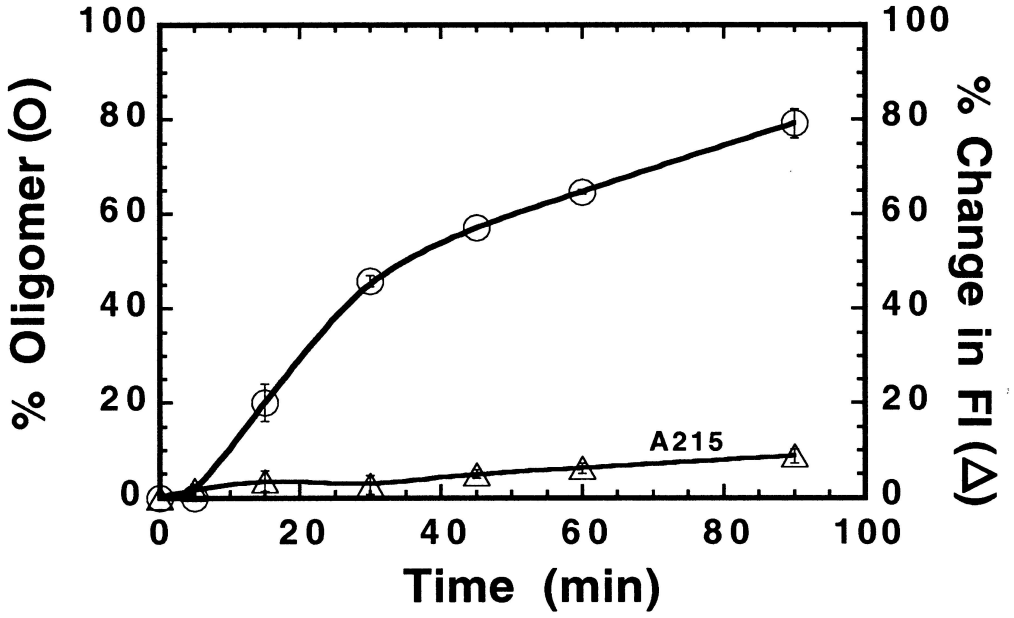


Figure 1.5: Identifying the prepore intermediate. The existence of the prepore was originally confirmed indirectly using ensemble fluorescence and SDS-AGE [9]. PFO oligomers were incubated with cholesterol-rich liposomes at 4°C and samples were removed from the mixture at the times indicated. The extent of oligomerisation (circles) was measured by a densitometric analysis of the ratio of monomer to oligomer, both of which appeared as single bands on the SDS agarose gel. The extent of β-barrel insertion (triangles) was measured by the fluorescence of the environment sensitive fluorophore nitrobenzoxadiazole (NBD), attached to TMH1 at a residue previously shown to face the membrane in the pore state. An increase in fluorescence caused by the transition of the fluorophore to the non-polar membrane environment would indicate β-barrel insertion. The extent of oligomerisation and insertion were measured relative to a sample taken from the mixture at the end of the experiment and equilibrated at 37°C before analysis, thus defining 100 % oligomerisation and 100 % β-barrel insertion. At 4°C, regular oligomers of characteristic molecular weight assembled on the liposomes, but they did not insert a β-barrel, indicating the presence of the prepore intermediate. Adapted from [9].

β4 in the formation of the initial dimer of an oligomer is reversible and caused by thermal fluctuations [49]. They proposed that interaction with an oligomer or other monomer via β1 stabilises β5 displacement in the same monomer, increasing the chance of successful binding in subsequent β4-β1 encounters and causing oligomer completion to be more likely than initiation of new oligomers [49].

The monomers remain perpendicular to the membrane upon binding [26, 50, 51], and diffuse laterally, colliding with monomers and oligomers; some fraction of collisions lead to successful oligomerisation [49]. Oligomerisation tends towards a ring-shaped prepore multimer [9,24,38], typically containing 30-50 monomers [21,22, 39–42]. The prepore was first identified indirectly by sodium dodecyl sulfate agarose

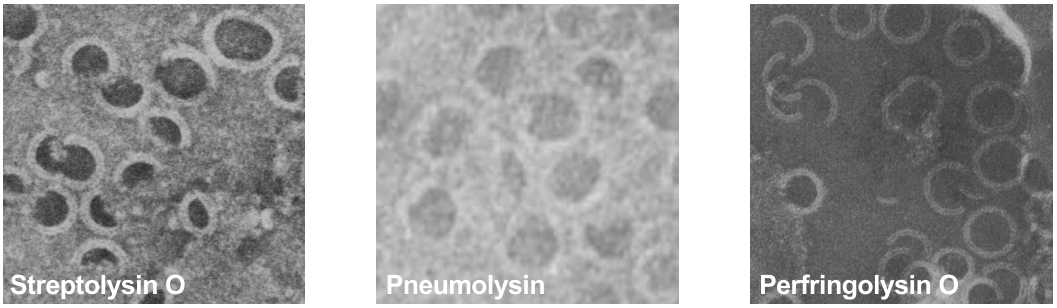


Figure 1.6: Negative-stain EM of CDCs. *Left-Right*, SLO on a trypsin-chymotrypsin treated erythrocyte membrane [20]; PLY on a sheep erythrocyte membrane [21]; PFO on human platelet-derived lipid layers [22]. Rings, arcs and larger irregular complexes such as double-arcs or interlocking arcs are present.

gel electrophoresis (SDS-AGE) and ensemble fluorescence: at 4°C, characteristic oligomers formed but the β-barrel did not insert, as demonstrated in Figure 1.5 [9]. A cooperative effort by monomers in the prepore drives insertion of the β-barrel into the membrane to create the functional pore [12], which is around 40 nm in diameter [24]. The characteristic ring shape of the multimeric pore has been verified by EM on various types of membrane many times previously (Figure 1.6) [20–22,52].

Each monomer contributes a double β-hairpin to the β-barrel; the two transmembrane helices (TMHs) in D3 that are marked in Figure 1.4 are α-helices that rearrange to form the β-hairpins [8,11]. To facilitate β-barrel insertion, the D2-D3 interface is disrupted and D2 collapses to permit the β-strands to extend the depth of the membrane [26,42,51]. During this collapse, D1 and D3 sink 40 Å closer to the membrane [26,51]. The structural rearrangements necessary for the prepore to pore transition were elegantly revealed in a cryo-EM study of PLY, which also served to verify the existence of the prepore by direct structural observation, illustrated in Figure 1.7 [24]. Insertion of the β-hairpins to create a functional pore is the final step in the typical 'on-pathway' mechanism of CDC pore formation.

1.1.4 Oligomer-based assembly

In addition to the typical on-pathway assembly mechanism that leads to ring-shaped pores, recent EM and AFM studies have revealed that oligomeric arc-shaped CDC

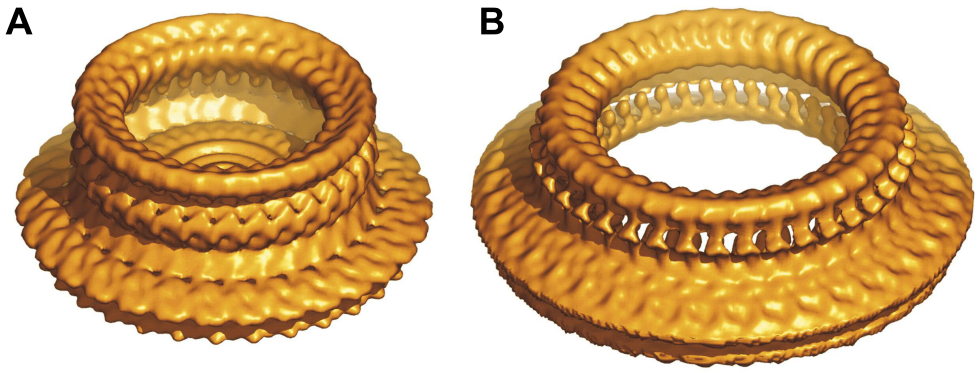


Figure 1.7: Reconstructions of the PLY prepore and pore from cryo-EM data. *A*, Density map with surface rendering of a PLY prepore on an extracted disk of liposome membrane. *B*, Equivalent view of a PLY pore and surrounding ring of membrane. Adapted from [24].

complexes are able to make lesions in bilayers [25, 27, 53]. Arcs have regularly been observed in EM studies (see Figure 1.6), but their biological relevance was disputed for some time ([42, 54] compared to [25, 27, 55]). The recent studies suggest they are not dead-end complexes or artefacts of EM sample preparation sitting atop the membrane as previously claimed [42]. Rather, they appear to be a mechanism for increasing the efficacy of CDCs, for example in membrane rupture or inducing inflammation.

Figure 1.8 summarises the proposed structure of arcs, and an argument for their functionality based on channel conductances [55, 56]. Figure 1.8D illustrates an AFM tip penetrating the lumen of an arc to confirm that it formed a membrane lesion [25]. The height of arcs in AFM scans is also more consistent with the pore arrangement than the monomer/prepore arrangement, an argument that has been made previously [57].

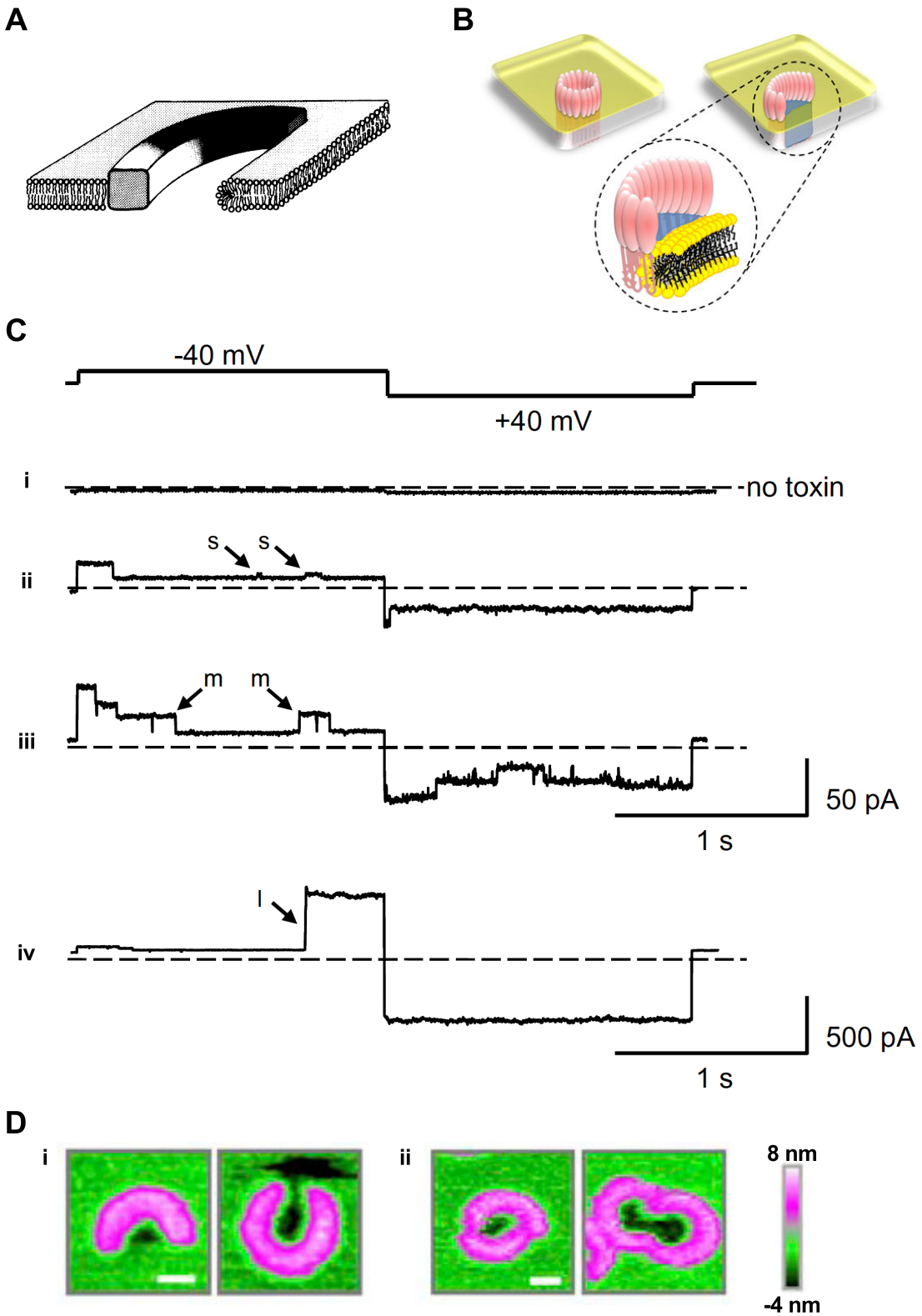

A
B
C
-40 mV
+40 mV
i
-no toxin
ii
s
s
iii
m
m
50 pA
1 s
iv
l
500 pA
1 s
D
i
ii
8 nm
-4 nm

Figure 1.8: Arcs do make holes. *A*, Schematic of the proposed form of an SLO arc-pore, published in 1985 [20]. *B*, Since then, the case for arc-pores has consistently been made [55, 57, 58]. On the opposing side of an arc-pore the lipids are proposed to adopt a toroidal arrangement. *C, i-iv*, Arc-pores have been argued for on the basis that CDCs exhibit a range of conductances when inserted into a membrane: El-Rachkidy et al. classified PLY pore-conductances as small, medium and large (s $<$ 0.2 nS, m = 0.2-1 nS and l $>$ 1 nS respectively) [56]. *D*, The pore-forming capability of arcs has recently been verified by AFM [25,27] and EM [53]; the AFM scan shown demonstrates that an AFM tip was able to penetrate through to the mica support in the lumen of an arc-pore, whereas elsewhere the membrane remained intact [25].

Large irregular complexes formed by multiple arc-shaped oligomers have also consistently been observed in EM and AFM images of CDCs (see Figures 1.6 [20–22], 1.8D [25] and 1.9C [27]). AFM studies again proved that such complexes are able to puncture the membrane and form lesions with a range of effective diameters, some larger than the regular ring-shaped pore [25, 27]. Figure 1.9 highlights this mechanism for LLO, as well as revealing the plastic nature of LLO pores. Podobnik et al. revealed the surprising ability of LLO complexes to remodel and accommodate new oligomers even after insertion (Figure 1.9A) [27].

The facility to create functional complexes comprised of multiple distinct arcs is unlikely to be a significant feature of the general assembly mechanism, rather a convenient off-pathway side effect, because the comprising arcs must assemble by another mechanism initially. It is a part of the global assembly mechanism nonetheless, and is pertinent to this study, as discussed in Sections 4.3.4 and 5.5.3.

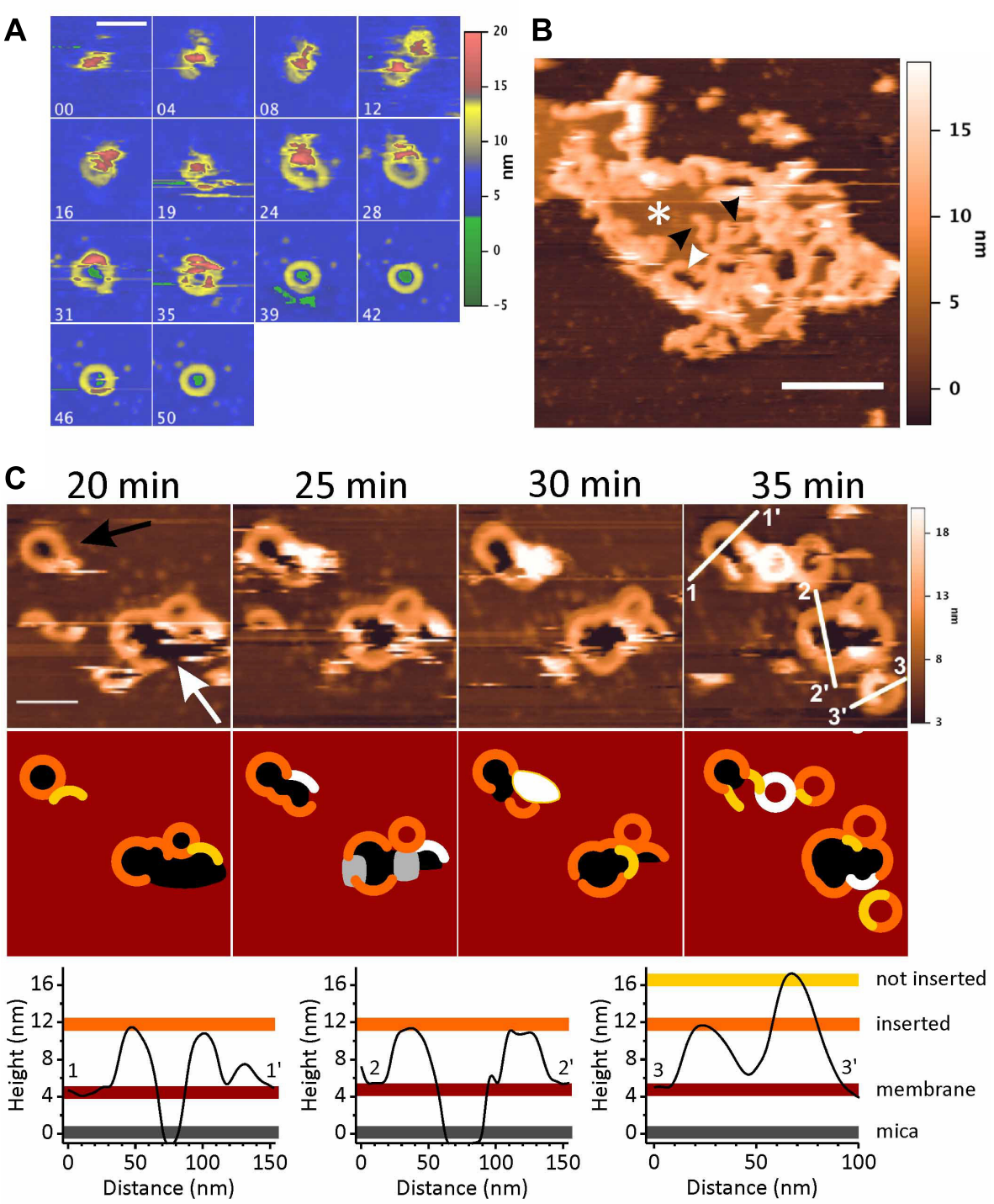


Figure 1.9: Plastic LLO assembly. An additional feature of assembly for LLO revealed by AFM [27]: the oligomers seemed to be less rigid than expected and able to remodel themselves to allow more efficient use of monomers for membrane rupture. *A*, Assembly and remodelling of a wild-type LLO complex on a supported lipid bilayer (SLB) over the indicated number of minutes. Scale bar 100 nm. *B*, Scan of wild-type LLO oligomers; white asterisk indicates a patch of SLB, black arrows indicate arcs, white arrow indicates a large irregular complex formed from multiple arcs creating a membrane lesion. Scale bar 500 nm. *C*, H311A LLO mutant oligomeric complexes remodelling over time. Top: AFM scans at 5 minute intervals (times since addition of LLO to the SLB are indicated); black arrow indicates an initially complete ring, white arrow a complex formed from conjoined arcs. Centre: schematic representation of the LLO structures. Bottom: height profiles corresponding to white lines in the 35 min AFM scan. Adapted from [27].

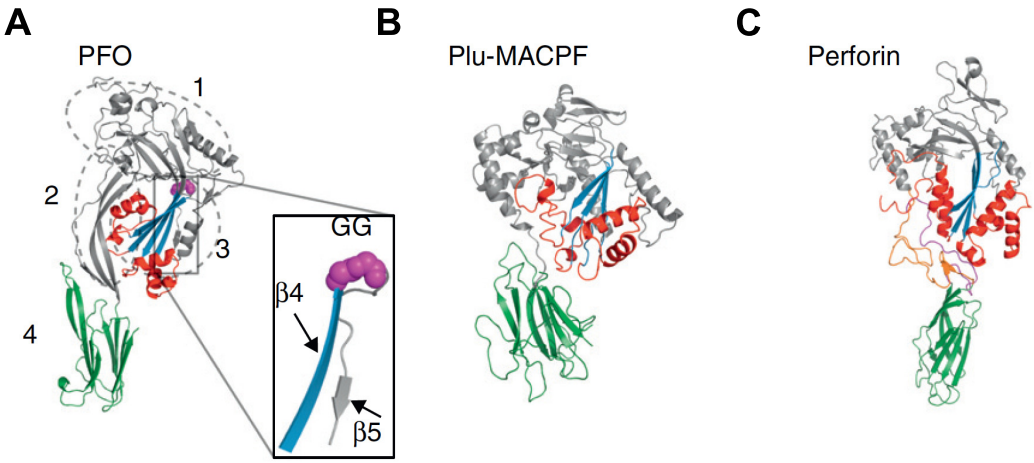


Figure 1.10: Commonality between MACPF and CDC proteins. *A*-*C*, Crystal structures of 3 different MACPF/CDC proteins: the CDC PFO, and Plu-MACPF and perforin from the MACPF family. The common CDC/MACPF fold contains the kinked β-sheet spanning D1-D3, and the TMH regions. The central part of the kinked β-sheet is coloured in blue, the TMH regions are coloured red. Membrane-binding domains are in green. (The orange and purple colours in perforin are an epidermal growth factor-like domain and the C-terminal tail, respectively.) The discrete domains of PFO are labelled. The inset in *A* highlights β-strands β4 and β5; β5 rotates to allow the pairing of β4 with β1 from another monomer during oligomerisation. The magenta spheres are a double glycine motif, connecting β4 and β5, that is highly conserved in MACPF/CDC proteins; mutating the motif prevents the displacement of β5 required for monomer-monomer interaction. Adapted from [41].

1.1.5 The MACPF family of proteins

The CDCs exhibit structural similarity to the eukaryotic membrane attack complex/perforin (MACPF) family of pore-forming proteins [41, 59–61]. Notable shared features include the kinked β-sheet spanning D1-D3, the flattened shape, the double glycine motif and the TMHs (not all MACPF proteins exhibit C-terminal structures similar to D4 of the CDCs) [41, 61]; some of these features are highlighted in Figure 1.10. MACPF proteins utilise pore formation to support the immune response against bacteria, viruses and tumours [61]. They have also been found to influence neural development [62] and embryonic structure [63, 64].

The structural conservation between MACPF proteins and CDCs suggests that their mechanism of pore formation will also share common features. The symmetry of equivalent mechanisms employed by pathogenic bacteria and eukaryotic immune surveillance proteins is an interesting biological phenomenon, but crucially it implies that characteristics of assembly determined for one family will directly relate to the

other. The results presented in this thesis regarding CDC assembly kinetics may extend to the MACPF family.

1.2 Remaining unknowns

Section 1.1 highlights the wealth of information learned about CDCs to date, and illustrates our strong understanding of the overall mechanism of pore formation. There remains a gap, however, when it comes to understanding the precise stepwise details of oligomerisation at the single-pore level. The kinetics of assembly have been reported, but generally at an ensemble level by fluorescence [9, 10, 54] or haemolysis [13, 14]. Moreover, the dynamic mechanism of pore formation can only be indirectly inferred from structural investigations, which report the discrete stages of assembly: unbound monomer, membrane-bound monomer, prepore, membrane-inserted pore and arc assemblies. Structural studies do not reveal the dynamic transition from one stage to the next and so arguably offer an incomplete understanding of assembly.

Often the difficulty in obtaining high spatial and temporal resolution information has been bypassed by clever mutagenesis and cross-linking approaches that synchronise the protein population at different stages of assembly [25, 38]. However, these approaches are still unable to resolve individual steps in the growth of an oligomer, and it is difficult to rule out non-biological artefacts caused by cross-linking or mutagenesis. The best dynamic picture to date of CDC assembly with high spatial resolution was provided by AFM in two recent studies [25,27]; an example is provided in Figure 1.11 [25].

Figure 1.11A depicts suilysin prepore motion by the presence of streaks in an AFM scan: a convolution with the horizontally scanned AFM tip. The prepores were disulphide-locked to prevent pore formation. Upon reducing the disulphide bond, the prepores inserted into the bilayer to form pores. Separately, the authors analysed the stoichiometry of oligomers in the prepore state, reducing their mobility

by cooling. They found a distribution of stoichiometries equivalent in both the prepore and pore states, revealing that oligomerisation of individual complexes occurred entirely before membrane penetration (though the plasticity of pores represented in Figure 1.9 seems to be an exception to this claim, for LLO at least). The stoichiometry distribution was fitted accurately with a stepwise irreversible monomer-addition model of assembly [25].

The AFM studies (represented by Figures 1.9 and 1.11) are highlighted as dynamic pictures of assembly that resolve individual oligomers. However, the scanning requirement for AFM limited the frame-rate to minutes in these examples (frame-rate being directly related to the size of the scanned area [65]), which is insufficiently high to capture dynamic monomer-monomer or monomer-oligomer interactions. The present study attempts to address the gap in simultaneous high spatial and temporal resolution data pervading the field of CDCs. The technique employed was single-molecule fluorescence (sm-fluorescence) imaging of droplet interface bilayers (DIBs).

In comparison with the AFM studies, sm-fluorescence sacrifices spatial resolution (200 nm versus a few nanometres) but achieves better temporal resolution (milliseconds versus minutes). Moreover, AFM and EM identify pores indirectly by the absence of lipids in the lumen and the change in height of the monomers, they do not directly detect the passage of ions through pores which defines them as functional. DIBs are capable of measuring the conductance of pores while simultaneously imaging them by sm-fluorescence. Sections 1.4 and 1.5 elaborate on the techniques employed in this study.

The single-pore dynamics are amongst several unresolved questions in the CDC field. The function of CDCs *in vivo* is only partially understood in several cases [4, 35], particularly the roles that do not involve typical lysis [30–34], which hint at undiscovered functions. Super-resolution light microscopy might be able to help in these cases [66], and is discussed further in Section 1.4.1.

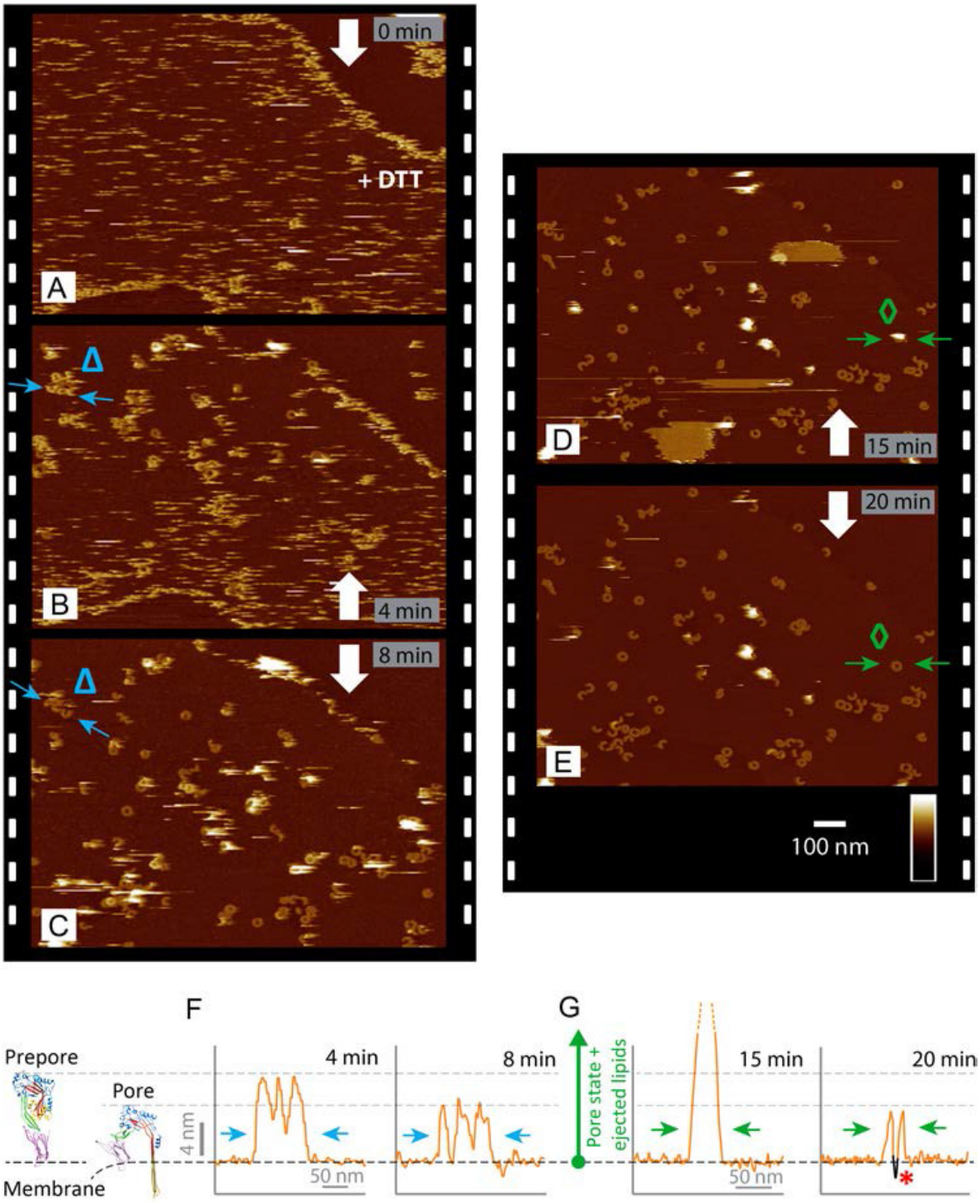


Figure 1.11: Dynamics of the prepore to pore conversion resolved by AFM. *A-E*, Consecutive AFM scans of a disulphide locked suilysin mutant following reduction of the crosslink by addition of DTT (halfway through scan *A*) to permit insertion of the β-barrel. White arrows indicate direction of the scan; the start times of the scan relative to the first scan; frame time 4 minutes. The triangles highlight a large irregular complex formed from multiple arcs, in the prepore state in *B* and later in the pore state in *C*. The diamond indicates a putative lipid-ejection event in *D* and the corresponding complex after the lipids have condensed into the membrane in *E*. *F-G*, Height profiles of the region between the arrows indicated by triangles and diamonds in *A-E*. Star indicates membrane penetration by the pore. Adapted from [25].

Mechanistically, the nature of β-barrel insertion is of interest: extreme synchronisation might be necessary to distinguish simultaneous β-hairpin insertion from consecutive hairpin insertions of the monomers in an oligomer. There are doubtless new mechanistic details to be gathered from the unique structural features of individual CDCs, exemplified by intermedilysin [16] and the recently solved PLY structure [18, 19]. Furthermore, the fate of lipids following β-barrel insertion is poorly understood, though recent data suggests that they are expelled to settle on top of and gradually condense back into the membrane [25].

Each new discovery concerning the mechanism of the MACPF/CDC family of proteins would benefit from a dynamic context. For example, complete prepores may persist for several seconds before converting to a pore, or may insert immediately following ring completion. The full impact of mechanistic details is difficult to fully appreciate without being time-resolved relative to other features of assembly.

1.3 Other pore-forming toxins and their assembly mechanisms

Understanding CDCs was paramount in preparing to capture their assembly. Useful insight on the appropriate techniques to use was also gathered from studies that have captured other PFT's assembly. A previous study on α-haemolysin (αHL) by the Wallace lab used monomers labelled with fluorophores, added to a DIB by injection and observed by single-molecule total internal reflection fluorescence microscopy (smTIRF), to examine the mechanism of αHL assembly [67]. The techniques used for the αHL study are discussed in subsequent sections, as they are fundamentally equivalent to the techniques used in this study, but the method is summarised in Figure 1.12.

The relevant results from the αHL study are summarised in Figure 1.13. The assembly of a heptameric αHL complex was detected by bright spots caused by

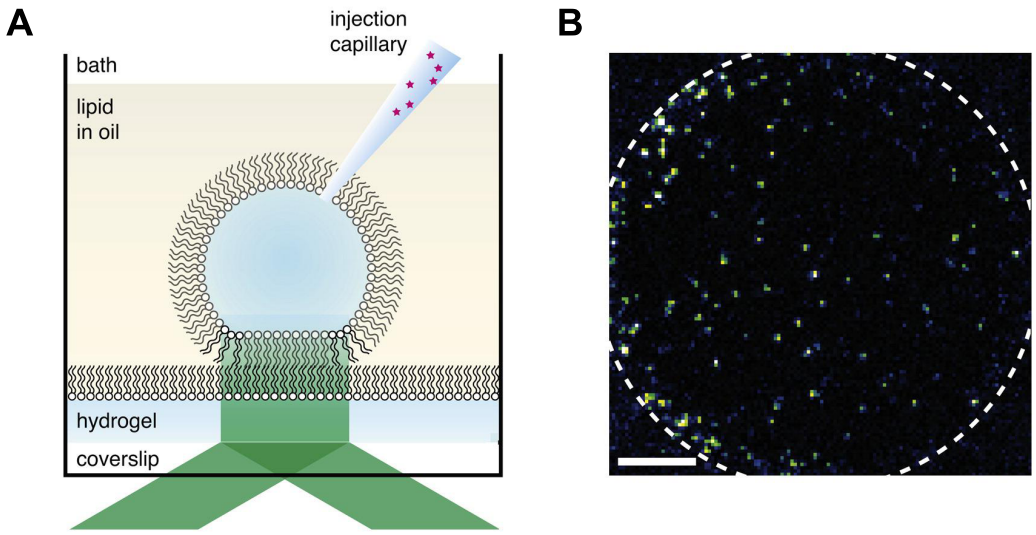


Figure 1.12: DIB approach to study αHL assembly. *A*, A DIB (Section 1.5) on a hydrogel substrate was imaged by TIRF (Section 1.4) following injection of labelled αHL monomers into the droplet. The bilayer was imaged from below using an inverted objective lens. *B*, Single labelled αHL monomers were resolved diffusing on the bilayer (there is variation in spot intensities due to noise). White dashed line indicates the bilayer edge. Scale bar 10 μm. Adapted from [67].

the colocalisation of many fluorophore-labelled monomers. The heptamers were observed to assemble in under 5 ms (the temporal resolution of the experiment), as demonstrated in Figure 1.13A. Moreover, Figure 1.13B shows that only two αHL sub-populations were observed, the monomer and the heptamer; intermediate stoichiometries were conspicuously absent at the 5 ms frame-rate. These results limited the mechanisms that could explain αHL assembly, as shown in Figure 1.13, i and ii. The possible mechanisms by which αHL can assemble provide a useful reference with which to interpret CDC assembly [67].

Another example of PFT assembly quantified by sm-fluorescence comes from Nguyen et al. and the bicomponent pore-former γ-haemolysin (γHL) [68]. They employed a combination of Förster resonance energy transfer and a TIRF arrangement (Section 1.4) to determine the stoichiometry and density of γHL subpopulations at 30 ms temporal resolution. From here they calculated the binding and association constants, where applicable, for the sub-populations: monomers, heterodimers, tetramers, hexa/heptameric pores and pore clusters. They concluded that the assembly of γHL pores was principally by dimer formation and association

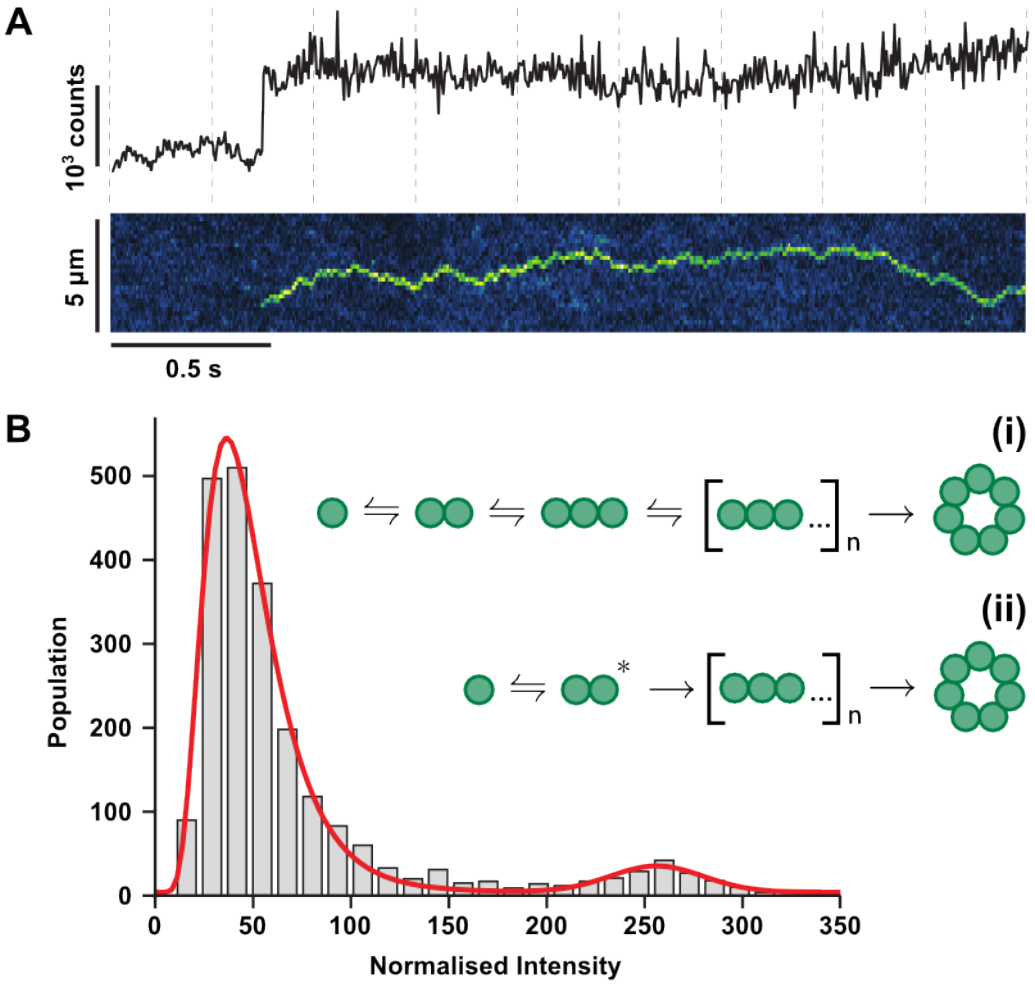


Figure 1.13: αHL exhibits rapid assembly. αHL heptamers were observed assembling by the method illustrated in Figure 1.12, when the injected monomer concentration was increased. *A*, The intensity trace of an assembling complex (top) and the corresponding kymograph (bottom) revealed that assembly was entirely completed within 5 ms (the temporal resolution in the experiment). *B*, A histogram of intensities for spots on the bilayer corresponding to labelled αHL: the two peaks correspond to monomers and heptamers. *Inset*, Rapid assembly and the binary population of αHL complexes only allows two possible mechanisms of assembly for the heptamer: (*i*), reversible addition of monomers up to an irreversible ring-completion step or (*ii*), reversible dimerisation inducing an activated complex and subsequently irreversible monomer addition. Adapted from [67].

and was also highly cooperative [68].

1.4 Single-molecule fluorescence to study CDCs

Previous sections highlight the need for a deeper understanding of CDC assembly kinetics; accordingly, this thesis describes efforts to elucidate and quantify CDC

assembly kinetics. The technique used to image CDC assembly in this study was total internal reflection fluorescence microscopy (TIRF) (specifically, single-molecule total internal reflection fluorescence microscopy (smTIRF)); the motivation for this imaging technique is outlined below.

1.4.1 Basic principles of sm-fluorescence

Fluorescence is light emission from a molecule that has been excited to a higher energy state by absorbing electromagnetic radiation [69]. The energy of the excited state determines the wavelength of light that can be absorbed by the molecule. A molecule typically remains in the excited state for a few nanoseconds before emitting light at a longer wavelength than the excitation light; the difference in wavelength, known as the Stokes shift, depends on the fluorophore [69]. The difference in wavelengths for excitation and emission allows the excitation light to be discriminated from the fluorescence signal.

Fluorophores are molecules that are exploited for their fluorescent properties [69]. The principle of single-molecule fluorescence (sm-fluorescence) is to attach a fluorophore to a protein of interest, and then to excite the fluorophore using an appropriate wavelength of monochromatic light from a laser. The protein is studied indirectly by monitoring the labelling fluorophore. Fluorophores are often chosen for their brightness, a product of their quantum yield (photons emitted by fluorescence per absorbed photon) and absorption cross section (ability to absorb an incident photon), and their photostability (resistance to photobleaching [70–72], Section 4.4), relative to other molecules [73, 74]. When light from a sample is collected to form an image, the fluorophores appear brighter than other molecules in the illuminated volume and are easily identified (see Figure 1.12 and Chapter 4). Fluorophores can be synthetic dyes (typically smaller and brighter but require conjugation to the protein of interest) or fluorescent proteins (larger and dimmer but are attached endogenously); the fluorophores employed in this study were all of

the former category.

An important parameter to optimise for sm-fluorescence is the signal-to-noise ratio (SNR) [71, 73]. With respect to sm-fluorescence, the SNR reports the strength of the desired fluorophore signal relative to the unwanted background signal originating from other light sources. Such spurious light is typically caused by the inherent natural fluorescence (autofluorescence) of cellular components *in vivo*, or from contaminants *in vitro*. To improve SNR, sm-fluorescence techniques generally detect light only from a limited part of the sample: the signal from single fluorophores in the observed volume is entirely retained, while spurious light from elsewhere in the sample is reduced [71]. Two well-established sm-fluorescence techniques that operate under this principle are confocal microscopy and TIRF.

Confocal microscopy uses a pinhole at a conjugate image plane before the detector to reject out-of-focus light [72, 75]. As only light from the confocal volume is detected, a sample must be scanned with the laser to construct a full image. TIRF relies on the limited, approximately 200 nm penetration depth of an evanescent field created by the total internal reflection of light at an interface between two materials with differing refractive indices [76–78]. While allowing millisecond temporal resolution - essentially limited by the detector speed and number of photons collected - and a wide field of view, TIRF only permits imaging of a thin depth of sample near the support. TIRF is not suitable for imaging 3D samples, but provided they are sufficiently close to the support it can resolve single molecules with high SNR (smTIRF, Figure 1.12B for example), and is therefore suited to imaging processes occurring in the cell membrane [78].

Conventional sm-fluorescence is limited to a lateral spatial resolution of approximately 200 nm, a limit imposed by the diffraction of light passing through components in the optical path [79, 80]. In recent years, however, a host of new developments in sm-fluorescence have proved capable of bypassing the diffraction limit; collectively these are termed super-resolution techniques [72, 79]. Their

spatial resolution, which can reach 10 nm, almost bridges the gap between EM and conventional sm-fluorescence [72, 79, 80], but their temporal resolution is generally limited to seconds due to the requirement for stochastic detection of subsets of fluorophores, or the need to scan the sample as in confocal microscopy [66, 72, 79]. Super-resolution applied to CDCs is discussed in a recent review [66].

1.4.2 Applying sm-fluorescence to CDCs

Sm-fluorescence offers several benefits for the study of CDCs: dynamic information; detecting unique sub-populations and intermediates without ensemble averaging; removing the need to synchronise the protein population artificially for dynamic studies [71]. Moreover, labelling the protein of interest with a fluorophore provides high specificity: there is no confusion as to which molecule is being detected. In comparison, antibody labelling for improved specificity in EM can be challenging [80], and in ensemble fluorescence the separate molecules are indistinguishable.

There are also disadvantages to sm-fluorescence: the diffraction-limited 200 nm spatial resolution of conventional sm-fluorescence is significantly worse than the sub-nanometre scale offered by EM, so oligomers are inferred indirectly as their structure cannot be resolved. (The spatial resolution in this study was typically 550 nm, Section 5.5.2.) Though the fluorophore offers specificity it can also influence the biological function of a labelled protein (a problem that is compounded for large labels such as fluorescent proteins), and controls must be performed to alleviate this concern. Permanent destruction of the fluorescent mechanism of fluorophores by photobleaching must be combatted [70–72], and the implementation of optics for sm-fluorescence requires significant expertise, though doubtless this is not a unique problem amongst biophysical techniques.

In this study, the principal aim was to investigate CDC assembly kinetics at the single-pore level. Sm-fluorescence techniques in general offer dynamic information; smTIRF was chosen because it combines the millisecond temporal resolution likely

to be relevant to monomer-monomer or monomer-oligomer interactions with a wide field of view and can achieve high SNR [78]. The wide field of view allows imaging of a large area of bilayer (2.6×10^3 μm^2 in this study, for example), and so many diffusing monomers and assembling complexes can be observed in parallel. Finally, the assembly of CDCs bound to a bilayer is suitable for imaging within the shallow depth permitted by smTIRF. SmTIRF was therefore the most appropriate imaging technique with which to capture CDC assembly. Previous studies where features of PFT assembly were revealed - the αHL and γHL studies mentioned in Section 1.3 - further support smTIRF as the choice of imaging technique. Fluorescence correlation spectroscopy combined with wide-field imaging, using the 'number and brightness' analysis for example [81], is another technique that could provide useful information on the CDC assembly process and will be investigated in the future; a review of such methods is beyond the scope of this thesis.

1.5 Droplet interface bilayers

Besides the imaging technique, an important experimental consideration was the choice of artificial bilayer. In this study, droplet interface bilayers (DIBs) were used as a model membrane to support the capture of CDC assembly. The reasons for an artificial bilayer and in particular a DIB are described in the following section. The arguments for an artificial bilayer over a biological membrane are closely related to the arguments for experiments performed *in vitro* versus *in vivo*.

1.5.1 DIBs as artificial bilayers

A DIB, depicted in Figure 1.14, is foremost an artificial bilayer. Real biological membranes such as erythrocytes or Chinese hamster ovary cells offer a more native environment for the protein than artificial bilayers. However, CDCs only require a lipid bilayer with cholesterol to oligomerise and form pores [41, 42]: while

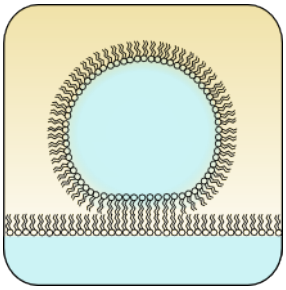


Figure 1.14: Essence of a droplet interface bilayer. A droplet interface bilayer is formed by the contact of two monolayers; one monolayer at least is at the interface between an aqueous droplet and a lipid-in-oil solution. The other monolayer can be another droplet monolayer, or it can be formed on a spin-coated hydrogel substrate, covered with a similar lipid-in-oil solution, as illustrated. The two monolayers form over several minutes after the aqueous phase is introduced to the lipid-in-oil solution, before they are brought into contact.

interference from other proteins may occur on a biological membrane, this does not appear to contribute to the fundamental pore-forming mechanism employed by CDCs (except for the CD59-binding CDCs [42, 82, 83]). For studying the CDC molecular mechanism, it is therefore helpful to reduce the bilayer-protein system to the fewest possible components with which oligomerisation and pore formation can occur, isolating the mechanism of interest from the chaos of a real cell membrane. Such a reduction in complexity is offered by artificial bilayers. Furthermore, autofluorescence (Section 1.4.1) is a problem with imaging real cells and cell membranes [73, 78], but is virtually eliminated in a contaminant-free artificial bilayer-protein system. Where possible, however, it is important to validate results obtained *in vitro* using data from live cells.

1.5.2 Alternative artificial bilayers

There are several types of artificial bilayer that could be used to characterise CDCs, some of which are presented in Figure 1.15. This section explains the choice of DIBs for this study, by reviewing the properties of other available artificial bilayers.

Black lipid membranes offer the advantage of being free-standing, and not resting on or interacting with a solid support [84]; Figure 1.15Ai depicts a schematic of a black lipid membrane [85]. Created by the Montal-Mueller method [86], these

bilayers form across a small aperture in a sheet of plastic that separates two aqueous chambers, and are useful for electrical recordings due to the easy access to the two chambers on either side of the bilayer. These bilayers suffer from instability, however, and they cannot be imaged at high resolution because the bilayer cannot be placed near a lens.

A more reliable, versatile and easy-to-make analogue of a black lipid membrane is the droplet-droplet DIB [85]. This form of bilayer is formed by the contact of two aqueous droplets in oil, each with a monolayer at the interface after incubation in a lipid-in-oil solution (Figure 1.15Aii). The droplets are suspended from electrodes, as illustrated in Figure 1.15Aiii, so the current across the bilayer can be measured. As with black lipid membranes, these bilayers do not interact with a solid support, and are useful for electrophysiological interrogation of pore- or ion channel-forming proteins dissolved in the droplets (for example: [87–89]). However, critically they are also difficult to place near a lens and therefore to image with high resolution.

Supported lipid bilayers (SLBs) are formed by the rupture of vesicles on a solid support (Figure 1.15B); they can be interrogated by mechanical probes such as AFM [25], and also by the short penetration depth evanescent field created in TIRF [90, 92]. They have been used in several previous studies of CDCs [25–27]. SLBs are well-suited to the parallelised study of single-complex CDC assembly because of their compliance with wide-field microscopy. The disadvantages of SLBs include their interaction with the underlying support [90], which disrupts the interaction of membrane proteins, for example, by preventing their diffusion. Efforts to alleviate this problem exploit spacers between the support and the bilayer (see Figure 1.15B). It is also very difficult to access the underside of an SLB with an electrode, for functional measurements of pores [90, 93].

Liposomes comprise a bilayer encapsulating an aqueous compartment, generally suspended in solution (Figure 1.15C) [94]. Liposomes are simple to make [91,94] and can be imaged at molecular resolution using EM [24,40] or tracked with fluorescence

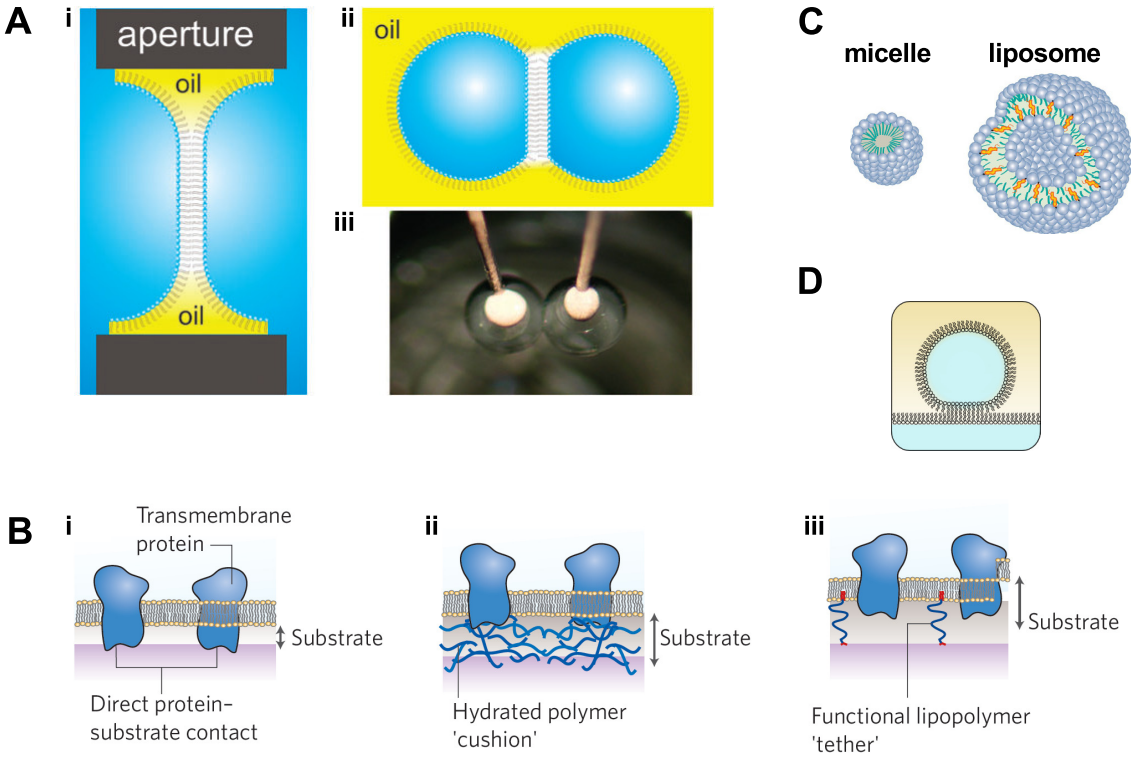


Figure 1.15: Alternative artificial bilayers. *A*, Free-standing bilayers between two aqueous compartments [85]. *i*, Black lipid membranes are formed across an aperture and are notoriously unstable; *ii*, Droplet-droplet DIBs are stable analogues of the black lipid membrane and are simple to make; *iii*, A droplet-droplet DIB *in situ*, suspended from an electrode in each droplet [85]. *B*, An SLB is formed by fusing vesicles with the substrate. Membrane components are prone to interact with the substrate (*i*), so attempts have been made to decouple the bilayer from the substrate (*ii-iii*) [90]. *C*, Micelles and liposomes assemble depending on the concentration of lipids in solution [91]. Liposomes can be suspended in solution or tethered, their bilayer can be highly curved, and they can be prepared by different methods [91]. *D*, A DIB, redrawn here for completeness.

microscopy [95]. Electrophysiological recordings are difficult but possible to perform under a patch-clamp arrangement [96], but often functional protein pores in liposomes are assessed indirectly using ion flux between the internal and external compartments to induce fluorescence [54, 97, 98].

Liposomes are less suitable for parallel single-molecule imaging of CDCs, however, because their three-dimensional structure would necessitate tethering and scanning to form an image. Moreover, liposomes are typically smaller than a diffraction limit in diameter, making tracking CDC monomers assembling into pores on liposomes impossible by conventional smTIRF (the monomers would all appear colocalised even before assembly). Liposomes have been used in several studies of

CDCs, but normally with ensemble fluorescence assays or EM [9, 10, 24, 40, 54].

Droplet-hydrogel DIBs (Figure 1.14) have been used previously to study the assembly of pore-forming toxins as discussed in Section 1.3 [67]. The construction of the droplet-hydrogel DIB arrangement is described in Chapter 3 [99]. As a supported bilayer, DIBs inevitably experience some interaction with the underlying hydrogel substrate, similar to SLBs. However, Thompson et al. reported that lipids in a DIB diffused at a comparable rate to lipids in an unsupported bilayer, a factor of 20 times higher than in a regular SLB, and that αHL pores in a DIB diffused at 16.8 ± 4.2 $\mu m^2 s^{-1}$ [100]. Conversely, Huang et al. intentionally restricted the diffusion of αHL pores to under 20 nm in a 30 minute recording, for optical sensing of nucleic acids, by dehydrating the hydrogel substrate [101]. Therefore, the interaction with the substrate in a DIB is subject to some degree of control via hydration of the hydrogel; it can be made minimal relative to a regular SLB.

A disadvantage of DIBs, in comparison to black lipid membranes or SLBs for example, is that introducing a protein sample post-bilayer formation is not trivial; this facility may be desirable for observing time-dependent processes such as assembly of protein complexes, as was the case in this study. Subsequent addition of protein to the droplet is accomplished with a nanolitre microprocessor-controlled injector (Sections 3.2.3 and 3.3).

Overall droplet-hydrogel DIBs offer several benefits for studying CDC assembly. The large planar bilayer is suitable for imaging by smTIRF as it can be placed very close to an objective lens (Section 3.1) [67, 99, 102]. The bilayer is generally hundreds of microns across and the field of view tens of microns, so multiple protein complexes can be observed in parallel on the bilayer. Most significantly, a droplet-hydrogel DIB can be interrogated simultaneously by electrical and optical methods (see Section 3.4) [101–103]. This dual capability is often difficult or impossible with other types of artificial bilayer, depending on the particular type. Throughout the rest of this thesis, the droplet-hydrogel DIB is simply referred to as a DIB and the

droplet-droplet form is always referred to in full.

1.5.3 DIB versatility

The final justification for choosing DIBs comes from the αHL study mentioned in Section 1.3, where assembly of αHL heptamers was successfully observed with 5 ms temporal resolution using smTIRF and DIBs [67]. Moreover, DIBs have demonstrated their versatility in several recent studies, with applications not limited to sm-fluorescence or β-barrel PFTs [101, 104, 105].

One of the foremost potential uses of DIBs is as a diagnostic tool for characterising membrane proteins and inhibitors that are of medical interest. For example, an array of DIBs was used to detect the presence of αHL in different bilayers; a fluorogenic dye in the droplets became fluorescent upon reaction with Ca^{2+} that passively diffused through αHL pores from the hydrogel into the droplets [106]. Moreover, the reaction rates for γ-cyclodextrin blocking αHL pores was measured at different concentrations to obtain a dissociation constant of $K_d = 340$ μM. This method could be extended to other pore-formers and their inhibitors.

Other notable uses of DIBs include electrical single-channel recordings (SCRs) of reconstituted eukaryotic ion channels [104], imaging lipid nanodomains by interferometric scattering microscopy [105] and discriminating DNA sequences by optical single-channel recordings (oSCRs) of nanopores [101]. Nanopore sequencing has risen to the forefront of genome sequencing techniques in recent years [107], and the development of the optical analogue by Huang and colleagues is significant: by the optical method, several nanopores can be used for sequencing in parallel in the same bilayer, and several bilayers can be measured simultaneously [101].

The suitability of DIBs for membrane protein diagnostics is revisited in Chapter 6 in light of the experiments in this study.

1.6 Key findings from this thesis

The chapters of this thesis are split roughly between methods (Chapters 2 and 3), results (Chapter 4) and analysis (Chapter 5). Chapter 2 describes the synthesis of a biologically viable protein sample suitable for imaging by the smTIRF methods discussed above. Standard techniques from molecular biology were employed to synthesise and characterise the protein sample, including bacterial expression and liquid chromatography. The protein synthesised was PLY, an archetypal CDC, and several results in Chapters 3 and 4 refer to PLY. However, labelled PFO received from our collaborator A. P. Heuck was used primarily to capture assembly (Chapter 4) and for the subsequent quantification of assembly in Chapter 5, because in repeats, PFO's assembly behaviour appeared less sensitive to variation in protein concentration and bilayer properties (Section 3.2.2).

Chapter 3 focuses on establishing a robust protocol for the imaging of CDC assembly by smTIRF, as well as detailing the DIB protocol modifications that were necessary for PLY and PFO. Confirming the biological function of the protein sample in a DIB by electrophysiology is also discussed in Chapter 3.

The protein synthesis and protocol development together were preparation for recording videos of CDC assembly by smTIRF at millisecond frame-rate. These videos and other smTIRF-based results characterising CDCs are presented in Chapter 4. Assembly of CDCs was captured at a range of concentrations, and a photobleaching technique suggested that the complexes observed by smTIRF were of the expected stoichiometry for CDCs.

Finally, Chapter 5 concerns the analysis of assembly videos from Chapter 4, a discussion of the assembly mechanism from this data and quantification of CDC assembly kinetics. The principal mechanism of assembly for PFO was ultimately not trivial to interpret by this imaging technique, but the analysis supported a model of irreversible stepwise monomer addition. The rate of successful collisions between PFO monomers and oligomers was determined from the time-wise alignment of the

assembly of many complexes.

1.7 Outlook

Despite the detailed knowledge of CDCs and their mechanism of pore formation afforded by previous structural and biochemical studies, a high-resolution recording of single assembling complexes at the timescale relevant for oligomerisation has been missing. This study presents the successful application of smTIRF to capture CDC assembly at 60 ms frame-rate. While helping to alleviate the paucity of single-complex dynamic information in the field, the results will hopefully encourage the use of sm-fluorescence in future studies of CDCs. There are several opportunities supported by the results in this study for understanding the effects of mutations or inhibitors specifically on oligomerisation. Moreover, the super-resolution techniques alluded to in Section 1.4.1 can offer significantly improved spatial resolution as well as some level of dynamic information, at timescales insufficient for resolving the molecular mechanism of CDCs but perhaps sufficient for resolving their function in cells [66].

A clear opportunity resulting from the experiments described herein is the combination of sm-fluorescence via labelled monomers and oSCRs via fluorogenic dye in solution. Such experiments could potentially resolve the insertion of the β-barrel relative to oligomerisation of the complex and where applicable to completion of the prepore. Furthermore, the percentage of oligomers that form functional pores could be determined. In this fashion, the capture of assembly presented here will hopefully support further discoveries regarding the CDC protein family.

Chapter 2

Creating a cholesterol-dependent cytolysin sample suitable for single-molecule fluorescence imaging

This chapter describes the synthesis of a CDC protein sample suitable for imaging on a DIB with smTIRF. It starts by outlining the sample requirements for smTIRF, and modifications to the protein primary sequence that were necessary as a result. Starting with a mutated PLY gene, the subsequent methods describe cloning the gene into a new vector, expressing the protein in *E. coli*, purifying it and labelling with a suitable fluorophore. The final sections discuss characterisation of the protein sample to ensure it met the requirements for smTIRF and the study of pore assembly.

The molecular biology methods in this chapter are described in detail: with my background in physics, they were an interesting and important addition to my scientific training and are therefore given thorough consideration. (A report from several Structural Genomics Consortiums [108] and Berg et al. [109] provide useful references.)

2.1 Sample considerations

2.1.1 Required features of the protein sample

As a well-documented member of the CDC family, PLY was chosen as a representative archetype to study CDC assembly [21, 24, 33, 40, 53, 56, 110–114]. Moreover, the necessary expertise for PLY synthesis were accessible via our collaborator R. J. C. Gilbert. The foremost requirement to study PLY assembly by smTIRF was to create PLY monomers labelled with a fluorophore. Following previous success in an αHL study [67], the fluorophore chosen for labelling PLY was Cy3B-maleimide. Cy3B is a rigidified form of Cy3, offering enhanced brightness [115]. It was initially chosen because it is excitable with a common 532 nm laser, exhibits a large Stokes shift between the excitation and emission wavelengths, and yields a strong fluorescence signal (large extinction coefficient of 130,000 $M^{-1}cm^{-1}$ and high fluorescence quantum yield of 0.7) [115]. The maleimide derivative of Cy3B selectively and strongly reacts with the thiol groups of cysteine residues [116].

To support the estimation of stoichiometry from fluorophores in a protein complex (Sections 4.4.2 and 5.3), the ideal sample required monomers labelled with a single fluorophore (1:1 labelled monomers). Doubly-labelled monomers would cause overestimates of stoichiometry. A sample containing unlabelled monomers (equivalent monomers without the fluorophore label) was acceptable, and potentially desirable to avoid self-quenching of the fluorophores (discussed in Section 3.2.2). However, to ensure total control over the imaged sample, an unlabelled fraction was preferably achieved by mixing 100 % 1:1 labelled monomers and unlabelled monomers, rather than using a sample in which the labelling reaction was inefficient. Moreover, a measured labelling efficiency of 100 % gave greater confidence that the labelling proceeded as desired, with monomers conjugated in a 1:1 ratio to the dye, and not with some monomers doubly-labelled and others not labelled.

A second consideration was a homogenously pure sample: any contaminants

present in the sample could influence the apparent mechanism of assembly, and could potentially cause spurious light, lowering the SNR for smTIRF (Section 1.4.1). Furthermore, at the typical 200 nm resolution of smTIRF (550 nm in this study, explained in Section 5.5.2), monomer structure cannot be resolved; complexes must be identified indirectly by the presence of the label (Section 4.1). It was therefore important to independently verify the biological activity of the labelled sample. A haemolytic assay, a standard test for the activity of many PFTs, that exploits their ability to lyse red blood cells, was performed to verify the activity of the PLY sample (Section 2.5.1).

Finally, a step in the imaging protocol described in Chapter 3 required the protein sample to be injected into a droplet with a preformed DIB. The small injected volume (2.3 nl) and the large droplet volume (138 nl) necessitated an initially highly concentrated protein sample (on the order of micromolar), to ensure the monomers were still sufficiently concentrated to assemble into complexes after injection (the optimum concentration is discussed in Section 4.2.2).

2.1.2 Implications for the primary sequence

Creating a PLY sample with the characteristics necessary for smTIRF described above required modifications to the PLY primary sequence. To enable conjugation of the fluorophore to PLY monomers, a cysteine residue was required at an appropriate geometric position on the monomers, for maleimide labelling.

Like many CDCs, the single native cysteine in wild-type PLY resides in the undecapeptide loop highlighted in Figure 1.4 [48, 110]. However, mutation of this cysteine to an alanine had no effect on PLY activity [110]. A PLY mutant was produced, using site-directed mutagensis, with a mutation of the native cysteine at position 428 to an alanine, and a prepended cysteine residue at the N terminus for labelling. This mutant, recombinant pneumolysin, $PLY^{C428A,N\text{-}cys}$ (rPLY), was kindly given to us by our collaborator R. J. C. Gilbert. Geometrically, CDCs bind

with the long axis perpendicular to the membrane [51]. The N-terminus is at the opposite end to the membrane-binding region so attaching a fluorophore here did not affect protein function (as confirmed by haemolysis in Section 2.5.1).

To facilitate purification of the rPLY mutant by immobilised metal ion affinity chromatography (IMAC), for faster purification in fewer steps, a hexahistidine tag (his-tag) was prepended to the primary sequence of rPLY at the N-terminus (Section 2.4). This modification was tested after purification, concomitantly with the presence of the fluorophore, by haemolysis, to ensure that it did not affect the activity of rPLY (Section 2.5.1). The following section describes the addition of the his-tag to rPLY by standard cloning techniques. Subsequently expression, purification and characterisation of the protein sample are described.

2.2 Cloning recombinant pneumolysin

2.2.1 Sequencing the rPLY gene

Before any further modification to the rPLY gene it was sequenced to verify its identity. The gene was initially carried in a pET14b vector and was amplified for sequencing by the following method. The vector was first transformed into DH5α^{TM} *E. coli* cells which are designed for cloning applications and amplify DNA efficiently. Around 500 ng of vector DNA was added to DH5α^{TM} cells thawed on ice. The mixture was kept on ice for 20 minutes, heat shocked at 42°C for 30 seconds and then returned to ice for 10 minutes. 300 µl of Super Optimal broth with Catabolite repression (SOC) media was then added to the mixture, and it was incubated at 37°C for 1 hour.

Following transformation, the cells were streaked onto a Luria-Bertani (LB) agar plate with antibiotic and incubated overnight at 37°C. The pET14b vector carries ampicillin resistance, therefore ampicillin or its more stable semi-synthetic analogue carbenicillin (50 µg/ml) were used as the antibiotic to prevent the growth of other

bacteria on the plate.

A single colony was picked from the plate the following morning and added to 5 ml LB broth with antibiotic. This culture was grown overnight at 37°C in a shaker (180-200 rpm). The pET14b vector was purified from the culture using a Qiagen Miniprep kit, according to the manufacturer's instructions. Some of the DNA was sent with information on the primers (T7 forward and T7 terminator) for sequencing (Source Bioscience Sequencing, Oxford). The rest was stored at -20°C. The sequencing results confirmed that the gene carried in the pET14b vector was the correct rPLY sequence.

2.2.2 A new vector to aid purification

To facilitate fast purification of rPLY in fewer steps, a hexahistidine tag (his-tag) was prepended onto the rPLY gene. This genetic modification was achieved by re-cloning the rPLY into a new vector, the Oxford Protein Production Facility (OPPF) pOPINB vector, which carries an N-terminal his-tag for the inserted protein of interest.

The recombination-based cloning tags suggested for use with HIS6-3C-POI (hexahistidine tag - 3C protease cleavage site - Protein Of Interest) pOPINB vector are aagttctgtttcagggcccg (forward) and atggtctagaaagcttta (reverse). The starting sequence, and base-pair mirrored/reversed final sequence of the rPLY gene are GGCAGCGGCTGTATGGCAAATAAAG and GTCATTTTCTACCTTATCCTC-TACCTGAGGATAG respectively. Therefore, the rPLY gene was first amplified from the pET14b vector by PCR using the primers
5'-aagttctgtttcagggcccgGGCAGCGGCTGTATGGCAAATAAAG-3' (forward) and
5'-atggtctagaaagctttaGTCATTTTCTACCTTATCCTCTACCTGAGGATAG-3' (reverse), ordered from Eurofins MWG Operon. The pET14b vector in the PCR sample was cleaved using methylated-DNA specific enzyme DpnI, because the pET14b vector, being made in bacteria, was methylated unlike the PCR product.

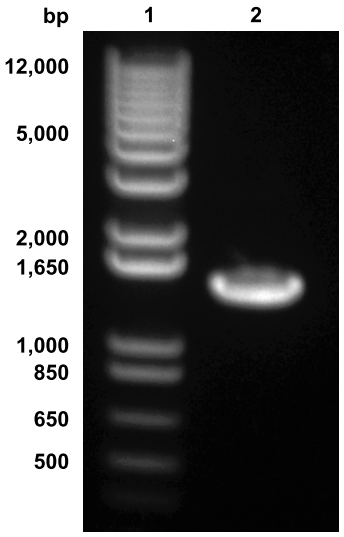


Figure 2.1: Molecular weight of the lifted rPLY gene. Agarose DNA gel to assess the molecular weight of the PCR-amplified rPLY gene from the pET14b vector. *Lane 1*, Molecular weight marker, 1 Kb Plus DNA Ladder from Invitrogen. *Lane 2*, rPLY gene. The rPLY gene has the expected molecular weight: 1,425 base pairs or 475 amino acids (compared to the wild-type with 471 amino acids).

The DNA fragment resulting from PCR amplification was assessed by agarose gel electrophoresis, as illustrated in Figure 2.1, and purified using a Qiaquick PCR purification kit according to the manufacturer's instructions. Meanwhile, the pOPINB vector was cut and linearised using KpnI and HindIII restriction enzymes incubated at 37°C for 2 hours, and also purified using the PCR purification kit. The amplified rPLY gene was inserted into the digested pOPINB vector using In-Fusion^{TM} enzyme to become the new gene, recombinant pneumolysin with a prepended hexahistidine tag, PLY$^{C428A,N\text{-}his\text{-}cys}$ (rPLY^{his}). pOPINB-rPLY^{his} was transformed into DH5α^{TM} cells, according to the OPPF Cloning and Expression Screening standard protocol.

2.2.3 Increasing the volume of DNA

Before using the pOPINB-rPLY^{his} vector to express the rPLY^{his} protein, more DNA was generated, to ensure there was a sufficient amount for sequencing and further iterations of protein expression and purification. The DH5α^{TM} cells transformed with the pOPINB-rPLY^{his} vector from the previous section were

MGSSHHHHHHSSGLEVLFQGPGSGCMANKAVNDFILAMNYDKKKLLTHQ
GESIENRFIKEGNQLPDEFVVIERKKRSLSTNTSDISVTATNDSRLYPGALL
VVDETLLENNPTLLAVDRAPMTYSIDLPGLASSDSFLQVEDPSNSSVRGAV
NDLLAKWHQDYGQVNNVPARMQYEKITAHSMEQLKVKFGSDFEKTGNSL
DIDFNSVHSGEKQIQIVNFKQIYYTVSVDAVKNPGDVFQDTVTVEDLKQRG
ISAERPLVYISSVAYGRQVYLKLETTSKSDEVEAAFEALIKGVKVAPQTEWK
QILDNTEVKAVILGGDPSSGARVVTGKVDMVEDLIQEGSRFTADHPGLPIS
YTTSFLRDNVVATFQNSTDYVETKVTAYRNGDLLLDHSGAYVAQYYITWDE
LSYDHQGKEVLTPKAWDRNGQDLTAHFTTSIPLKGNVRNLSVKIREATGLA
WEWWRTVYEKTDLPLVRKRTISIWGTTLYPQVEDKVEND

Figure 2.2: Amino acid sequence of the cloned rPLY^{his} gene. rPLY was cloned into a pOPINB vector to prepend a histag and create rPLY^{his}. Red (in order): the hexahistidine tag, the 3C protease cleavage site, the N-terminal prepended cysteine residue for labelling, and the alanine residue that replaced the native cysteine at position 428.

streaked onto an LB agar plate containing 35 μg/ml kanamycin, 1 mM isopropyl β-D-1-thiogalactopyranoside (IPTG) and 200 μg/ml 5-bromo-4-chloro-3-indolyl-β-D-galactopyranoside (X-Gal) and incubated overnight at 37°C. IPTG was included to induce expression of the rPLY gene, kanamycin because pOPINB carries resistance to this antibiotic so only cells carrying the pOPINB vector survived on the plate. X-Gal was included to distinguish between colonies where the rPLY gene had been successfully inserted into the pOPINB vector and those where it hadn't: incorporation of a new gene into the vector disrupts the transcription of an enzyme that turns X-Gal blue, so colonies with an inserted rPLY gene remained white. The following morning, only 2 blue colonies were found on a plate full of white colonies.

A white colony was picked from the plate and added to 5 ml LB broth with 35 μg/ml kanamycin. The culture was grown overnight at 37°C in a shaker (180-200 rpm). The pOPINB-rPLY^{his} vector was purified using a Qiagen Miniprep kit according to the manufacturer's instructions. The final concentration of DNA was 130 ng/μl, dissolved in around 50 μl of Milli-Q® water (MQ). Some of this DNA was sent for sequencing to confirm its identity, the rest was stored at -20°C. The sequencing result for the rPLY^{his} gene is shown as an amino acid sequence in Figure 2.2.

2.3 Expression of rPLY^{his}

2.3.1 Bacterial culture

The newly created rPLY^{his} gene, including a his-tag for purification as well as the N-terminal cysteine residue for labelling and an alanine at position 428 instead of the native cysteine, was expressed in *E. coli* to produce large quantities of rPLY^{his}.

The pOPINB-rPLY^{his} vector made in the previous section was thawed and approximately 300 ng was used to transform *E. coli* BL21 Star^{TM} cells, which are more suited to protein expression, according to the protocol described in Section 2.2.1. These cells were streaked onto an LB agar plate supplemented with 50 μg/ml kanamycin and the plate was incubated overnight at 37°C.

The following day, a single colony of the BL21 Star^{TM} cells was picked and added to 200 ml of LB broth supplemented with 35 μg/ml kanamycin in a covered conical flask. This pre-culture was incubated at 37°C overnight in a shaker (180-200 rpm). The pre-culture was diluted into 8 litres of LB broth supplemented with 35 μg/ml kanamycin, split into 1 l conical flasks, the dilution bringing the cells out of stasis. The 8 l culture was incubated at 37°C, 180-200 rpm until it reached an optical density (OD) of 0.5-0.6, measured at a wavelength of 600 nm. 1 mM IPTG was then added to the culture to induce expression of the rPLY^{his} gene and the culture was grown under the same conditions for a further 4-5 hours. The culture was centrifuged at 5000 rpm for 30 minutes, the supernatant was discarded (disinfected with Virkon®), and the pelleted cells were frozen in liquid nitrogen and stored at -80°C. The pelleted cells contained large amounts of expressed rPLY^{his}, ready for purification.

2.3.2 Expression trial

The expression of rPLY^{his} described in the previous section was verified by sodium dodecyl sulfate polyacrylamide gel electrophoresis (SDS-PAGE), as shown in Figure

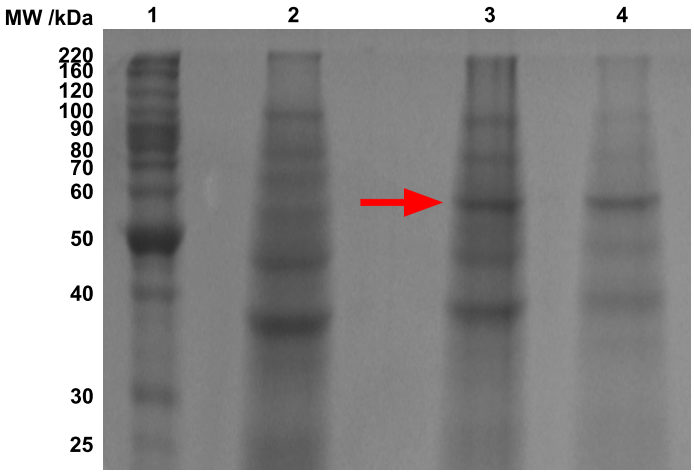


Figure 2.3: Expression trial for detection of rPLY^{his} in bacterial culture. SDS-PAGE to assess the level of rPLY^{his} expression in various *E. coli* BL21 Star^{TM} cultures. *Lane 1*, Molecular weight marker, BenchMark^{TM} Protein Ladder from Life Technologies. *Lane 2*, Control: glucose-inhibited expression. *Lane 3*, Pre-culture, leaky expression without induction by IPTG. *Lane 4*, Culture, after 4-5 hours of expression induced by IPTG. The red arrow indicates the rPLY^{his} band at roughly 53 kDa in the pre-culture and culture. The other bands in the gel correspond to other macromolecules expressed in significant quantities by the *E. coli*; they were subsequently removed from the sample during purification.

2.3. A culture of the same cell type with glucose-inhibited expression was used as a control. The gel shows that rPLY^{his} was also expressed in the pre-culture even without IPTG-induction ('leaky' expression, lane 3). Induction by IPTG appeared only to have a small effect on expression, with the density of the 53 kDa band being only slightly higher relative to the background total protein extract in lane 4 compared to lane 3.

2.4 Purification and labelling

2.4.1 Purification by liquid chromatography

The rPLY^{his} expressed in Section 2.3.1 was extracted from the cells in the pellet and purified before labelling with the fluorophore, to ensure contaminants were not present in the final sample.

The pelleted cells from Section 2.3.1 were resuspended in phosphate-buffered saline (PBS) (10 mM phosphate buffer, 2.7 mM potassium chloride, 137 mM sodium

chloride, pH 7.4) with 1 mM dithiothreitol (DTT) and 20 mM imidazole. DTT was added to buffers throughout the purification process to reduce the thiol group of the labelling cysteine residue and prevent intermolecular disulphide bonds from forming; it was removed prior to labelling to allow the thiol to oxidise during reaction with the maleimide group of Cy3B-maleimide (Table 2.1). Imidazole was added to the resuspension buffer in preparation for the first chromatography step.

The resuspended cells were lysed by sonication, then centrifuged for 1 hour at 19,000 rpm to separate cell debris. The resulting supernatant contained the soluble fraction of the cell lysate, including $rPLY^{his}$. It also contained many other molecular species and so was subsequently purified by liquid chromatography in a series of steps that are summarised in Table 2.1.

In liquid chromatography, a sample is purified based on the strength of adsorption of its constituent parts onto a solid surface. The solid material is typically packed into a column. The sample is passed through the column and the parts are separated as they interact with the material inside [108, 109]. The liquid chromatography described herein was facilitated by the use of an ÄKTA protein purification system from GE Healthcare Life Sciences.

At each step the column was first equilibrated in MQ, then buffer 'A' (Table 2.1), before the sample was loaded onto the column. At the start of each step, the sample containing $rPLY^{his}$ was dissolved in the buffer that it was eluted with or finished in during the previous step; for the first immobilised metal ion affinity chromatography (IMAC) step the sample was initially in the resuspension buffer described above. Once the sample was loaded onto the column, the protocol differed for each step.

For the first, IMAC step, the sample was loaded onto a column containing immobilised nickel ions, because his-tags have a strong affinity for nickel. The $rPLY^{his}$ bound strongly to the nickel ions while other molecules in the soluble lysate washed through: 20 mM imidazole was included in buffer A to remove

Purification step	**Column**	**Buffer A**	**Buffer B**
immobilised metal ion affinity	GE HisTrap HP, 5 ml	PBS, 1 mM DTT, 20 mM imidazole	PBS, 1 mM DTT, 1 M imidazole
buffer exchange	GE disposable PD-10 desalting column	PBS^-, 1 mM DTT	-
anion exchange	GE HiTrap Q HP, 5 ml	PBS^-, 1 mM DTT	PBS^-, 1 mM DTT, 1 M NaCl
concentration and filtering	Millipore Amicon® Ultra-4 centrifugal filter unit, 10 kDa MWCO; Millipore Ultrafree®-MC 0.5 ml centrifugal filter unit, 0.22 μm		
size exclusion	GE Superdex 200 10/300 GL	PBS	-
	– labelling –		
anion exchange	GE HiTrap Q HP, 5 ml	PBS^-, excess DTT	PBS^-, 1 M NaCl
buffer exchange	GE disposable PD-10 desalting column	1 M KCl, 10 mM HEPES, 0.1 mM EDTA	-
concentration and filtering	Millipore Amicon® Ultra-4 centrifugal filter unit, 10 kDa MWCO; Millipore Ultrafree®-MC 0.5 ml centrifugal filter unit, 0.22 μm		

Table 2.1: Chromatography steps: purifying and labelling $rPLY^{his}$. Mechanisms of purification and the columns and buffer solutions used in each purification step are listed. PBS: 10 mM phosphate buffer, 2.7 mM KCl, 137 mM NaCl. PBS^-: 8 mM Na_2HPO_4, 1.5 mM KH_2PO_4, 2.5mM KCl. All buffers were at pH 7.4. MWCO, molecular weight cut-off. The table is usefully interpreted together with Figure 2.4. See text for details.

non-specifically bound molecules from the column. To elute the $rPLY^{his}$ from the column, an imidazole gradient was applied from 20 mM up to 1 M, by increasing the percentage of buffer 'B' in the solution pumped through the column. At around 100 mM, the imidizole out-competed the $rPLY^{his}$ for binding to the nickel ions and the protein was eluted and collected in fractions. The UV absorbance of the elution

from the column was measured and the result is shown in Figure 2.4, peak i. A large peak in the UV absorbance indicated the exit of $rPLY^{his}$ from the column. The imidazole gradient is also represented in Figure 2.4, in terms of % buffer B.

A similar principle was applied during the third, anion exchange purification step (Table 2.1), and the elution UV absorbance profile and gradient is presented in Figure 2.4, peak ii. In anion exchange chromatography, the column is packed with a resin with positively charged chemical groups, so that negatively charged molecules bind to the resin. The protein bound to this column in buffer A (Table 2.1) but was displaced when a gradient of increasing NaCl concentration was applied (Table 2.1, Figure 2.4, peak ii).

The desalting column used for buffer exchange in the second purification step employed a different principle: molecules in the sample were separated according to their size. Desalting columns are packed with spherical particles made from a porous matrix material. Large molecules such as proteins penetrate the porous matrix relatively poorly, they pass through the column quickly. Small molecules including salts penetrate the porous matrix significantly, and are therefore retarded by it to a greater extent. These differing flow rates are exploited to swap the buffer solution solvating the protein. The PD-10 desalting column was used in 'gravity' mode in this study, according to the manufacturer's instructions.

Size exclusion chromatography (SEC) employs the same principle as a desalting column, except a different porous matrix is used and the column is longer. SEC can separate different macromolecular species based on size: the separation resolution is far greater than for the desalting column. This technique was used to purify $rPLY^{his}$ further, and to exchange buffer solution again prior to labelling: the sample was exchanged into PBS without DTT, so that the cysteine thiol groups could oxidise during the labelling reaction with the maleimide group of the dye. The SEC elution is shown in Figure 2.4, peak iii. SEC separates molecular species by size and not chemical properties, so no chemical gradient was applied in this step.

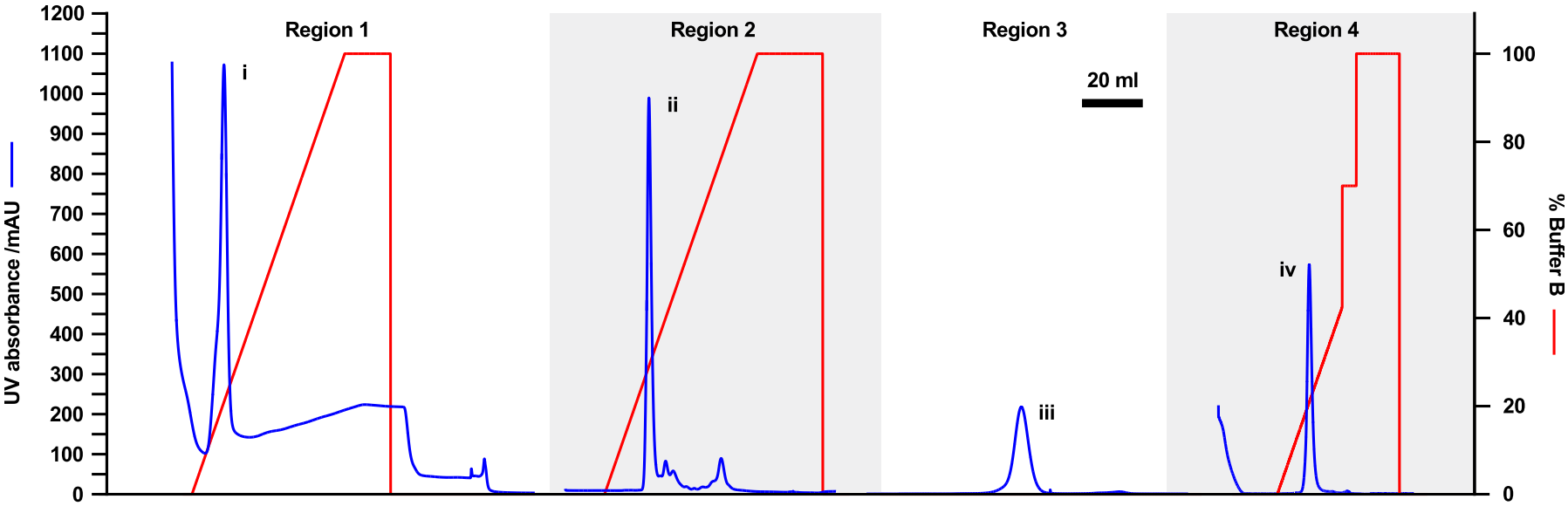


Figure 2.4: Elution profile from several purification steps. UV (280 nm) absorbance measurements of the solution eluted from a column during purification and, where applicable, the chemical gradient applied to induce elution of the protein in terms of % buffer B (see Table 2.1 for buffer solutions used in each step). The separate regions should be interpreted in conjunction with Table 2.1. *Region 1*, Elution from the nickel IMAC column under an imidazole gradient. The large UV absorbance preceding the protein elution is due to the excess of other molecular species in the cell lysate, eluted in buffer A in this first purification step. The imidazole itself absorbs in the UV, hence the increasing background absorbance in proportion to % buffer B. *Region 2*, Elution from the anion exchange column under an NaCl gradient. *Region 3*, Elution from the size exclusion column. *Region 4*, Elution from the second anion exchange purification step, to remove excess free dye from the labelled lPLY sample; the tail preceding peak *iv* is the last of the free dye, which has some absorbance in the UV range, exiting the column. In each region, the elution of protein from the column is represented by a peak in UV absorbance (peaks *i-iv*). $rPLY^{his}$ was labelled between the third and fourth region. The x-axis in this figure is in units of millilitres, and represents solution flowing out of the columns. This unit is synonymous with time, increasing from left to right, except that the flow rate in ml/min was not constant for each purification step.

Immediately following elution from the SEC column, the protein's concentration was determined ready for labelling. Without DTT in the buffer to reduce the thiol group, intermolecular disulphide bonds could begin to form between monomers, rendering them useless for PLY assembly studies. Labelling was therefore performed as quickly as possible following elution of the protein sample from the SEC column.

2.4.2 Labelling trial

Prior to the SEC step in Table 2.1, the labelling protocol was tested by labelling a small amount of $rPLY^{his}$ with 5 kDa polyethylene glycol (PEG)-maleimide, a polymer with a prescribed molecular weight and an attached maleimide group similar to the Cy3B-maleimide that was used to fluorescently label the protein (see Section 2.1.1 for the choice of dye). In preparation for the labelling trial a desalting column was used to remove DTT from the sample.

Figure 2.5 shows that successful labelling was achieved when a 10-fold molar excess of PEG-maleimide, dissolved in dimethyl sulfoxide (DMSO), was added to $rPLY^{his}$ in PBS at pH 7.4, and incubated at room temperature for 15 minutes. The large majority of $rPLY^{his}$ was successfully labelled in this reaction, but the reaction was not 100 % efficient as evidenced by the band that persisted at 53 kDa following labelling. The extent of labelling was deemed sufficient to attempt labelling with Cy3B-maleimide under the same conditions. The volume of DMSO added was less than 1 % of the total volume of solution in the reaction. The labelling reaction was quenched in this trial by dilution into SDS-PAGE loading buffer, which contained an excess of reducing agent, to prevented any further oxidation of the thiol groups.

2.4.3 Labelling and subsequent purification

$rPLY^{his}$ was fluorescently labelled immediately after further purification and removal of DTT from the buffer solution by SEC. A 10-fold molar excess of Cy3B-maleimide was added to the protein sample, the maleimide group reacting with

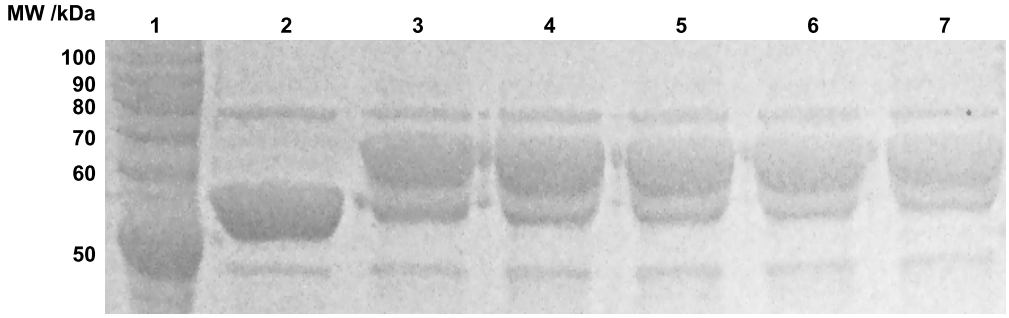


Figure 2.5: Measuring the extent of PEG labelling of rPLY^{his} by SDS-PAGE. *Lane 1*, Molecular weight marker. *Lane 2*, Unlabelled rPLY^{his} (53 kDa). *Lanes 3-7*, rPLY^{his} following addition of a 10-fold molar excess of PEG-maleimide (5 kDa) for labelling of the protein molecule, at 7.5, 15, 30, 60 and 120 minutes respectively. The rPLY^{his} band shifted to around 58 kDa after the addition of 5 kDa PEG, as expected for successful labelling. The labelling reaction was complete after around 15 minutes (lane 4), but not all the rPLY^{his} became labelled as indicated by the band that persisted at 53 kDa in lanes 3-7. This trial was conducted before the SEC purification step to test the labelling conditions, hence some impurities at 80 and 50 kDa were still present in the sample.

the thiol on the cysteine residues to create 1:1 labelled recombinant pneumolysin, PLY$^{C428A,N\text{-}his\text{-}cys}$-Cy3B (lPLY). The reaction was allowed to proceed for 15 minutes at room temperature, in PBS at pH 7.4. The volume of Cy3B-maleimide dissolved in DMSO added to the rPLY^{his} solution was kept under 1 % of the total volume of solution in the labelling reaction. The reaction was quenched by addition of a 100-fold molar excess of DTT and reducing the reaction temperature to 4°C.

After labelling, excess free dye was removed by another anion exchange purification step. The free dye eluted from the column in buffer A (Table 2.1). The UV absorbance elution profile is shown in Figure 2.4, peak iv.

Finally, the buffer solution was again exchanged, to 1 M KCl, 10 mM HEPES, 0.1 mM EDTA at pH 7.4, for storage of the protein sample until it was characterised for activity, labelling and purity (Section 2.5), or used in imaging experiments.

In the UV absorbance plots in Figure 2.4 the important quantity at each purification step was the area under the peak, which was representative of the total quantity of protein exiting the column. The area under the peak became smaller after each purification step: some protein molecules were not retained whenever the sample passed through any sort of filter/column, but also, due to the large quantity

of expressed protein, not all of the protein was carried forward at every step.

2.4.4 Monitoring protein purity

After each purification step the elution was collected into separate fractions. The fractions of interest corresponding to the UV absorbance peaks i-iv in Figure 2.4, putatively containing $rPLY^{his}$ or lPLY, were assessed for molecular weight to understand their molecular composition. The resulting SDS-PAGE gels are presented in Figure 2.6.

During the first purification step by IMAC, a large number of molecules from the cell lysate washed through the column before the imidazole gradient was applied (the eluate with large UV absorbance preceding peak i in Figure 2.4). Figure 2.6A demonstrates that the 53 kDa $rPLY^{his}$ was in vast excess, relative to other molecular species, in the fractions of interest collected from the IMAC column. However, impurities did elute with the $rPLY^{his}$.

Panels B and C from Figure 2.6 show the purity of the fractions of interest exiting the first anion exchange column and the SEC column respectively (peaks ii and iii from Figure 2.4). $rPLY^{his}$ became increasingly pure with each step. Finally, for completeness, the lPLY fractions from the second anion exchange step (peak iv in Figure 2.4) are shown in Figure 2.6D. Figure 2.6 indicates that $rPLY^{his}$ or lPLY was present in the fractions of interest after every chromatography step described above, and was almost pure to homogeneity by the final step. Following purification, lPLY was characterised before imaging experiments were performed.

2.5 Characterisation of labelled PLY

Figure 2.6D demonstrates that by the end of the purification process, lPLY was almost homogeneously pure. Most importantly, the protein was sufficiently pure for sm-fluorescence studies without concern for contaminants reducing the SNR

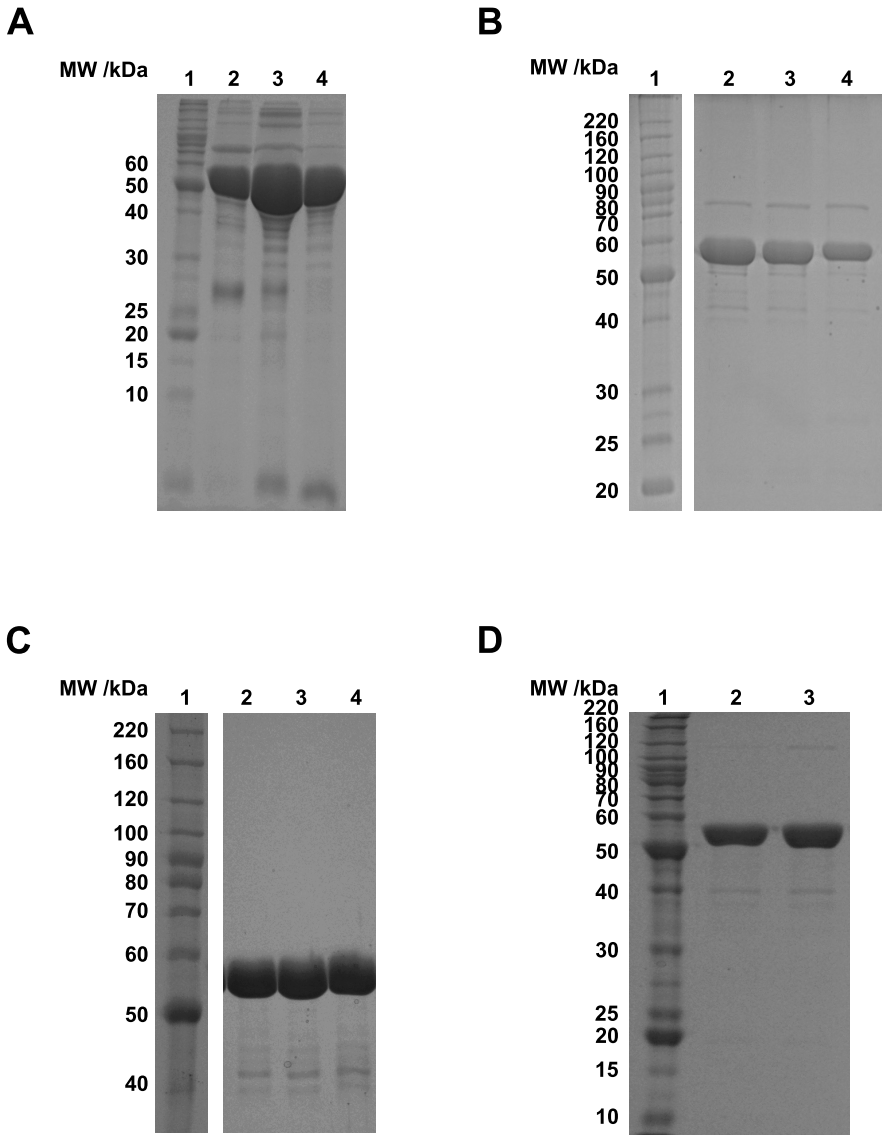


Figure 2.6: Purity of eluate after each chromatographic step. SDS-PAGE was used to assess the presence of rPLY^{his}/lPLY in collected fractions eluted in the various chromatography steps from Table 2.1, as well as the relative amounts of other molecular species in these fractions. *A-D* correspond to the fractions of interest eluted from the IMAC, first anion exchange, SEC and second anion exchange purification steps, respectively, and to peaks *i-iv* in Figure 2.4, respectively. In each panel, lane 1 is a molecular weight marker and the other lanes are a set of neighbouring collected fractions centred on the peaks *i-iv* from Figure 2.4. The large band at 53 kDa in each panel is due to rPLY^{his} (*A-C*) or lPLY (*D*). The gels highlight the rPLY^{his} or lPLY becoming progressively purer.

during smTIRF or influencing the assembly process. The labelling efficiency and the biological activity of lPLY remained to be assessed, to validate any interpretations of assembly data.

2.5.1 Confirmation of biological activity

The biological activity of lPLY was assessed by haemolytic assay, which measures the protein's ability to lyse red blood cells by their optical density (OD). Lysed cells turned translucent (low OD), intact cells remained opaque and cloudy (high OD). Figure 2.7 illustrates rabbit red blood cells being lysed by wild-type PLY and lPLY.

PLY was serially diluted by a factor of 2 from 10 nM along the columns of a 96-well plate. Each filled row contained a unique PLY sample. Red blood cells suspended in PBS were added to the wells using a multichannel pipette, to synchronise the reaction start time for the row, and the lysis reaction was allowed to proceed for 35 minutes. The OD of the wells was measured throughout lysis using a plate reader. The assay was performed with newly thawed wild-type PLY and was repeated for lPLY 5 days after the final lPLY purification step in Section 2.4 and then again 37 days after the final purification step (lPLY was stored at 4°C).

The serial dilution enabled an accurate estimate of the protein concentration below which lysis could not occur. A loss of lytic activity for a constant concentration could potentially be caused by aggregation and denaturation over time, the genetic mutations and prepended his-tag introduced to lPLY, or the fluorophore label creating some sort of steric hinderance.

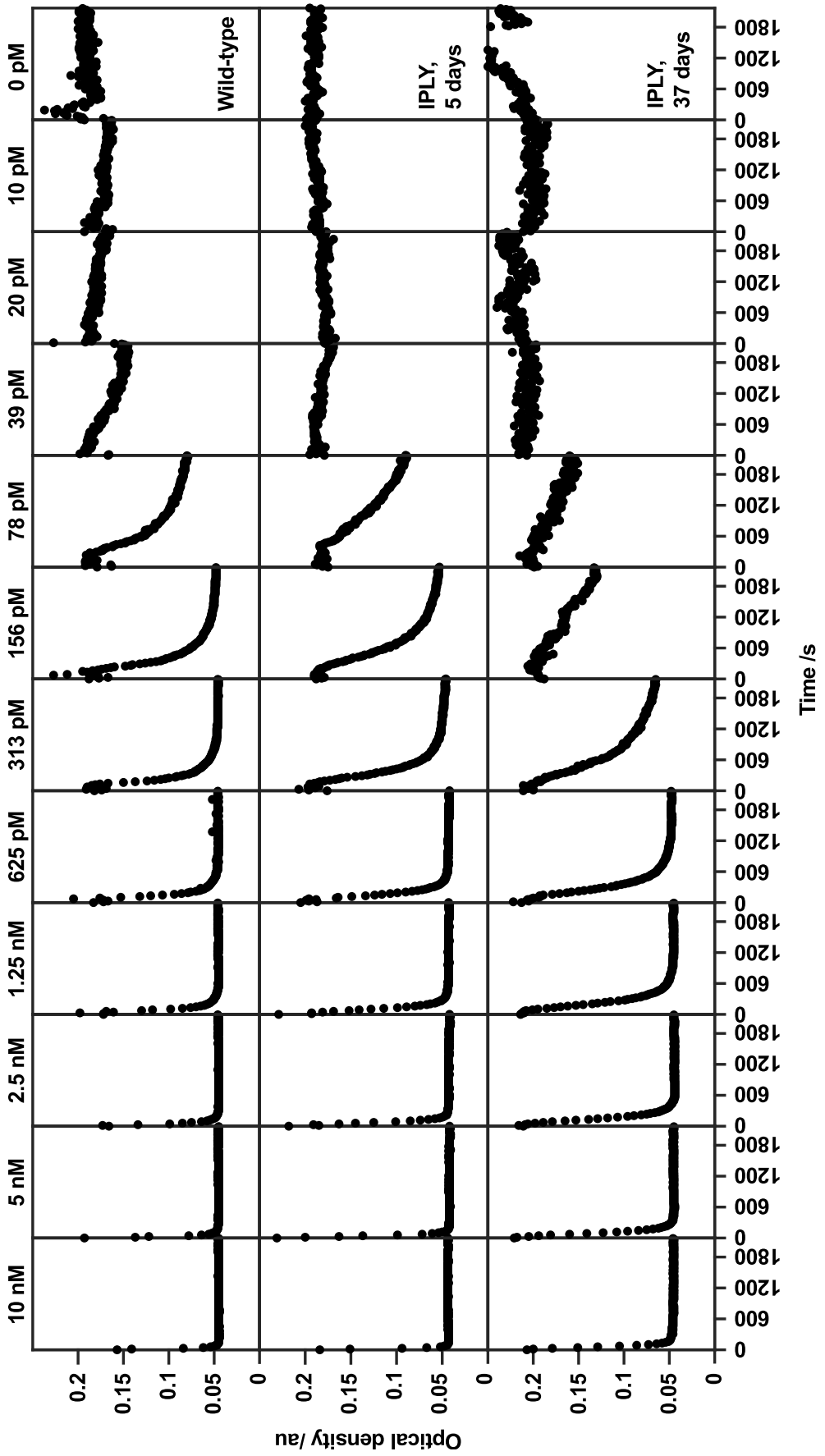

Wild-type
IPLY, 5 days
IPLY, 37 days
10 nM
5 nM
2.5 nM
1.25 nM
625 pM
313 pM
156 pM
78 pM
39 pM
20 pM
10 pM
0 pM
Optical density /au
Time /s
0
0.05
0.1
0.15
0.2
600
1200
1800

Figure 2.7: Haemolysis assay demonstrates protein activity. Each graph represents one well of a 96-well plate, to which was added 100 µl of rabbit red blood cells and 100 µl of protein solution (each row is actually data from a different day). Columns left to right: final protein concentration decreasing by a factor of 2 from 10 nM, last column is a no-protein control. *First row*, Wild-type PLY, thawed and filtered on the same day as the assay. *Second row*, lPLY, 5 days after the final purification step in Table 2.1. *Third row*, lPLY, 37 days after the final purification step in Table 2.1; the lPLY concentration was re-checked before the assay in row 3 and found to be 0.95× that in row 2. The figure shows that 37-day old lPLY was the least active of the three samples, wild-type the most active, but that 5-day old lPLY was essentially as active as the wild-type to within the error in protein concentration measurements. Lytic capabilities were completely lost at 40 pM (column 9).

Figure 2.7 shows that both wild-type PLY and lPLY were haemolytically active, because at sufficiently high concentrations both proteins caused the OD of red blood cells to drop. The activity of lPLY 5 days after purification was the same as the activity of the wild-type protein, to within the error on protein concentration measurements, giving confidence that the mutations and fluorophore label introduced to lPLY were not interfering with the natural protein function. Moreover, most lPLY activity was retained over the course of 32 days at 4°C (row 3 compared to row 2), although some activity was lost (compare the rows in column 7, 156 pM, for example, where the older sample exhibits reduced lysis for equivalent concentration).

2.5.2 Measuring the extent of labelling

The lPLY labelling efficiency - the percentage of monomeric protein tagged with a fluorophore during the labelling reaction, assuming a 1:1 ratio - was assessed by UV absorbance. As discussed in Section 2.1.1, 100 % labelling with a 1:1 fluorophore:protein ratio was desirable, to give confidence in the labelling procedure and to allow for controlled mixing of labelled and unlabelled protein during imaging experiments. Characterising the extent of labelling was important for estimating the stoichiometry of CDC complexes using fluorophores (Sections 4.4.2 and 5.3).

SDS-PAGE gels imaged under UV light gave a preliminary indication that the labelling reaction was successful (Figure 2.8). Cy3B exhibits some absorbance in the

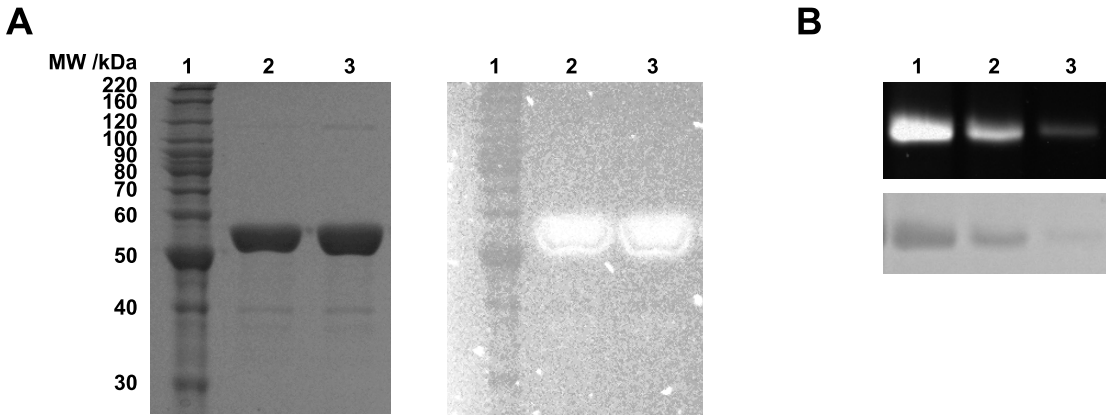


Figure 2.8: Cy3B-labelled PLY detected by a UV gel. *A*, Gel from Figure 2.6D imaged under white light (left) and UV light (right). The band at 53 kDa is lPLY. The gels illustrate that the sample is pure and labelled. *B*, A different Cy3B-labelled PLY sample imaged under UV light (top) and white light (bottom), demonstrating the achievable fluorescence signal from Cy3B in a UV gel imaged immediately, compared to the week-old gel in *A*.

UV range (see Figure 2.9), so bands on a gel that contained Cy3B-labelled protein fluoresced under UV light. Figure 2.8A shows the same gel as Figure 2.6D, imaged under UV and white light. This UV image was captured a week after running the gel; the gel was stored in day light, so the fluorescent signal is weak due to many Cy3B molecules having photobleached (Section 4.4). Figure 2.8B shows a different Cy3B-labelled PLY sample; this UV image was taken immediately after running the gel so the fluorescent signal from Cy3B was stronger.

The efficiency of the labelling reaction was measured using the absorbance spectrum of lPLY, which is presented in Figure 2.9. The protein alone absorbs strongly at 280 nm, while Cy3B absorbs weakly at 280 nm and strongly at 559 nm. The absorbance of Cy3B at 280 nm, relative to its absorbance at 559 nm, was measured as $\delta = 0.13$ (the value in the Amersham Cy3B manual is $\delta = 0.08$). The labelling efficiency was calculated using Equation 2.1.

$$\frac{[\text{labelled protein}]}{[\text{total protein}]} = \frac{A_{\max} * \epsilon_{\text{protein}}}{(A_{280} - \delta * A_{\max}) * \epsilon_{\text{dye}}} \tag{2.1}$$

ϵ represents the extinction coefficient of the denoted species. The extinction coefficient of PLY is 72,080 $M^{-1}cm^{-1}$, that of Cy3B is 130,000 $M^{-1}cm^{-1}$. A_{max} refers

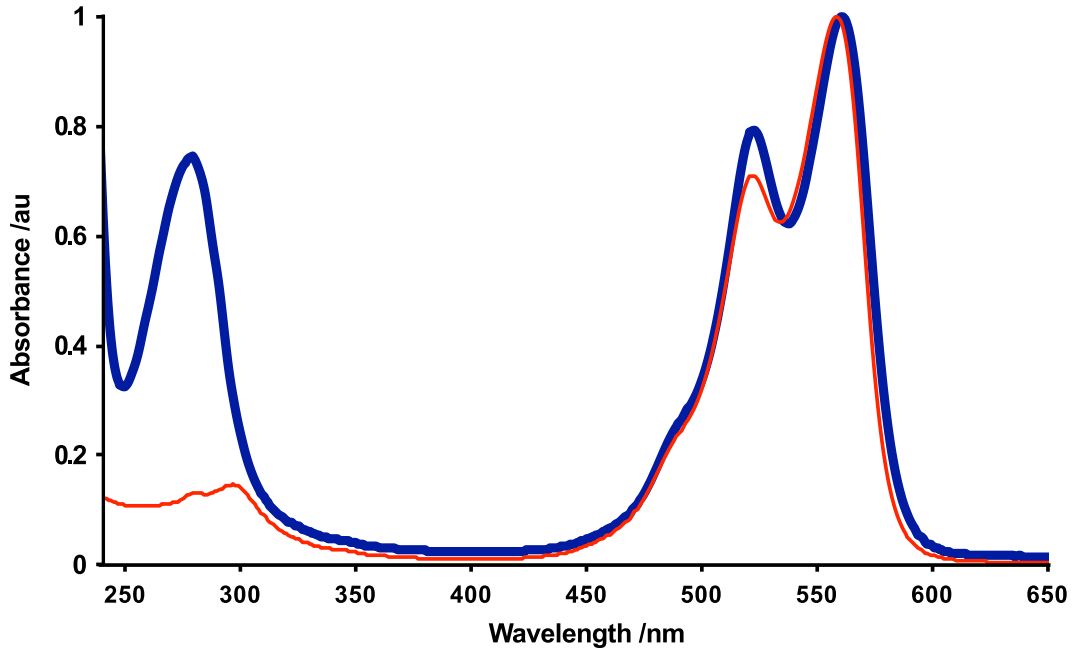


Figure 2.9: Absorbance spectrum of Cy3B and lPLY. *Blue*, normalised lPLY absorbance; the peak at 280 nm is due to the protein, the double-peak at 559 nm is due to the Cy3B-maleimide label. *Red*, normalised Cy3B only absorbance, in the same buffer as lPLY.

to the relative absorbance of the dye at the wavelength with maximum absorbance: for Cy3B-maleimide this is A_{559}. $\delta = 0.13$ is the previously mentioned correction factor. From the absorbance spectrum in Figure 2.9, the labelling efficiency for lPLY was calculated to be 91 %.

Assuming some measurement error from the spectrophotometer, which was not characterised, the labelling efficiency was close to 100 %. The slight deficit was predicted by the PEG labelling trial in Section 2.4.2, where not all the $rPLY^{his}$ became labelled with PEG. The efficiency being close to 100 % suggested that the majority of monomers were labelled with a single fluorophore, rather than a significant population of both unlabelled and over-labelled monomers (though this was impossible to explicitly determine with the bulk absorbance assay), and therefore from a labelling perspective the sample was suitable for smTIRF experiments.

Ultimately, capture of CDC assembly was mostly performed with labelled PFO received from a collaborator (discussed in Section 3.2.2), and not this lPLY sample.

2.6 Summary of the labelled PLY sample

This chapter described the production of a protein sample suitable for imaging CDC assembly at the single-molecule level. The rPLY gene received from our collaborator had been modified to facilitate 1:1 labelling in a position that would not interfere with biological function. The gene was re-cloned into a new vector with an N-terminal his-tag to facilitate purification. The protein was expressed in *E. coli* cells and purified using standard liquid chromatography techniques. It was then labelled with Cy3B-maleimide and purified again to remove free dye. A large quantity of protein was synthesised: at some stages, not all of the protein was carried forward due to the difficulty in handling such large quantities. The final lPLY sample aliquoted and stored at 4°C, or frozen in liquid nitrogen and stored at -80°C, was 0.5 ml of 20 μM lPLY, after concentration and filtering (Table 2.1). It was stored in 1 M KCl, 10 mM HEPES, 0.1 mM EDTA at pH 7.4.

The lPLY sample was characterised in terms of its biological activity, its purity and the ratio of labelled to total protein. It was found that lPLY was as active as wild-type PLY, around 91 % labelled, almost pure to homogeneity and sufficiently concentrated for injecting into a droplet with a DIB. Thus, it was deemed suitable for sm-fluorescence imaging of CDC assembly on a DIB. In line with the overall goal of quantifying CDC assembly, the next step was to establish an imaging protocol: to ensure that lPLY was active on a DIB, that the imaging experiments were reproducible, and that the fluorescence signal collected from the labelled protein was sufficient to characterise assembly. The imaging protocol is discussed in the next chapter.

Chapter 3

Optimising bilayer construction and imaging for the study of cholesterol-dependent cytolysins

The focus of this chapter is establishing a reproducible protocol for imaging lPLY on a DIB. The protocol includes construction and customisation of the DIB, the exposure settings and arrangement of the sample for smTIRF, and verification of the protein's functionality in a DIB by electrophysiology and optical single-channel recording (oSCR). A PFO sample received from our collaborator is also introduced, as this sample was used to obtain the majority of the results concerning assembly in Chapter 4.

3.1 Droplet interface bilayer construction

DIBs were chosen as the artificial bilayer system with which to capture CDC assembly via smTIRF, for reasons fully discussed in Section 1.5. DIBs are simple to make, versatile and stable [99], and can be interrogated electrically as well as optically [102]. They therefore make an excellent tool for the study of pore-forming proteins, whose function naturally causes a change in conductivity of the target

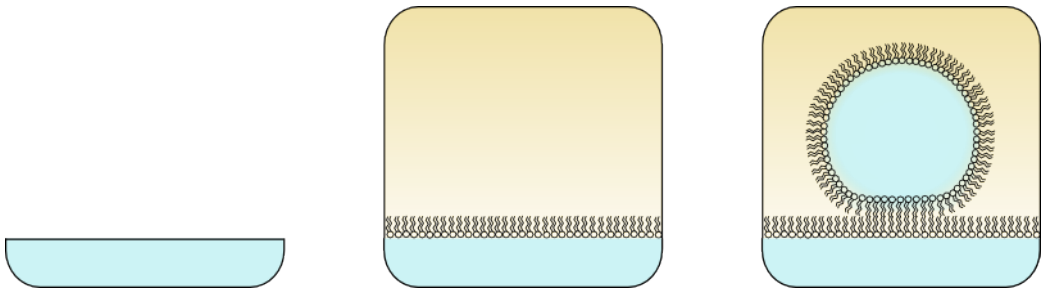


Figure 3.1: Principles of DIB construction. Lipid-in-oil is applied to a spin-coated hydrogel substrate and the lipids form a monolayer at the aqueous-oil interface. A monolayer similarly formed on an aqueous droplet is brought into contact with the hydrogel monolayer and the two monolayers fuse to form a bilayer.

membrane. This section describes the construction of DIBs that are compatible with the study of CDCs.

Figure 3.1 illustrates the basic principle for constructing a DIB. The first step was making the lipid in oil solution: lipids stored in chloroform at -20 °C were dried under vacuum and redissolved in hexadecane, or hexadecane with 10 % silicone oil. The lipid solutions were heated to 37°C to ensure thorough mixing. The choice of lipids is discussed in Section 3.2.1, but for CDC experiments a base lipid and cholesterol were a minimum requirement. To create an asymmetric bilayer, the hydrogel monolayer was formed from lipid solution 'A' and the droplet monolayer was formed from a different lipid solution 'B'.

Next, the bespoke plastic device used to host droplets during imaging was prepared. This device is illustrated in Figure 3.2; it was specially designed to permit high-throughput DIB imaging [99]. Each of the 16× 0.5 mm bottomless wells in the device hosted a single droplet during experiments.

To prepare this device, 140 µl of 0.75 % ultra-low melt agarose in MQ was first heated to 90°C and then spin-coated on to a glass coverslip. The coverslip was placed in the 0.2 mm recess on the underside of the device, with the coated face towards the device, and the borders were sealed with tape. The spin-coated coverslip then formed the base of the 0.5 mm wells; the agarose layer was sufficiently thin to allow a DIB resting on it at the base of a well, imaged from below with an inverted

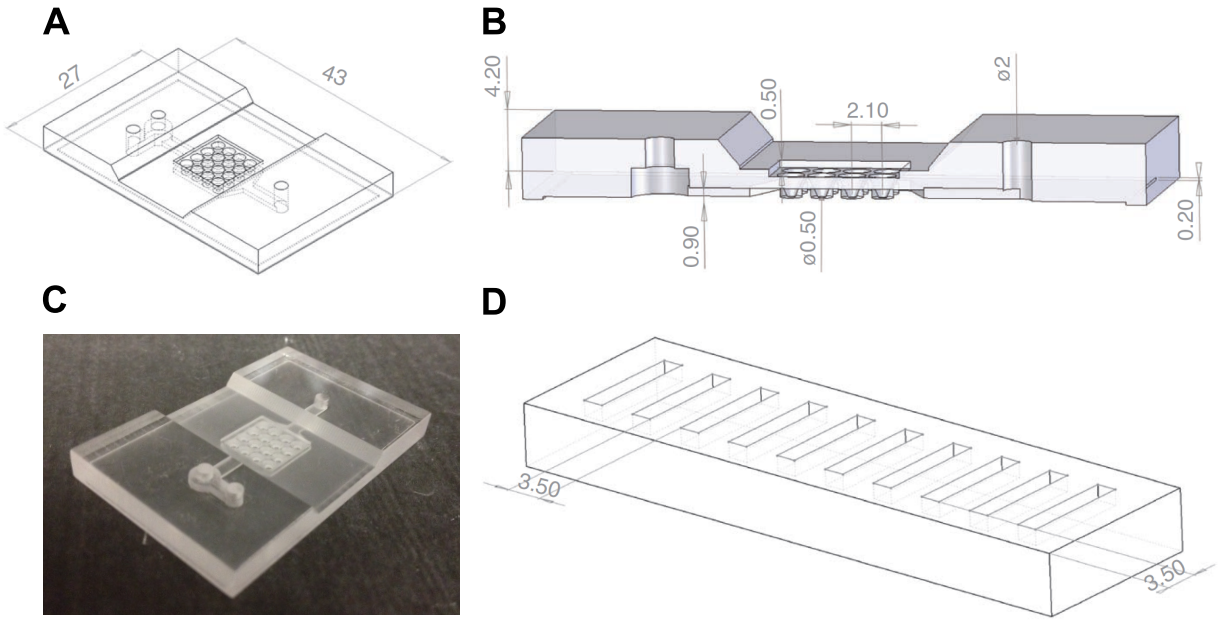


Figure 3.2: A bespoke droplet holder. *A-B*, The poly(methyl methacrylate) (PMMA) device used to hold droplets during imaging experiments was designed using computer-aided design software and machined using computer numerical control (CNC) [99]. *C*, A photograph of the PMMA device. *D*, The CNC machined PMMA incubation chambers (×10), in which droplets were incubated with lipid-in-oil solution to form a monolayer. Adapted from [99].

objective lens, to be illuminated by a 200 nm-depth TIRF evanescent field (Section 1.4.1). (The depth of TIRF field was not calibrated in this study.)

Around 200 µl of 1.8 % low melt agarose in buffer solution 'A', heated to 90°C, was pipetted into the single 2 mm hole in the thick part of the device, flowing through the machined-out channel underneath the device in between the wells, until it just overflowed from the two 2 mm holes on the opposite side. The thicker agarose rehydrated the spin-coated agarose mesh on the coverslip, producing a hydrogel of buffer solution at the base of the wells [99]. (The second asymmetric 2 mm hole on one side of the device was incorporated as an escape conduit for the molten thicker agarose, for experiments where an electrode was placed into the first of these two holes at this point in the procedure, Section 3.4.1.) The agarose was allowed to set for 30 seconds, and any excess protruding from the 2 mm holes was scraped away and the holes sealed with tape to prevent dehydration.

Around 50 µl of lipid solution A was pipetted onto the top of the 16 wells

until the wells and the 0.5 mm recess above them were filled. The device was incubated at room temperature for 2 hours to allow a lipid monolayer to form at the interface between the hydrogel and the oil phase (without a large fraction of cholesterol present, Section 3.2.1, the incubation time could be as short as 15 minutes).

Meanwhile, the incubation chambers illustrated in Figure 3.2D were filled with approximately 25 µl each of lipid solution B. Around 20× 138 nl droplets of buffer solution 'B' were injected directly into the incubation chambers using a nanolitre microprocessor-controlled injector (Nanolitre 2010, WPI, Figure 3.7). The droplets were incubated for 2 hours at room temperature to allow monolayers to form at the droplet-oil interface.

In different methodologies, the protein could be dissolved in buffer solution B as the droplets were made, or injected into the droplet after bilayer formation; in CDC assembly experiments, the latter was chosen to eliminate interaction of the CDC with cholesterol, and initiation of assembly, before the bilayer could be imaged.

Following incubation of the monolayers, the 138 nl droplets were pipetted into the wells in the device, one droplet per well, where they sank under gravity to the base of the well. After some time, depending on the lipid concentration, the hydrogel and droplet monolayers fused to form a DIB. Figure 3.3 shows the appearance of the droplet resting at the base of the well pre- and post-bilayer formation.

The whole device including droplets was incubated for 30-40 minutes at 37°C to encourage equilibration of the asymmetric monolayers (Section 3.2.1), before the device was transferred to the microscope stage. Using an inverted 20× objective lens to help view the tip of the injector, a small 2.3-4.6 nl volume of buffer solution A was fused with the hydrogel at the bottom of each well prior to imaging (in a part of the well that did not interfere with the 138 nl droplet). This fused volume rehydrated the hydrogel supporting the bilayer, because a dehydrated hydrogel was observed to restrict the diffusion of membrane penetrating proteins [101]. The effect

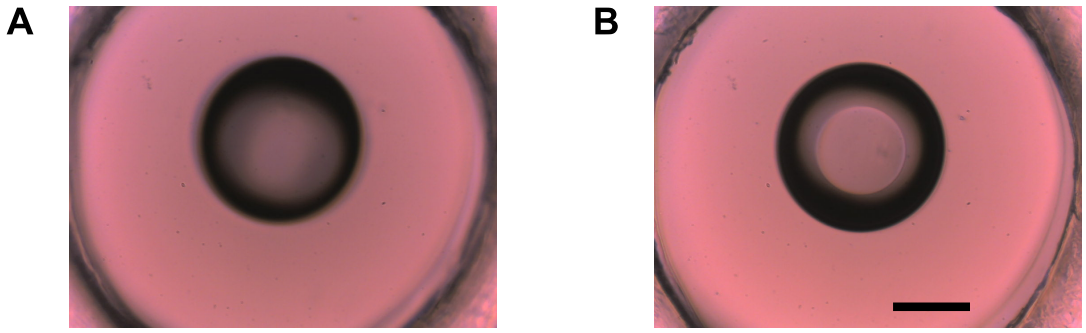


Figure 3.3: Magnified view of a droplet before and after DIB formation. *A*, A 138 nl droplet in a lipid-in-oil filled well, observed from below using an inverted objective lens. The droplet sinks under gravity to the base of the well and sits there until the monolayers fuse to form a bilayer. The barrier to immediate bilayer formation comes from excess lipids coating the hydrogel and droplet, which are displaced as the droplet sinks. *B*, The same droplet after formation of the DIB. While the droplet itself is blurred because of its three dimensional shape, the bilayer is planar and sharply in focus, appearing as a lighter circle in the centre of the droplet. The large outer circle in these images is the border of the machined PMMA well (Figure 3.2). Scale bar, 200 µm.

of a rehydrated hydrogel on the bilayer was visible: as the buffer solution spread across the base of the well, the bilayer expanded and shifted towards the aqueous front.

The DIBs on rehydrated hydrogel were ready to image via smTIRF. Imaging of the bilayers in the absence of protein was performed first, for post-processing background corrections. The subsequent injection of monomers into a droplet and smTIRF imaging is discussed in Section 3.3, but first other points are discussed that are relevant to the device and sample preparation thus far.

3.2 Tuning DIB properties to accommodate CDCs

The factors optimised for smTIRF imaging of CDC assembly included lipid composition, the choice of CDC protein used to represent CDC assembly, and the environment of the protein during imaging. These considerations are discussed in the following sections.

3.2.1 Lipid composition

Different DIB base lipids were considered for imaging CDC assembly. The lipid properties affected bilayer stability, cholesterol content, and the presence of aggregates and domains in images. The most suitable lipid was determined experimentally, with helpful insight from the literature. Continuing with the notation from Section 3.1, lipid solution A formed the hydrogel monolayer and lipid solution B formed the droplet monolayer.

A base lipid previously analysed in CDC studies is 1,2-dioleoyl-*sn*-glycero-3-phosphocholine (DOPC) [117, 118], therefore DIBs were first constructed from DOPC:cholesterol 3:2, 8.7 mg/ml total lipid concentration in hexadecane (both lipid solution A and B). Though there was some evidence of successful complex formation with the DOPC bilayer (compare Figure 3.4C-D with Figure 4.1), it was decided against for several reasons. Distinct domains were observed at high cholesterol concentrations, with apparently different cholesterol contents given the differential affinity of lPLY to the separate domains (Figure 3.4A-B). Domains were undesirable, as they would complicate the interpretation of CDC assembly data. Secondly, electrophysiology reported unusual stepwise changes in bilayer conductivity even in the absence of protein, presumably due to bilayer electroporation [119], which prevented reliable identification of lPLY by the same method on the DOPC bilayer (Section 3.4.1).

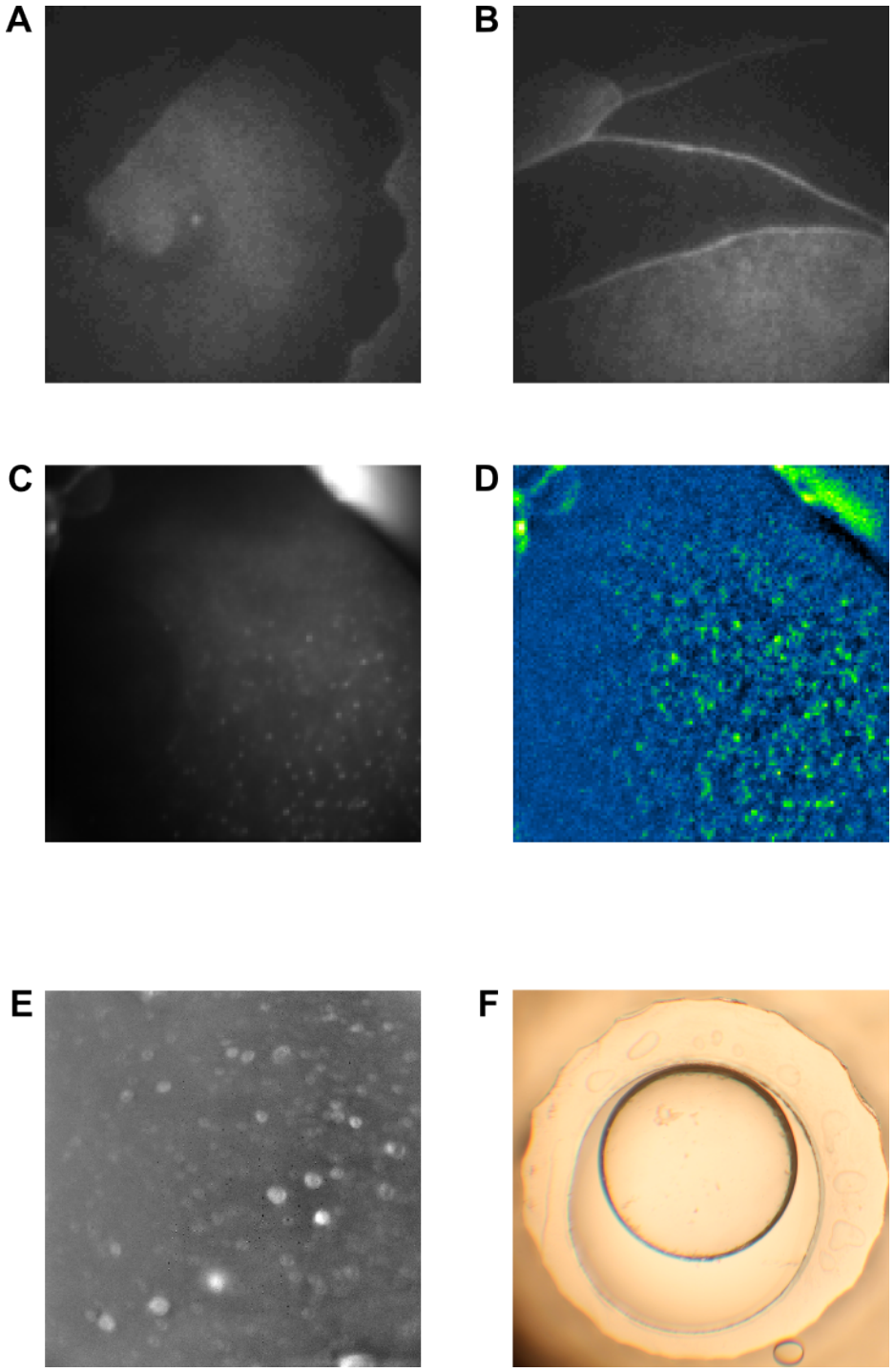


Figure 3.4: DOPC and POPC bilayers. *A*-*C*, Greyscale TIRF images of a DOPC/cholesterol bilayer displaying separate domains. Some regions are brighter indicating more lPLY monomers bound to the bilayer, and therefore a higher cholesterol content. The temperature dependence of these domains was not characterised. *C* shows some possible lPLY complexes in the DOPC bilayer, made clearer by the blue-green colourisation in *D*. *E*, TIRF image of a POPC/cholesterol/DPhPC bilayer. Lipid aggregates resulted from suspending lipids in the droplet buffer solution and forming the droplet monolayer 'inside out' by vesicle fusion. The unusual bright cloud of fluorescence near the centre-bottom is a wild-type PLY single-channel calcium fluorescent transient (SCCaFT) (Section 3.4.3). *F*, White light image of a POPC/cholesterol/DPhPC bilayer (compare with Figure 3.3). The shadowed central circle is the bilayer, with the droplet above it; the next circles are the inner and rough outer edge of the plastic wells of the device (Figure 3.2). Large lipid aggregates are visible within the droplet.

1-palmitoyl-2-oleoyl-*sn*-glycero-3-phosphocholine (POPC) was trialled based on anecdotal evidence from a collaborator that PFO had inserted into POPC droplet-droplet DIBs, and it is also a common choice for CDC studies [10, 11, 117, 118]. POPC aggregated in the oil phase but was soluble as vesicles in buffer solution, so in a variation on the protocol described above, the droplet monolayer was formed by fusion of vesicles in the aqueous droplet with the buffer-oil interface. POPC:cholesterol 1:1, 2 mg/ml total lipid concentration was dissolved in buffer solution B and sonicated in an ultrasonic bath for an hour in iced water to create vesicles; 138 nl droplets of this aqueous solution were suspended in pure hexadecane for monolayer formation. Lipid solution B was 1,2-diphytanoyl-*sn*-glycero-3-phosphocholine (DPhPC), 4.5 mg/ml.

Some success was achieved with the POPC bilayer: the single-channel recordings (SCRs) of wild-type PLY in Figure 3.11A were recorded with a POPC bilayer. However, as shown in Figure 3.4E-F, lipid aggregates were difficult to completely remove from the 'lipid-in' buffer solution. The presence of lipid aggregates would interfere with images of CDC assembly. Moreover, one of the potential mechanisms for CDC pore insertion into the POPC DIB, in this experimental configuration, was by fusion of a vesicle containing a pore with the DIB, preventing capture of the initial assembly in the limited imaging depth afforded by smTIRF.

The final base lipid tested was DPhPC, based on evidence from Nelson et al. that a low cholesterol content was required for PFO to bind to DPhPC vesicles due to reduced cholesterol shielding [117]. Cholesterol was expected to destabilise DIBs because of its poor self-assembly properties, so a low cholesterol content in DIBs was preferable. Nelson et al. found that of several reviewed base lipids, DPhPC maintained CDC binding to the membrane at the lowest cholesterol percentage in vesicles, making it a suitable choice for CDC studies with DIBs.

Furthermore, droplets with an unstable DIB lipid mixture have a tendency to burst, fusing with the supporting hydrogel and destroying the bilayer. Pure DPhPC

in hexadecane forms extremely stable DIBs because it exhibits no detectable gel to liquid crystalline phase transition between -120°C and +120°C [120]. DPhPC also forms clean DIBs without any evidence of lipid aggregates, oil inclusions or domains [99].

A DPhPC base lipid proved compatible with the biological function of CDCs, assessed by electrophysiology in Figure 3.12, and with the desired imaging conditions (smTIRF images in Chapter 4). Lipid solution A was DPhPC:cholesterol 1:2, 15 mg/ml total lipid concentration, in hexadecane; lipid solution B was DPhPC, 8.5 mg/ml in hexadecane with 10 % silicone oil. This lipid composition was used to form the DIBs in smTIRF images of CDC complexes (Chapter 4), unless otherwise stated. An asymmetric monolayer arrangement was chosen because of the destabilising effect of cholesterol: a pure DPhPC droplet monolayer encouraged stability of the droplet and prevented it fusing with the hydrogel. To compensate, lipid solution A on the hydrogel was made with a high 66 % cholesterol content to ensure a sufficient final cholesterol content for oligomerisation of the protein, and the device was heated for 30-40 minutes at 37°C prior to imaging to allow time for cholesterol to incorporate into the upper leaflet of the DIB (Section 3.1).

3.2.2 Perfringolysin O

Chapter 2 described the synthesis of an lPLY sample suitable for imaging by smTIRF. However, two different CDCs were used to study assembly, PLY and PFO. Of these, PFO behaved more consistently in its *in vitro* environment, and assembled more frequently on numerous DIBs. Therefore, in most of the smTIRF images presented in Chapter 4, particularly the assembly data, PFO was the protein under investigation and not PLY.

PFO is another archetypal CDC. It has been used, notably by the Tweten lab, in numerous investigations into CDC mechanisms and structure [8, 9, 11, 12, 26, 49]. With proven success *in vitro*, we were grateful to receive a PFO sample from our

collaborator A. P. Heuck. The gifted protein included recombinant perfringolysin O, PFO^{C459A} (rPFO) and 1:1 labelled recombinant perfringolysin O, $PFO^{C459A,E167C}$-a488 (lPFO). lPFO is equivalent to rPFO but with a mutation of the glutamic acid residue to a cysteine at position 167 to facilitate the attached fluorophore Alexa Fluor® 488 (a488), which is excited by a blue laser (a wavelength of 470, 474, or 488 nm for example). Position 167 is at the top of the monomer, relative to the membrane, and so does not influence the pore assembly mechanism [51]. The PFO mutants are examined in Figure 3.5.

Before using the gifted PFO in imaging experiments, a quick haemolysis assay was performed to check its biological activity. The results, shown in Figure 3.6, confirmed that the received PFO was active.

Reports using labelled PFO have indicated that significant self-quenching of fluorophores occurs in oligomers when the protein sample consists of 100 % labelled monomers [121]. Quenching is the non-radiative de-excitation of fluorophores caused by an external environmental influence [70], it was undesirable in this study due to misleading estimates of stoichiometry. Self-quenching is equivalent to general quenching but is caused by proximal molecules of the same kind [70], such as identical fluorophores on labelled CDC monomers. Johnson et al. reported experiments where self-quenching was used to detect oligomerisation [121].

To combat self-quenching in the present study, a controlled ratio of labelled to unlabelled monomers was added to bilayers to increase the average distance between fluorophores in oligomers. Previous experiments suggested that quenching was significantly reduced for a labelled:unlabelled ratio of around 10 % [121], so lPFO:rPFO 1:10 was initially added to DIBs for smTIRF experiments.

The 1:10 labelled:unlabelled protein ratio was adjusted iteratively in several consecutive droplets to maximise the SNR of the single labelled monomers and complexes in smTIRF imaging. By trial and error, the ratio of labelled:unlabelled lPFO:rPFO with the highest SNR for complexes and labelled monomers was found

A

MRGSHHHHHHGMASMTGGQQMGRDLYDDDDKDPSSRS
KDITDKNQSIDSGISSLSYNRNEVLASNGDKIESFVPKEG
KKAGNKFIVVERQKRSLTTSPVDISIIDSVNDRTYPGALQ
LADKAFVENRPTILMVKRKPININIDLPGLKGENSIKVDDP
TYGKVSGAIDELVSKWNCKYSSTHTLPARTQYSESMVYS
KSQISSALNVNAKVLENSLGVDFNAVANNEKKVMILAYK
QIFYTVSADLPKNPSDLFDDSVTFNDLKQKGVSNEAPPL
MVSNVAYGRTIYVKLETTSSSKDVQAAFKALIKNTDIKNS
QQYKDIYENSSFTAVVLGGDAQEHNKVVTKDFDEIRKVIK
DNATFSTKNPAYPISYTSVFLKDNSVAAVHNKTDYIETTS
TEYSKGKINLDHSGAYVAQFEVAWDEVSYDKEGNEVLTH
KTWDGNYQDKTAHYSTVIPLEANARNIRIKAREATGLAWE
WWRDVISEYDVPLTNNINVSIWGTTLYPGSSITYN

B

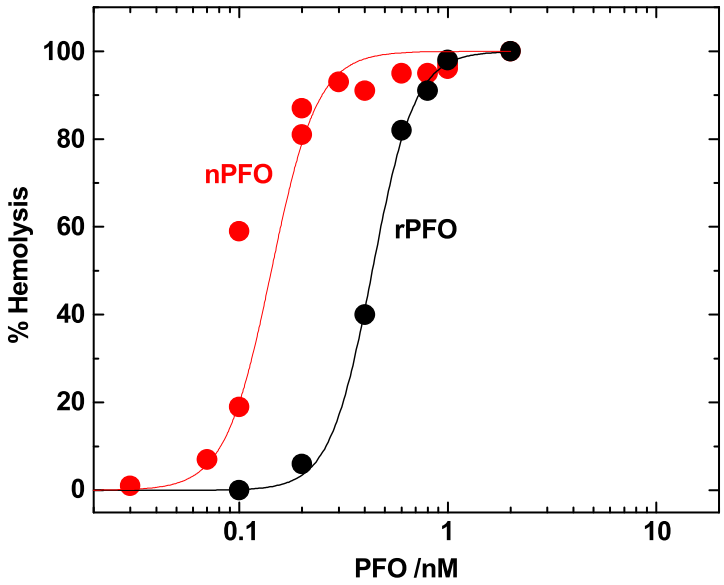


Figure 3.5: PFO characterisation. *A*, Amino acid sequence of lPFO. Red (in order): the hexahistidine tag, an enterokinase cleavage site, the cysteine residue mutation at position 167 for labelling with a488, the alanine residue that replaced the native cysteine at position 459. *B*, A comparison of the haemolytic activity of rPFO with nPFO (wild-type PFO with prepended hexahistidine tag; rPFO = $nPFO^{C459A}$). 100 % haemolysis was defined by osmotic shock in deionised water, 0 % by the absence of protein. Haemolysis was measured by the extent of haemoglobin release, by absorbance of the supernatants of centrifuged red blood cells at 540 nm. rPFO was approximately 3 times less active than nPFO, measured at 50 % lysis. Data courtesy of A. P. Heuck [121].

to be around 1:5.5.

The protein concentration was also adjusted over several bilayers, to optimise the time over which assembly occurred, and ultimately a value of 37 nM total protein concentration in the droplet was chosen. It was essential to optimise the timing of

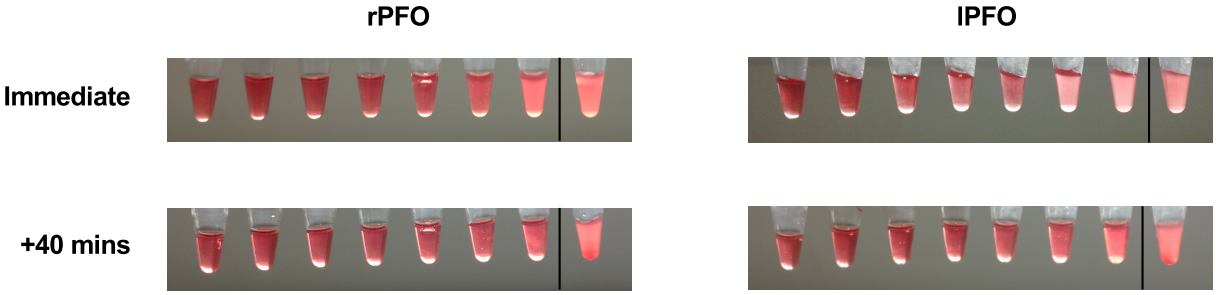


Figure 3.6: Haemolysis assay with received PFO sample. A quick assay for PFO activity, using haemolysis as described in Section 2.5.1. Rather than using a 96-well plate and plate-reader, as in Figure 2.7, the red blood cells and the protein were added to PCR tubes. Left to right, final protein concentration decreasing by a factor of 2 from 250 nM; last tube on the right contained no protein. Lysed cells became translucent (tubes towards the left), intact cells remained cloudy and opaque (tubes toward the right). The photographs taken immediately show that lysis occurred instantly for high protein concentrations. After 40 minutes the red smudge indicated that some cells had settled at the bottom of the buffer-only tube, while all of the tubes with protein exhibited some lysis.

assembly for reasons discussed in Section 4.2.2, but the protein concentration was difficult to control, as discussed in Section 3.2.4. A new protein aliquot was thawed every 2 weeks and centrifuged for 20 minutes at 14,000 rpm, 4°C, to ensure the imaged protein was not degraded or aggregated.

3.2.3 Applying protein to the bilayer

An important condition for capturing assembly of CDC complexes was the prevention of any interaction between the protein sample and cholesterol prior to imaging. The protein sample was not included in buffer solution B, where it could interact with cholesterol as the droplet monolayer formed, but injected into droplets after bilayer formation using a nanolitre microprocessor-controlled injector (Nanolitre 2010, WPI). The same injector was previously used to create uniform droplets and to rehydrate the hydrogel in Section 3.1; the method for injecting protein solution into the droplet is described in Section 3.3.

The volume of protein solution injected into the droplet was 2.3 nl (compared to the 138 nl droplet). 2.3 nl was the smallest injectable volume permitted by the injector. The volume injected was kept small to avoid disturbing the 138 nl droplet: a sudden expansion of the droplet volume destabilised the DIB.



Figure 3.7: Nanolitre injector. The injector was used to make uniform 138 nl droplets, to rehydrate the hydrogel substrate prior to imaging and to inject protein solution into the droplets. It comprises an arm that could be attached to a micro-manipulator (Figure 3.8), a glass capillary with a pulled tip (10 - 20 μm diameter), and a microprocessor-controlled metal plunger that was used to fill and expel solution from the tip. The capillary was back-filled with mineral oil to facilitate sample loading by displacement of the plunger.

The small volume of injected protein solution necessitated a high protein concentration to ensure oligomerisation (2.2 μM in the injected volume for 37 nM in the droplet). The small injected volume caused a significant error on the concentration of protein inside the droplet, compounded by the relatively high protein concentration in the injected volume (Section 4.3.1). A photograph of the injector that was used to inject protein solution into the droplets is shown in Figure 3.7.

3.2.4 Droplet solution conditions

The buffer solutions A and B (defined in Section 3.1) were chosen to encourage protein activity in the DIB and to support smTIRF imaging. Other than the oSCR experiments discussed in Section 3.4.3, buffer solutions A and B were equivalent. For CDC assembly experiments, the buffer solution was 0.5 M KCl, 10 mM MES, 0.1 mM EDTA, 1 mM Trolox, 10 mM Cysteamine, at pH 6.3.

0.5 M KCl was a compromise between droplet stability provided by high salt concentration and more physiological salt concentrations closer to 150 mM. Low pH

was found to increase PFO binding and rate of pore formation at low cholesterol concentrations by Nelson et al., an explanation being that some CDCs operate in acidic phagosomes [117]. The combination of Cysteamine and Trolox was reported by Campos et al. to reduce photobleaching of fluorophores [122], so it was included in buffer solution although its efficacy was not characterised (photobleaching is discussed in Section 4.4).

3.3 Imaging protocol

In Section 3.1, the preparation of DIBs ready for imaging CDC assembly was discussed, finishing with rehydration of the hydrogel substrate and the imaging of bilayers by TIRF, without protein, for background correction. The lipid compositions, protein sample, injection method and buffer solutions chosen for capturing CDC assembly were then detailed. This section describes the protocol for recording videos of assembly by smTIRF imaging, continuing from the background correction recordings.

Injection of the 2.3 nl volume containing the protein sample was achieved by submerging the tip of the glass capillary of the injector under the surface of the oil solution. The 2.3 nl volume was then expelled from the tip, but did not mix with the oil phase. The 2.3 nl volume was lowered into contact with the 138 nl droplet until the two fused. The bilayer was not disturbed by the injection, helped by the fact that a DIB can easily be translated laterally around the base of the well.

The physical arrangement for the injection is illustrated in Figure 3.8A. The position of the injector was controlled by a micro-manipulator; the same was used to hold an electrode that was inserted into droplets for electrophysiology in alternative experiments (Section 3.4.1). The position of the injector tip was monitored from above and via an inverted 20× objective lens from below. Figure 3.8B highlights the arrangement within a well, along with other features of the imaging protocol:

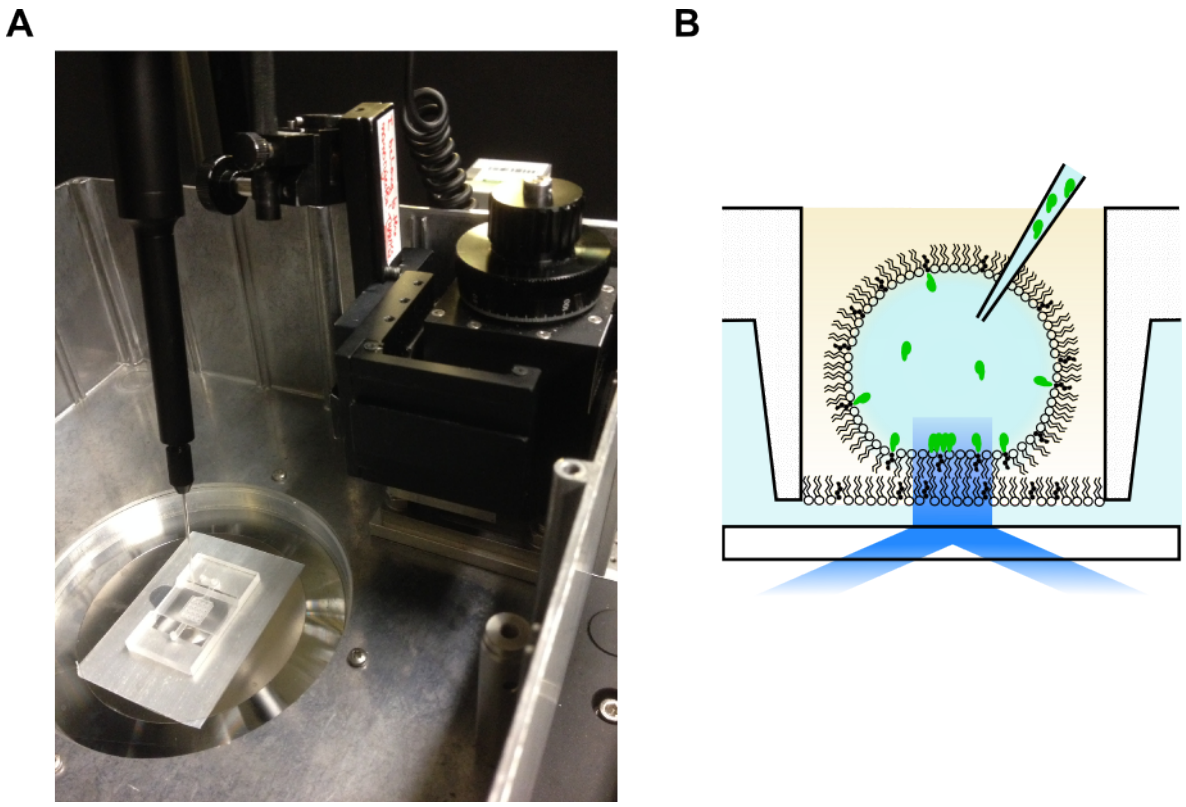


Figure 3.8: Experimental design for imaging CDC assembly. *A*, A microprocessor-controlled nanolitre injector secured to a micro-manipulator was used to inject PFO into a droplet with a preformed DIB in one of the 16 wells of the bespoke plastic device. The bilayer was then imaged in TIRF mode: the inverted TIRF objective lens is identifiable just beneath the device. The device was electrically isolated from the stage by a sheet of parafilm with a hole for the lens to pass through. The device is enclosed in a Faraday cage to reduce electrical noise during electrophysiology recordings, and to host the micro-manipulator. *B*, A schematic representation of capturing assembly. One well is shown, the sides of the well and the coverslip are represented; the lipid-in-oil solution in the well is coloured brown. PFO (green) was injected into the droplet and bound to cholesterol (black) in the bilayer. Fluorophores on the lPFO were excited in TIRF mode with a 470 nm laser.

injection of the labelled protein; excitation of the a488 fluorophores with a blue 470 nm laser in TIRF mode; cholesterol incorporated in the monolayers and bilayer; the edges of the plastic well and the hydrogel substrate above the coverslip. For simplicity, Figure 3.8B shows injection by piercing the droplet.

SmTIRF imaging of the bilayer was initiated as soon as possible after injection of protein into the droplet, typically within 30 seconds, to ensure that assembly was captured and did not reach conclusion prior to imaging. The 20× objective lens was switched to a high, 1.49 numerical aperture 60× Nikon TIRF objective lens, to which immerision oil had been added previously, and the level of focus was found using the

bilayer edge. Videos of the bilayer were recorded on an Andor iXonEM+ electron multiplying charge-coupled device (EMCCD) camera, 128 × 128 pixels, using the Andor Solis software package. (The exposure time of 60 ms was long enough not to be limited by this chip size.)

The imaging conditions for assembly videos, exemplified in Figure 4.2, were as follows. Exposure time was 60 ms per frame, the laser power incident at the back aperture of the objective lens was 0.06 mW. The laser was partially shuttered in the optical path before the objective lens to prevent photobleaching fluorophores outside the field of view; with an open shutter the incident power at the back aperture was 0.25 mW. The electron multiplying gain on the EMCCD detector was at its maximum of ×300 to achieve high sensitivity with the camera. A 470 nm laser was used to image a488-labelled lPFO, a 532 nm laser to image Cy3B-labelled lPLY.

The laser power and exposure settings were a compromise to ensure that minimal photobleaching occurred (low laser power), that the relevant timescale for assembly at the single-complex level could be captured (short exposure time/high frame-rate), but that sufficient photons reached the camera to be able to observe complexes with a high SNR, and to observe single molecules simultaneously with complexes too if possible (high laser power and long exposure time). Photobleaching is described in Section 4.4. Any deviations from these exposure settings, such as the higher laser power used for photobleaching in Section 4.4.2, are noted.

3.4 Validating CDC function in DIBs

Sections 3.1 and 3.3 describe the protocol for imaging assembly of PFO complexes, in line with the goal of the project. To give confidence that the complexes identified by smTIRF were biologically relevant CDC oligomers and pores, the functionality of the pores was measured by electrophysiology.

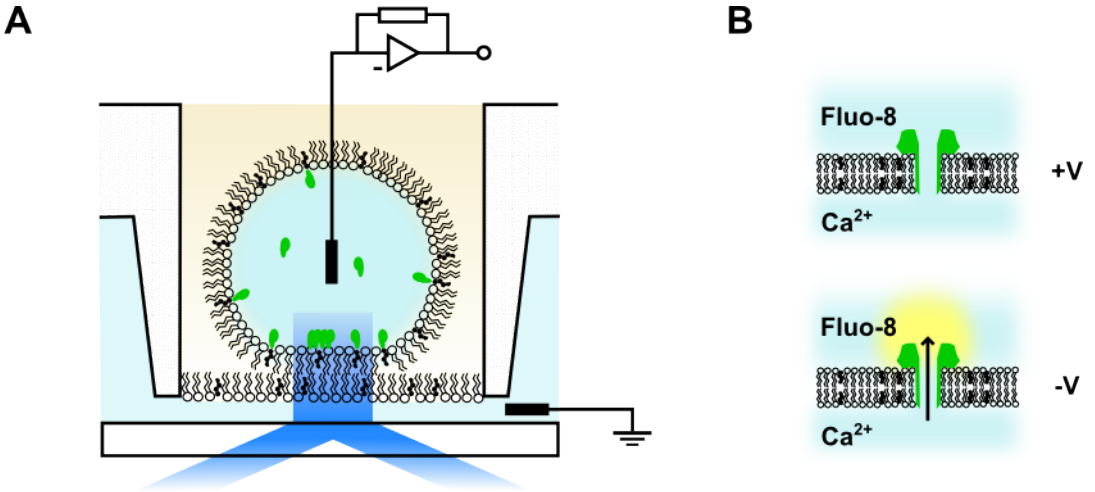


Figure 3.9: Electrophysiology with a DIB. *A*, To record the ionic current across a DIB, a ground electrode was placed in the agarose, in electrical contact with the hydrogel substrate supporting the bilayer. A reference electrode was used to pierce the droplet. The two electrodes were connected to an amplifier. The DIB effectively acted as a capacitor between the electrodes. This arrangement was used to detect CDC pores inserting into the DIB. *B*, The mechanism of an oSCR, in this case a SCCaFT (Section 3.4.3). A hole in a bilayer breaks the barrier between a fluorogenic dye (Fluo-8) and its binding partner (Ca^{2+}). Upon binding, the dye becomes fluorescent under excitation. Fluo-8 is excitable using a 474 nm laser in TIRF mode, as illustrated in *A*. The passage of the binding partner through the hole can be manipulated by applying a potential. For SCCaFTs, brighter fluorescence is seen under negative applied potential. The bilayer must naturally be highly impermeable to both binding partner and dye.

Electrodes were placed on either side of a DIB as described in Section 3.4.1. Protein channel insertion events caused stepwise changes in the conductivity of the bilayer. Insertion events were distinguishable from other lesions such as tears or electroporation [119] by their rectilinear shape; the alternative lesions induced a trans-bilayer ionic current that fluctuated.

3.4.1 Electrophysiology protocol

This section describes modifications to the DIB construction protocol outlined above, to facilitate recording of the ionic current across a DIB. Immediately after pipetting the 1.8 % molten agarose solution through the device, and while the agarose was still molten, a 1.5 mm electrode was placed into the symmetric hole of the two 2 mm holes on one side of the device (Figure 3.2); excess displaced

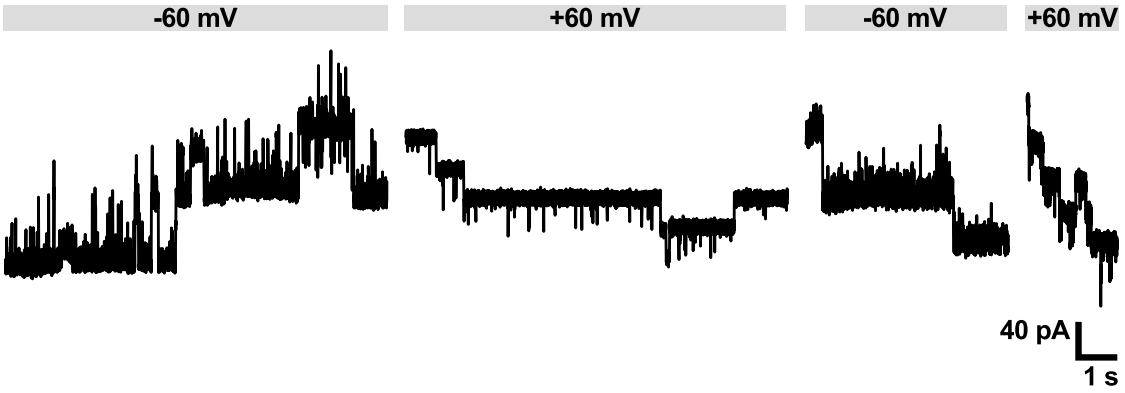


Figure 3.10: αHL insertion events. Step-changes in the conductivity of a DPhPC DIB after addition of αHL hepatamers, recorded by the method illustrated in Figure 3.9. Pore conductances were typically 0.7-1 nS, but these values were dependent on the hydration of the hydrogel substrate.

agarose flowed out from the other, asymmetric 2 mm hole. The 2 mm holes were sealed with tape and vacuum grease to prevent dehydration of the hydrogel. As depicted in Figure 3.9A, the 1.5 mm electrode inserted into agarose in the 2 mm hole was the ground electrode for recordings of ionic current.

The protocol for DIB construction proceeded as described above for imaging experiments, after inserting the ground electrode, until protein was injected into the droplet. After each injection, the injector was removed from the micro-manipulator and replaced with a 0.1 mm electrode, the reference electrode depicted in Figure 3.9A, which had been dipped into a shallow droplet of molten agarose, 0.75 % in MQ. The ground electrode and reference electrode were inserted into a CV-203BU headstage connected to an Axopatch 200B amplifier, both from Axon Instruments. The droplets and electrodes were contained in a Faraday cage to reduce electrical noise, which can be seen in Figure 3.8.

The reference electrode was lowered via the micro-manipulator, viewed from above and with an inverted 20× objective lens from below, and pierced the droplet containing the injected protein. The hydrophilic agarose coating of the electrode tip facilitated piercing of the droplet. The ionic current across the bilayer between the ground and reference electrodes was recorded using WinEDR software from the University of Strathclyde (Strathclyde Electrophysiology Software package).

3.4.2 Single-channel recordings of pore-forming toxins

Before testing the functionality of PLY or PFO complexes on the DIB, αHL heptamers were added to droplets to test the electrophysiology apparatus. αHL heptamers bound the lipid phosphocholine heads abundantly; many insertion events were observed following αHL injection (Figure 3.10). In the ionic current traces in this section, a positive step in current under positive applied potential indicates a protein insertion event, a negative step in current under positive applied potential indicates a 'de-insertion' or channel-blockage event, and the opposite applies to negative applied potential.

Figure 3.11 shows single-channel recordings (SCRs) of PLY added to DIBs of various lipid compositions. Figure 3.11A presents several different types of putative insertions of wild-type PLY into a POPC/cholesterol/DPhPC DIB (Section 3.2.1): some small, ill-defined short-lived steps that generally occurred earlier in the recording, some larger square steps that occurred after tens of minutes. These features match the behaviour expected from the insertion of arc pores and large complete pores respectively. The measured conductances of 0.1-1 nS agree with previous reports for PLY (Figure 1.8) [56].

Some insertion events lasted for a matter of seconds before the conductivity reverted to its previous level (Figure 3.11A). This behaviour was attributed to blockage of the pores, possibly by agarose from the hydrogel, or by lipid aggregates for the POPC bilayer (Figure 3.4E). For low-conductance insertion events, putatively caused by arc pores, another explanation could be collapse of the β-barrel structure. Similar events have been observed previously (Figure 1.8 [56]).

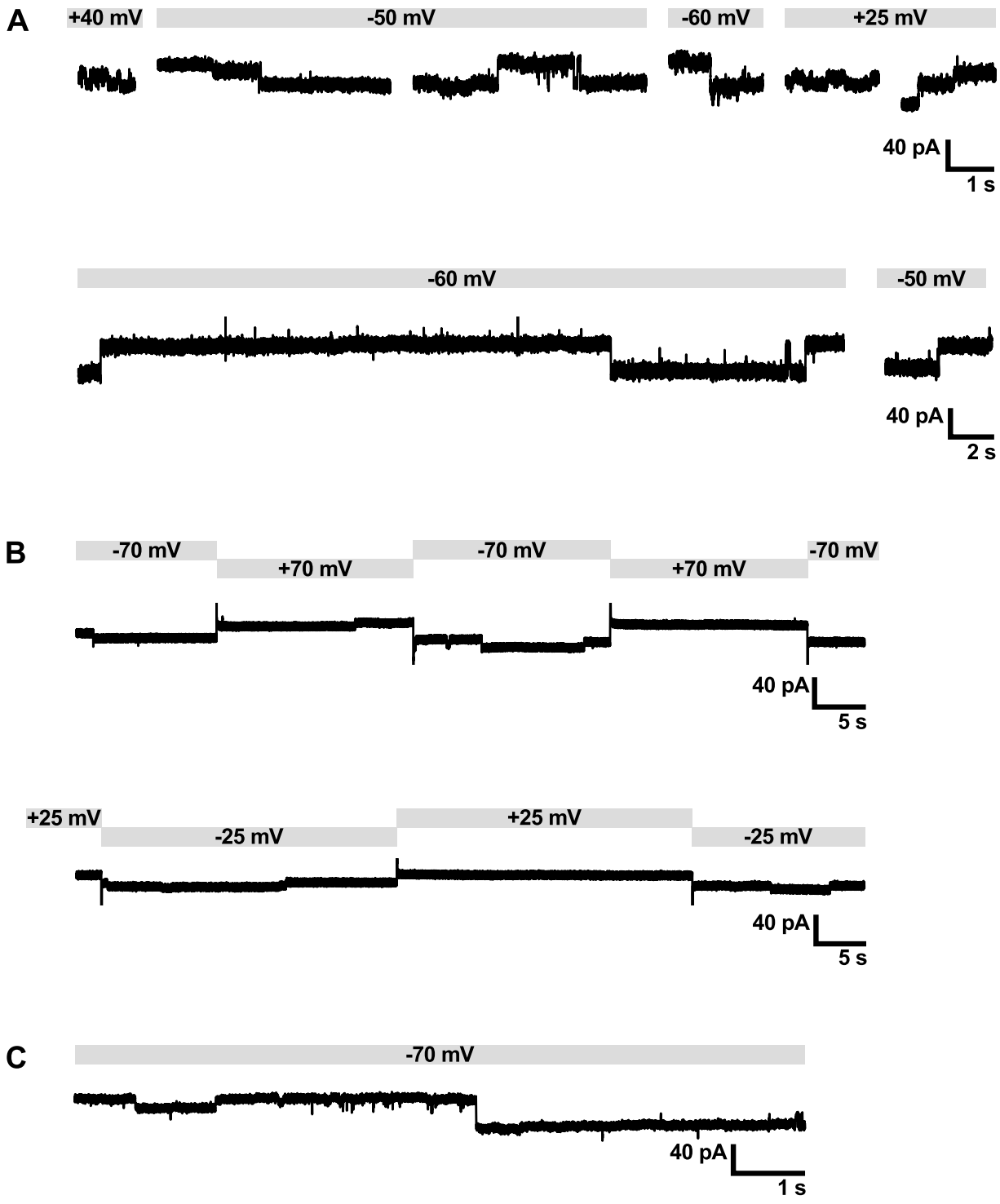


Figure 3.11: PLY insertion events. *A*, Step-changes in the conductivity of a POPC/cholesterol/DPhPC DIB after addition of wild-type PLY. A range of pore conductances was observed, from 0.1 to 1 nS, but these values were dependent on the hydration of the hydrogel substrate. *B*, SCRs of a DOPC/cholesterol bilayer after addition of lPLY. These stepwise changes were related to the activity of lPLY, as many more were observed in bilayers with lPLY. However, stepwise changes were observed in DOPC/cholesterol bilayers in the absence of protein, shown in *C*, presumably caused by electroporation [119]; DOPC was decided against as the base lipid for further experiments.

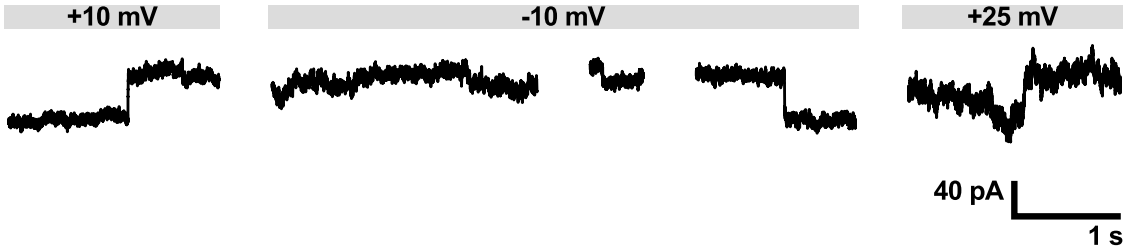


Figure 3.12: PFO insertion events. Step-changes in the conductivity of a DPhPC/cholesterol DIB after addition of rPFO. A range of pore conductances were observed, from 1 to 4 nS. 4 nS is in agreement with the expected value for a complete PFO pore [9].

The rectilinear changes to ionic current in Figure 3.11 supported proteinaceous pores as the source. The next most likely source of ionic current variation was electroporation [119]. Electroporation events were typically observed at applied potentials of around 200 mV, higher than the potentials in Figure 3.11, and were distinguishable from proteinaceous pores by their fluctuating conductivity. For the DOPC/cholesterol bilayer, some step-like events, presumably caused by electroporation, were observed in the absence of protein at 70 mV applied potential (Figure 3.11C); DOPC was therefore avoided as the base lipid in further experiments.

Figure 3.12 shows the ionic current across a DPhPC/cholesterol bilayer after the addition of rPFO. Small fluctuant step-changes in conductivity were observed, and after tens of minutes, large rectilinear step-changes. The largest step-changes for rPFO were around 4 nS, in agreement with previous PFO SCRs [9]. These experiments were challenging, because at low protein concentration no changes to conductivity were observed, but at high concentration bilayers ruptured suddenly, before any insertion events were observed or even before the electrode was inserted into the droplet, consistent with a cooperative nature of assembly.

The step-changes in conductivity after addition of PLY or PFO confirmed that the proteins were capable of inserting into DIBs, and therefore that assembly had occurred and could be captured by imaging. Relatively few insertion events were observed overall, a matter discussed in Section 4.2.3. In some of the electrophysiology experiments presented here, the recordings of ionic current were complemented by optical single-channel recordings (oSCRs); these results are

discussed in Section 3.4.3.

3.4.3 Optical single-channel recording

oSCRs link the spatial organisation and diffusion of pores with the passage of ions through them [102, 103]. Importantly, when several pores are present in a bilayer, electrical measurements only report the sum of the ionic current across a bilayer, but oSCRs can decompose this total current into its constituent parts by spatially resolving the pores (see Figure 3.13A, for example). The principle of oSCR is detailed in Figure 3.9B. The oSCRs referred to herein were all single-channel calcium fluorescent transients (SCCaFTs): the fluorogenic dye was Fluo-8 and the binding partner causing Fluo-8 to fluoresce was Ca^{2+}; these were included in buffer solutions B and A respectively.

Complete αHL and PLY pores inserting into DIBs induced stable SCCaFTs with conductivity independent of applied potential. At high (200 mV) applied potential, electropores were sometimes observed as voltage-dependent SCCaFTs, with irregular sizes and fluctuating intensities. oSCRs therefore complemented the identification and discrimination of proteinaceous pores by electrical SCRs described in Section 3.4.2.

The cloud of fluorescence corresponding to a SCCaFT was imaged by TIRF. The rate of Ca^{2+} passing through pores could be increased or decreased, leading to a brighter or dimmer cloud of fluorescence, by applying a potential across the bilayer (Figure 3.9B). A square-wave voltage caused the SCCaFT to flash on and off, making it extremely easy to identify.

As with electrical recording alone, the technique was first verified using αHL heptamers applied to a DIB, because of their reliability and their proclivity for insertion into simple phosphocholine lipid bilayers. Figure 3.13A shows a high density of αHL heptamer-induced SCCaFTs on a DIB.

Figure 3.13B illustrates a SCCaFT induced by wild-type PLY on a

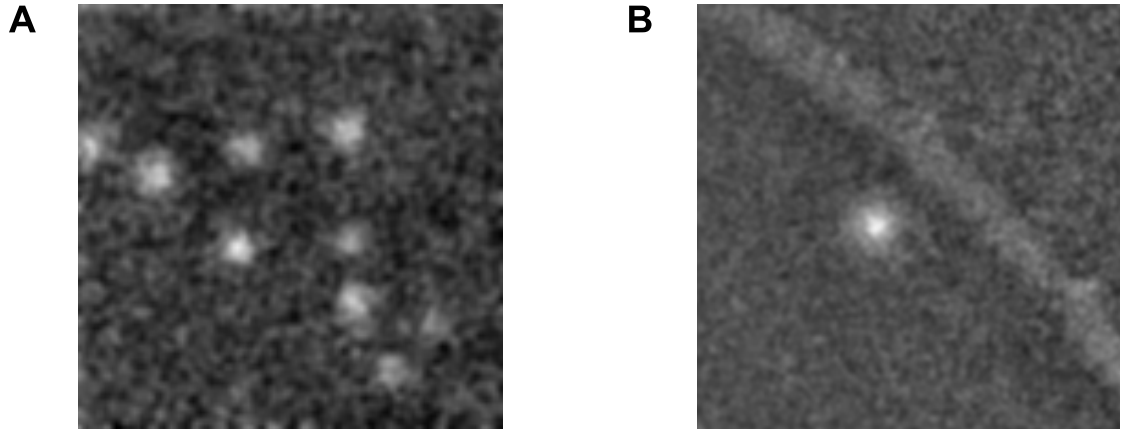


Figure 3.13: Optical single-channel recording of αHL and PLY pores. TIRF image of SCCaFTs caused by the insertion of protein pores into a DIB. *A*, αHL pores in a DPhPC bilayer. *B*, Wild-type PLY pores in a POPC/cholesterol/DPhPC bilayer. The edge of the DIB is also present in the image. The oSCR mechanism is illustrated in Figure 3.9B.

POPC/cholesterol/DPhPC DIB. PLY-induced SCCaFTs were constant, stable and diffusing, confirming their identity as PLY pores rather than electropores. The SCCaFT in Figure 3.13B was recorded on the same bilayer as the electrical traces in Figure 3.11A.

The electrical and optical data from a wild-type PLY-induced SCCaFT is decomposed in Figure 3.14. Unfortunately, the insertion event itself was not captured optically. The potential applied across the bilayer alternated between +60 mV and -60 mV, with a short period of 0 mV in between (Figure 3.14A). The direction of the ionic current across the bilayer changed in line with the applied potential (Figure 3.14B). Moreover, the intensity of a region of interest drawn around the SCCaFT also oscillated in line with the potential (Figure 3.14C). Some frames from TIRF imaging of the SCCaFT are shown in Figure 3.14D.

oSCRs were employed in this section to confirm the identity of lPLY pores. Recent experiments in our lab have yielded similar results for PFO (Figure 4.10). The oSCRs spatially resolved the ionic current through multiple pores; this feature was exploited especially at potentials that caused electropore events, to decompose the sum ionic current detected electrically into the proteinaceous pore and electropore components.

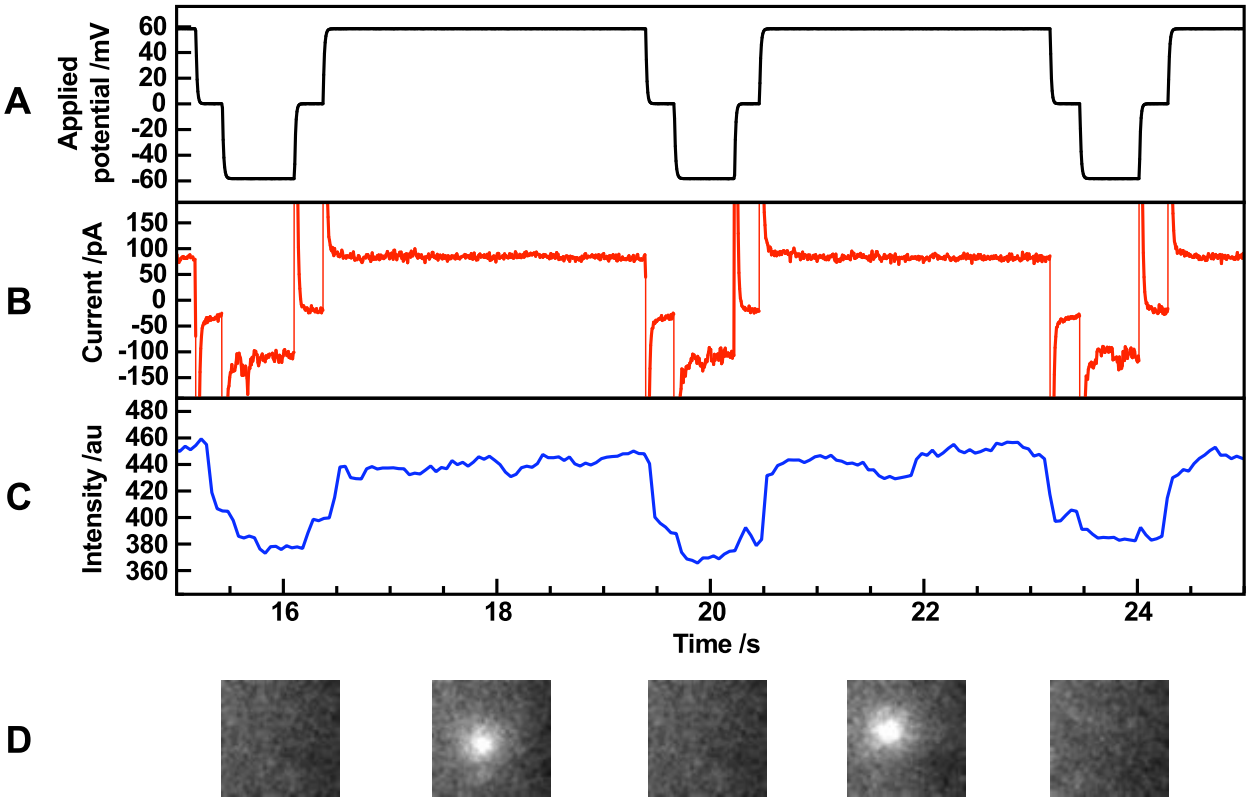


Figure 3.14: Deconstructing SCCaFT data from a PLY pore. A potential, *A*, applied across a POPC/cholesterol/DPhPC DIB influences the passage of Ca^{2+} ions through a wild-type PLY pore. The electrical recording, *B*, only reports total ionic current across the bilayer. The contributions to total current from individual pores can be resolved spatially using oSCR. The intensity of a region of interest around the SCCaFT, *C*, changes according to the applied potential. The SCCaFT flashes on and off, as demonstrated by TIRF images of the wild-type PLY-induced SCCaFT, *D*.

3.5 Summary

The insertions of CDC pores presented in the previous section validated the DIB construction and imaging protocols devised earlier in the chapter. The DIB construction method has been described previously [99], but was adapted here to accommodate CDCs and the imaging of assembly. For example, the lipid composition and droplet conditions were chosen to support stable DIBs and CDC activity, and the protein was injected rather than incorporated into the droplet initially to avoid interaction with cholesterol and initiation of assembly prior to imaging. The reason for undertaking the protocol optimisation and verification of CDC function in the *in vitro* DIB system, namely imaging of CDC monomers and oligomers by smTIRF, is described in Chapter 4.

Chapter 4

Recording cholesterol-dependent cytolysin assembly in real time with millisecond temporal resolution

This chapter focuses on data collection and a qualitative description of the results from smTIRF imaging of CDCs. Complexes were first imaged after assembly had reached completion, to remove the strict time constraints imposed by the assembly process. Assembly was subsequently recorded at different concentrations, for both PLY and PFO. The stoichiometry of some CDC complexes was estimated by photobleaching. A quantitative analysis of the smTIRF assembly data is presented in Chapter 5.

4.1 Protein complex detection by smTIRF

Confirmation that CDC assembly could be imaged was provided by smTIRF imaging of monomers and oligomers at equilibrium (after completion of assembly) on a DIB.

The recordings present the first video frame-rate dynamic picture of CDCs at single-molecule resolution. Representative frames from the videos are presented in Figure 4.1.

The light from a single fluorophore in the illuminated volume in a smTIRF experiment was collected by the EMCCD and formed a single spot in the image, with heightened intensity relative to the background signal. Each bright spot in the images of CDC complexes therefore represents one or more fluorophore-labelled monomers. The spot created by a fluorophore in the image was a convolution of the fluorescence light and the changes imposed on the signal by passing through the imaging apparatus (the point spread function (psf) of the apparatus; the psf of an imaging system is equivalent to the blurred spot in the image created by a point source of light [123]).

Complexes containing multiple colocalised labelled monomers such as oligomers and pores exhibited significantly higher intensity than that of a single fluorophore, because the light detected from the individual fluorophores was summed at the detector. The videos revealed a large number of dim spots (the monomers, with one fluorophore) and a small population of brighter spots with a range of intensities (the complexes, with several fluorophores). Figure 4.1 illustrates these features for lPLY and lPFO, at equilibrium. The number of photons per fluorophore was not measured.

The spots representing the monomers and complexes had a typical diameter of 550 nm ($2\bar{\sigma}$ of a fitted Gaussian function, as described in Section 5.5.2), an order of magnitude larger than the 40 nm-diameter of CDC pores. Therefore, a small non-biologically relevant protein aggregate and a biologically relevant arc, prepore or pore could not be discriminated by the detection of a spot alone.

However, several indirect pieces of evidence suggest that the bright spots in Figure 4.1 represent biologically relevant CDC complexes: firstly, the complexes did not continue to aggregate but reached a stable size that was smaller than 550

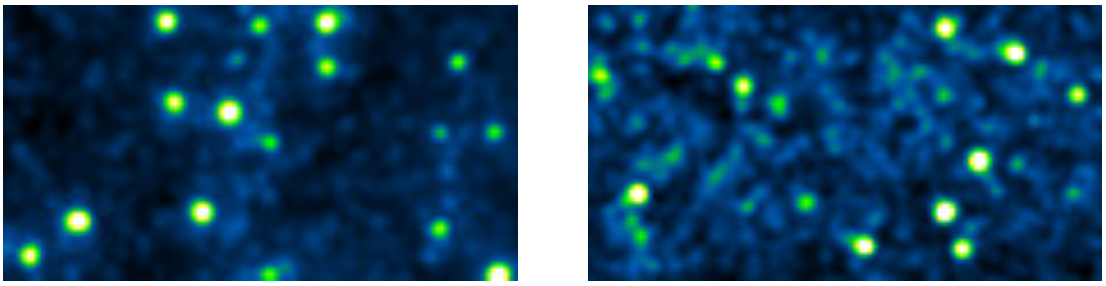


Figure 4.1: Individual CDC complexes on a DIB, detected by smTIRF. *Left*, lPLY monomers and complexes. *Right*, lPFO monomers and complexes (lPFO:rPFO 1:5.5). Single labelled monomers are represented by dim light-blue spots, protein complexes contain multiple fluorophores and so appear as much brighter spots. The frames are colourised to highlight the complexes in yellow-green; at this contrast setting the monomers are difficult to resolve. The images have been filtered with a Gaussian function, $\sigma = 1$ pixel. Fields of view are 45 μm × 24 μm.

nm across (because they had no discernible structure at the resolvable 550 nm scale, Figures 4.1 and 4.2). The proteins were able to form functional complexes as evidenced by SCRs in Section 3.4.2. The complexes assembled while diffusing in two dimensions on the bilayer (Figure 4.2) (with diffusion coefficients consistent for diffusing proteins [124, 125], Section 5.4.2); they did not aggregate in solution and subsequently bind to the bilayer. The diffusivity of the brighter, larger complexes was lower than for the small complexes and single molecules (see Section 5.4.2).

Finally, the stoichiometry of the complexes after calibration with intensity matched the expected stoichiometry for CDC complexes (see Sections 4.4.2 and 5.3). There is therefore good reason to believe that the observed spots in the smTIRF images in Figure 4.1, and in other figures in this chapter, correspond to single labelled monomers and biologically relevant protein complexes. This assumption is maintained for all subsequent results and analysis.

4.2 Capturing the assembly process

4.2.1 Typical features of PFO assembly

The observation of monomers and oligomers at equilibrium on a DIB, presented in Figure 4.1, made capturing assembly a matter of fine-tuning the amount of protein

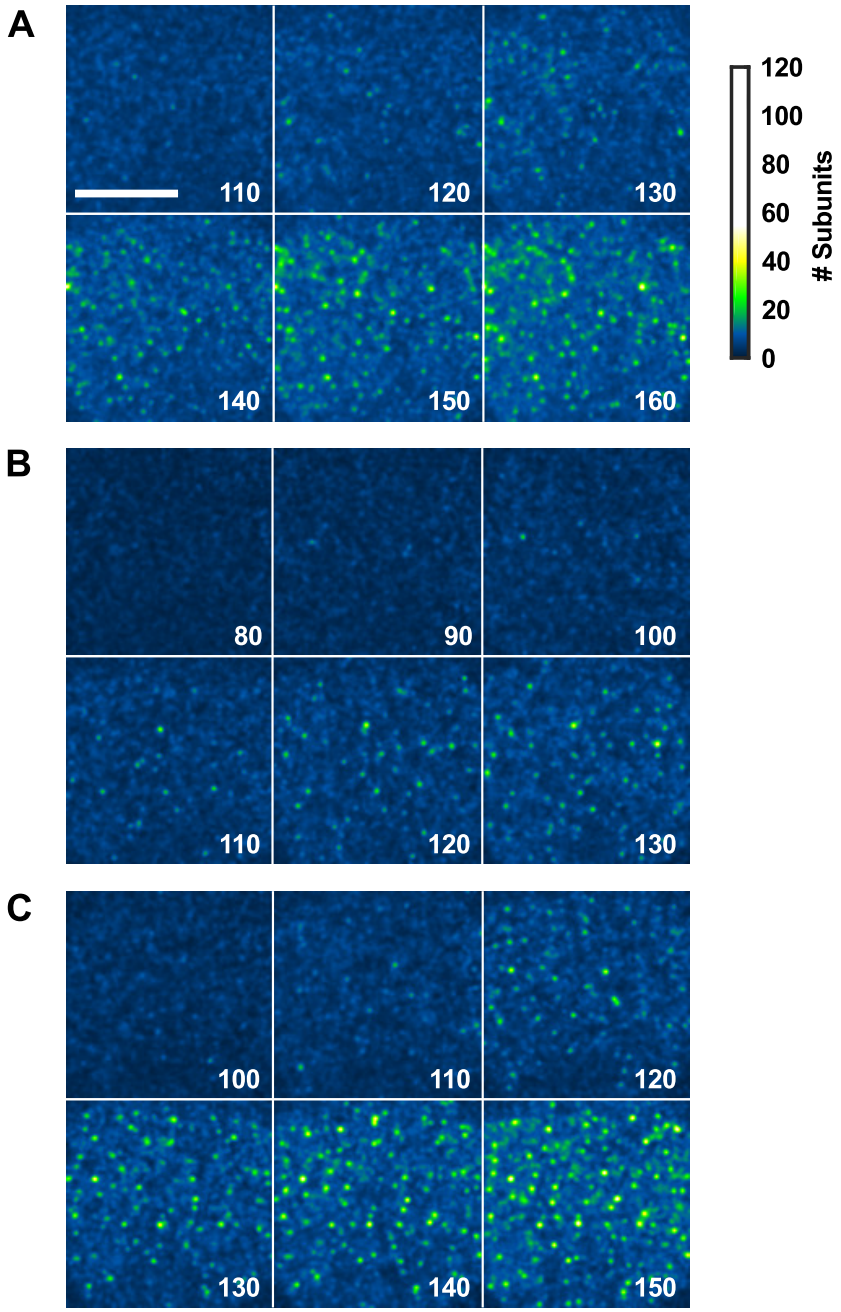


Figure 4.2: Typical smTIRF recordings of PFO assembly. A 2.3 nl volume of lPFO:rPFO 1:5.5 was injected into a 138 nl droplet with a pre-formed DIB. The total protein concentration in the droplet was nominally 37 nM. *A*-*C* are equivalent iterations of protein injection and imaging assembly, the only differences being variations in protein concentration due to error (Section 3.2.3). The brighter spots are complexes that contain multiple fluorophores; the dim light-blue spots are single labelled monomers. Intensity was calibrated to number of subunits as per the colour bar (see Section 5.3), but the scale must be interpreted carefully because one fluorophore corresponds to 6.5 monomers due to the presence of rPFO. Numbers on the frames indicate time in seconds following injection of the protein. The images have been filtered with a Gaussian function, $\sigma = 1$ pixel. Scale bar 25 μm.

injected into the bilayer and perfecting the timing of the recording (see Section 4.2.2). As described in Section 3.2.3, to avoid interaction between CDCs and cholesterol prior to imaging, the protein was injected into a droplet with a pre-formed DIB (the lipid composition and droplet solution conditions of the DIB are described in Section 3.2). Imaging was initiated as soon as possible but no more than 30 s after injection. Figure 4.2 demonstrates that lPFO generally began to assemble within tens of seconds following injection; the complexes are represented by bright yellow-green spots, the monomers by dim light-blue spots.

The arbitrary intensity units in Figure 4.2 were calibrated to stoichiometry (Section 5.3). Though infrequent, the intensity of some of the spots towards the end of assembly corresponded to over 100 subunits; these were attributed to the large multiple-arc/ring shaped complexes seen via EM and AFM (see Figures 1.6 and 1.9), though they could also be caused in some cases by proximal non-interacting complexes. Most of the bright complexes late in the assembly videos contained around 30-40 subunits (Figure 5.15), as expected for PFO complexes [21, 22, 39–42].

Complexes were distinguishable from monomers and above the background signal once they contained 2-3 labelled monomers. At low stoichiometries they were observed diffusing laterally on the bilayer (Figure 5.1 and Section 5.4.2). Over time, the intensity of the complexes increased stochastically, but generally monotonically. The inferred mechanism of assembly is discussed in Chapter 5.

Eventually the complexes reached a stable size and many appeared to become immobile. Overall, diffusivity appeared to decrease for larger complexes (Figure 5.7). This phenomenon is quantified in Section 5.4.2. Occasionally, the complexes experienced a stepwise drop in diffusion constant to zero, potentially indicating insertion of part of the protein into the bilayer and interaction with the hydrogel substrate (Figure 5.6). It was observed previously that inserted β-barrel pores in a DIB could be intentionally immobilised by dehydrating the hydrogel [101].

The injected protein sample for assembly experiments contained 1:5.5 lPFO:rPFO

and the total final protein concentration in the droplet was nominally approximately 37 nM. Both unlabelled rPFO and labelled lPFO were assumed to contribute to the assembled complexes, but the unlabelled rPFO was of course undetectable in smTIRF images. This assumption was supported by estimates of stoichiometry after accounting for unlabelled protein (Section 5.3), which agreed with the literature [21, 22, 39–42], and by similar haemolytic activity for both lPFO and rPFO (Figure 3.6).

In each iteration of protein injection and recorded assembly in Figure 4.2, the blue of the background grew brighter. This change was caused by lPFO monomers still binding to the bilayer throughout the recording. The imaging conditions for assembly capture are discussed in Section 3.3.

4.2.2 A concentration sweet spot

The transient nature of the assembly process imposed a limited time window in which to capture it. Constant imaging of the bilayer was necessary in anticipation of the process starting. The start time for assembly was governed by the number of monomers bound to the bilayer; oligomerisation only occurred above a threshold 2D monomer concentration, when the monomer-monomer encounter frequency was sufficiently high. The end of assembly was governed by oligomerisation exhausting the monomers bound to the bilayer, or saturation of the cholesterol binding sites, presuming the bilayer survived up until this point.

This discrete time window for the assembly process in turn imposed a sweet spot in the protein concentration injected into the 138 nl droplet. At low concentration the protein took many minutes to assemble into a significant number of complexes (see Section 4.3.1). Given the requirement for constant imaging mentioned above, waiting a long time for assembly to occur was undesirable, because the chance of fluorophores having photobleached increased with time during illumination.

Conversely, when the protein concentration was too high, assembly occurred

faster than it was possible to start recording after injection (around 20 s) and was only partially captured. For such high concentrations, the labelled monomers could on average be close to or less than 550 nm apart (the spatial resolution of the smTIRF experiments, Section 4.1), making single monomers difficult to resolve and complexes difficult to distinguish above the bright 'carpet' of monomers.

The quantity of protein injected into the droplet was optimised to cause assembly to occur between 30 s and 5 minutes after injection, the ideal time window given the imaging and physical constraints. As described in Section 3.2.2, a total protein concentration of 37 nM in the droplet was added by injection, and to maximise SNR and minimise self-quenching the ratio of lPFO to rPFO was 1:5.5. 37 nM was a nominal value, because as discussed in Section 3.2.3, the concentration of protein in the droplet was prone to error.

4.2.3 Comparing insertion events and assembled complexes

The number of functional rPFO pores reported by electrophysiology was low (Figure 3.12) in relation to the number of protein complexes detected by smTIRF (Figure 4.2). The nominal protein concentration in the droplet for electrophysiology was 13 nM, compared to 37 nM for the assembly videos. The concentration difference might explain the difference in the number of pore-like events reported by the two different types of bilayer interrogation.

For higher protein concentrations, bilayer rupture occurred suddenly before any insertions were observed during electrophysiological recording. However, by smTIRF many complexes were observed on the bilayer before rupture in assembly experiments. These combined observations further suggest that many of the complexes observed by smTIRF did not form inserted pores. Experiments are currently underway in our lab to perform simultaneous oSCR and labelled protein imaging, to determine whether it is indeed the case that few of the complexes observed by smTIRF insert a β-barrel into the bilayer (preliminary data is presented

in Figure 4.10).

Few assembled complexes forming inserted pores in a DIB is interesting, considering that others observed many insertion events caused by PFO even at concentrations of 176 pM, using a planar POPC/cholesterol bilayer [9]. All smTIRF experiments described herein were conducted at room temperature, which may explain the barrier to β-barrel insertion. Previous studies found that at 4°C, prepores assembled but the insertion mechanism was inhibited, while at 37°C insertion occurred freely [9]; others have mentioned that only prepores formed on liposomes at room temperature [24].

β-barrel insertion could also be influenced by the underlying hydrogel substrate of a DIB, though this does not stop αHL inserting [67], or a lower amount of cholesterol present in the bilayer than expected. It seems clear from the assembly videos that the amount of cholesterol was sufficient to permit oligomerisation, but previous reports have suggested that cholesterol is required not only for membrane binding but also for the prepore to pore transition [126, 127]. Finally, the use of DPhPC as the base lipid could influence insertion. Hopefully further experiments in which the temperature and the cholesterol and lipid content of the bilayer are systematically varied will clarify this issue.

4.3 Variations on assembly

4.3.1 Features of assembly at low 2D protein concentration

The significant variation in protein concentration injected into the droplet was discussed in Section 3.2.3. This variation meant it was difficult to perform experiments in which the concentration of protein was systematically adjusted. The variation in injected protein concentration was apparent from some bilayers exhibiting a relatively low 2D density of bound protein, some a relatively high 2D density (Section 4.3.2). The relatively low 2D protein concentrations were

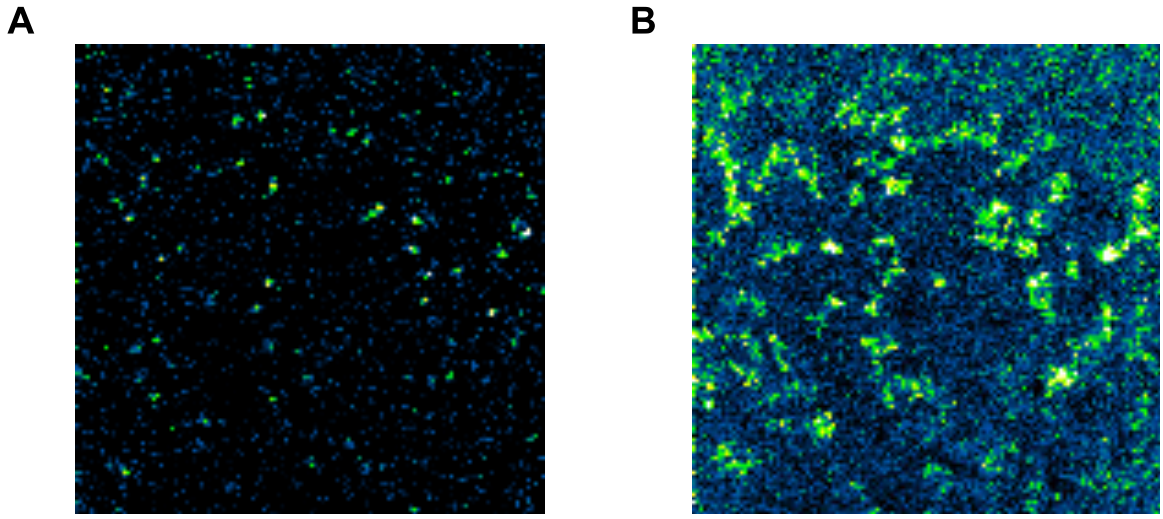


Figure 4.3: Resolving single PFO monomers. A 2.3 nl volume of lPFO:rPFO 1:12 was injected into a 138 nl droplet with a pre-formed DIB. The final total protein concentration in the droplet was nominally 30 nM. *A*, Single lPFO monomers can be resolved as yellow-green spots above the dark blue-black background signal. Due to noise, some relatively bright background pixels appear as light blue spots. *B*, Maximum pixel intensity projection of a sequence of 20 frames, including the frame shown in *A*. Taking the maximum pixel intensity from 20 frames effectively shows the path traced out by single molecules as they diffuse.

characterised by fewer monomers bound to the bilayer and fewer assembled protein complexes.

The observed variation in bound protein concentration could also be explained by a varying number of cholesterol binding sites within the bilayer, but the cholesterol content was determined during the lipid solution preparation step with greater handled volumes (Section 3.1) and should be significantly less prone to error than the tiny volume of injected protein.

At a particularly low concentration single labelled monomers were readily resolvable diffusing on the bilayer, too dilute to assemble into complexes in a reasonable imaging time frame. In contrast to experiments designed to image CDC assembly, a higher laser power was acceptable when imaging single diffusing monomers. The incident laser power at the back aperture of the objective lens was increased to 0.9 mW to improve the SNR of the single monomers (after partial shuttering in the excitation pathway to avoid photobleaching outside the field of view; unshuttered, 3.7 mW), compared to 0.06 mW (also partially shuttered, Section

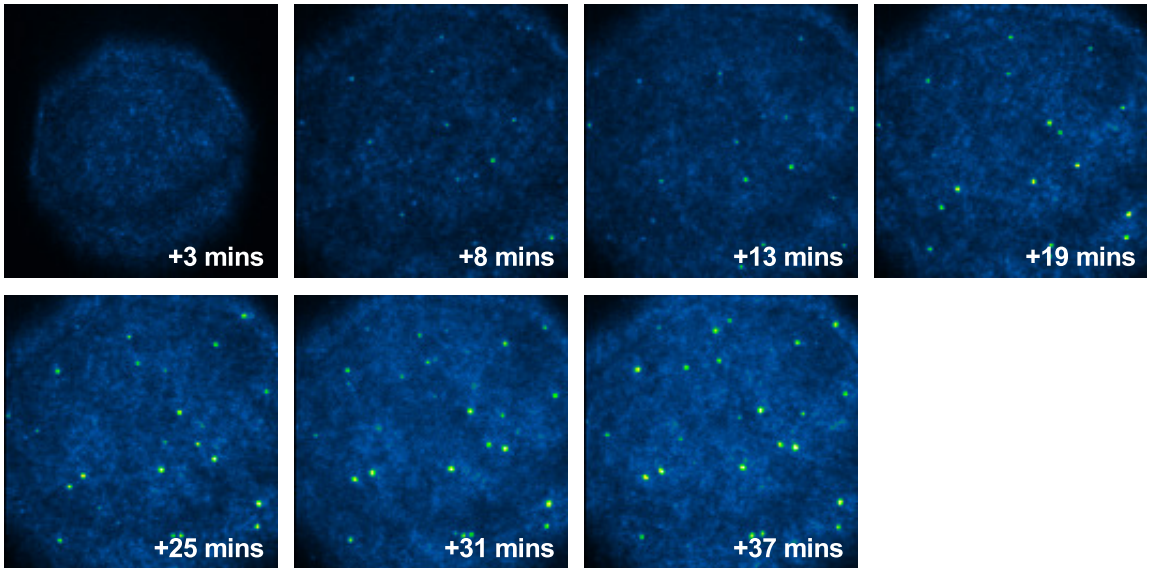


Figure 4.4: Time-lapse recording of lPLY assembly. lPLY was injected into a droplet with a pre-formed DIB to a nominal final concentration of 70 nM. At 5-6 minute intervals over the next forty minutes, a 2.5 s recording was taken at 50 ms per frame. 2.5 s was enough time to allow refocusing. Over a timescale of minutes, monomers continued to bind to the bilayer, evidenced by the background getting brighter; more complexes formed as a consequence (brighter yellow-green spots).

3.3) for assembly capture experiments. Figure 4.3A presents a snapshot of single lPFO monomers diffusing on the bilayer.

Figure 4.3B highlights the dynamic nature of the single molecules, by projecting onto a single image the maximum pixel intensity of a 20-frame series (60 ms per frame), from which the single frame in A was taken. The projection reports the maximum intensity experienced by the pixels in the course of the 20 frames, effectively storing all the positions occupied by single labelled monomers in that time. As expected for random motion, some monomers stayed in roughly the same position while others travelled relatively far in one direction. Using custom software developed within our research group, based on mean squared displacement (MSD) fitting, the diffusion coefficient of these monomers was calculated to be around 1.5 $\mu m^2 s^{-1}$. The lateral motion of the monomers appeared to be Brownian, as expected on the DPhPC/cholesterol DIB, which lacks domains and the crowded components and cytoskeleton of a natural biological membrane.

Some bilayers exhibited assembly of complexes over a timescale of minutes rather

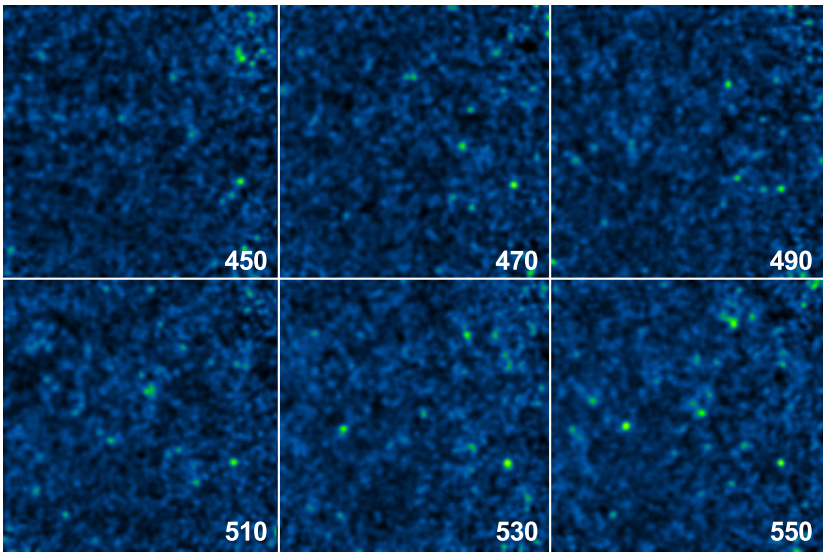


Figure 4.5: Assembly at low 2D protein concentration. Equivalent montage to Figure 4.2, except that due to the error on injected protein concentration, this bilayer exhibited slower assembly with fewer complexes. Note the longer time between frames in this montage. The images have been filtered with a Gaussian function, $\sigma = 1$ pixel.

than seconds. At this timescale, constant imaging of the bilayer was impractical due to photobleaching of the fluorophores, even at the lower laser power employed for assembly capture. Moreover, the large amount of data generated and the capability of the video-capturing software prevented constant imaging for many minutes at a time. However, an alternative approach to recording assembly was to perform time-lapse imaging, as demonstrated in Figure 4.4. lPLY was injected to a nominal concentration of 70 nM in the droplet. At 5-6 minute intervals over the next forty minutes, a 2.5 s recording was taken at 50 ms per frame. This recording time allowed refocusing at each iteration, and a frame from each recording is presented in Figure 4.4. A time-lapse approach rather than constant imaging prevented excessive photobleaching of the fluorophores on the bilayer, while still capturing some details of lPFO assembly. The number of complexes apparent in the field of view of the bilayer slowly increased over the forty minute period.

Finally, Figure 4.5 presents an example of lPFO assembly similar to those shown in Figure 4.2, but at a slightly lower rate, recorded continuously. Though assembly occurred faster than the tens of minutes for lPLY in Figure 4.4, the video was

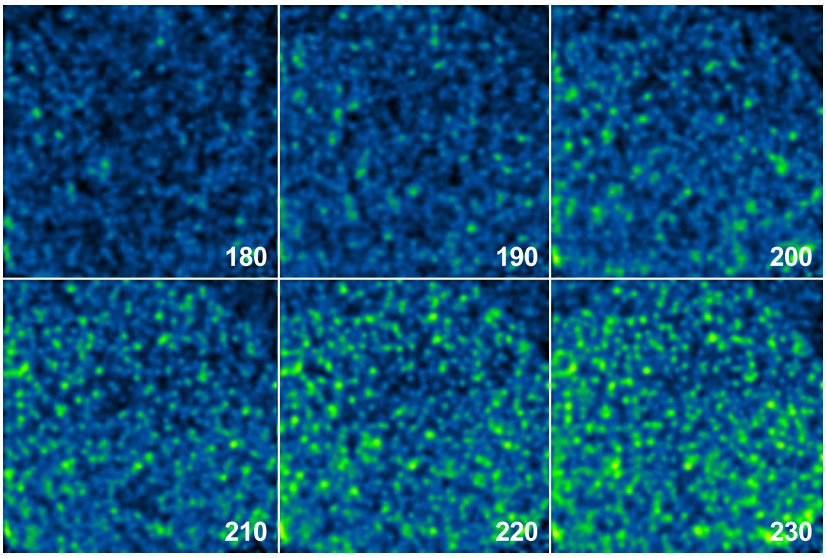


Figure 4.6: Assembly at high 2D protein concentration. Equivalent montage to Figure 4.2, except that due to the error on injected protein concentration, this bilayer exhibited many more complexes on the bilayer. The time taken for assembly to occur was longer, however, suggesting that perhaps cholesterol concentration was not constant between this bilayer and those in Figure 4.2, complicating the assembly kinetics. Alternatively, heating of the illuminated bilayer region by the TIRF field could potentially have influenced the assembly time. The images have been filtered with a Gaussian function, $\sigma = 1$ pixel.

sufficiently long that photobleaching may have occurred (Section 4.4), complicating stoichiometry estimates for the complexes. Photobleaching in assembly videos was difficult to quantify as labelled monomers were constantly binding to the bilayer. In any case, too few individual complexes appeared in the course of this video to statistically quantify their assembly mechanism.

The Figures 4.3-4.5 are intended to deconstruct the nature of assembly at low concentrations, starting with no assembly (single monomers that do not encounter each other sufficiently to oligomerise), through assembly on the order of tens of minutes, to a rate of assembly almost high enough to statistically quantify, on the order of minutes.

4.3.2 Features of assembly at high 2D protein concentration

In contrast to Figure 4.5, at the other end of the 2D protein density range, Figure 4.6 displays a bilayer almost carpeted in protein complexes. This effect was caused

by a high concentration of monomers and complexes bound to the bilayer. However, it is worth noting that because the bright spots representing the complexes were an order of magnitude larger in diameter than the complexes themselves (Section 4.1), it could appear that the bilayer was covered with complexes when actually there was still hundreds of nanometres between them.

Often, the protein caused the bilayer to rupture before this 2D density of complexes was reached. For comparison, images obtained by EM (Figure 1.6) suggest that monomers are entirely capable of oligomerising to the point where the bilayer is completely carpeted. Rupture of the DIB at these high complex densities is difficult to relate to natural biological membranes, which are more complex and are supported in cells by the cytoskeleton.

4.3.3 PLY assembly

Over several assembly experiments, lPFO/rPFO seemed to behave more robustly from bilayer to bilayer than lPLY, under potential variations in protein and cholesterol concentration and hydrogel hydration. Moreover, PFO generally seemed to oligomerise at lower concentrations than lPLY (compare lPFO Figures 4.2, 4.5 and 4.6 with lPLY Figures 4.4 and 4.7), though this observation was not tested explicitly. Capturing assembly was therefore attempted mostly with lPFO/rPFO rather than lPLY, and the analysis in Chapter 5 refers to lPFO/rPFO assembly.

Nevertheless, assembly of lPLY was captured, as demonstrated in Figure 4.7 (and also in Figure 4.4). The pattern of assembly was qualitatively similar to that for PFO (Figure 4.2), though the features were not yet quantitatively compared. The protein concentration was relatively low in Figure 4.7, as evidenced by the long time taken for assembly to occur, and as mentioned previously, lPLY did not generally seem to oligomerise to the same extent as lPFO/rPFO at similar concentrations.

The SNR for lPLY complexes in Figure 4.7 was not dissimilar to that of rPFO/lPFO complexes (Figures 4.2, 4.5 and 4.6), despite the 91 % labelled fraction

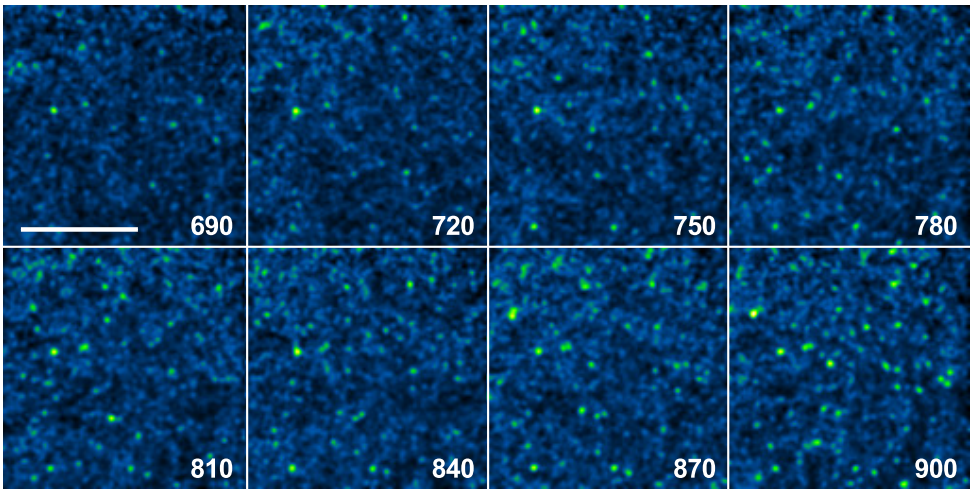


Figure 4.7: PLY assembly imaged by smTIRF. lPLY was injected into a droplet with a pre-formed DIB to a nominal final concentration of 70 nM. As with lPFO/rPFO in Figure 4.2, protein complexes formed by oligomerisation once sufficient monomers had bound to the bilayer. The images have been filtered with a Gaussian function, $\sigma = 1$ pixel. Scale bar 25 μm.

in the lPLY sample compared to the $1/6.5 = 15$ % labelled fraction in the rPFO/lPFO sample. This observation suggests that either self-quenching had a significant effect on the intensity of the lPLY complexes, or that lPLY was forming relatively small stable oligomers in this video. Either way, the possibility of self-quenching justified the decision to inject a mixture of labelled and unlabelled protein in assembly experiments, rather than purely labelled protein.

4.3.4 Oligomer-based assembly

In structural investigations of CDCs, irregular multi-arc/ring complexes have repeatedly been observed (see Section 1.1.4). Such complexes include interlocked arcs as well as arcs bound at the ends [25, 27]. In the examples in Figures 1.9C and 1.8D, an AFM tip was scanned over these complexes and penetrated through to the mica support in their lumen, confirming their ability to form functional pores.

The smTIRF technique in this study could not resolve monomer structure in the protein complexes, but putative irregular multi-arc complexes could be identified by their unusually high intensity. After calibrating intensity with stoichiometry (Section 5.3), the brightest complexes contained over 100 subunits. Such high

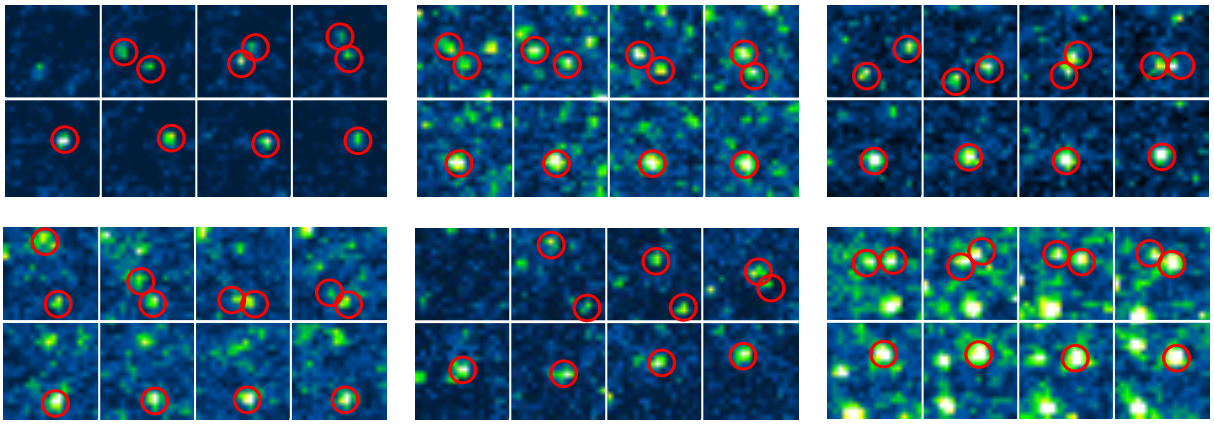


Figure 4.8: Oligomer-oligomer assembly. Two oligomeric (brighter than single-fluorophore) complexes that encountered each other while 2D-diffusing occasionally bound and either diffused away together or remained stationary together. The montages show some examples; the frames correspond to -10, -5, -2.5, -1.25, 0, +1.25, +2.5 and +5 seconds relative to the binding event. The input complexes and output complex are highlighted with red circles. The most likely explanation for these events are the multi-arc complexes, bound end-to-end or interlocking, observed with EM and AFM (Figure 1.6, 1.9).

stoichiometry could also be explained by several distinct complexes in a similar location but not interacting, however the nature of assembly for the large complexes, discussed below, suggested multi-arc complexes were the cause in many cases.

Tracing their assembly backwards, unusually bright complexes often formed by the binding of two oligomers, the 'input' complexes, which had diffused into the same location and subsequently followed a single trajectory. The colocalisation of the input complexes for a longer duration than could occur by random diffusion confirmed that they had bound together, forming an 'output' complex. Some examples are presented in Figure 4.8. Notably, the binding of input complexes did not only result in the formation of high-stoichiometry output complexes; small complexes with around 20 subunits often bound to form complexes with stoichiometry similar to typical CDC rings (30-50 subunits [21,22,39–42], see Section 5.5.3). Diffusion of the output complex was generally reduced due to its larger size.

In light of the EM and AFM images, the input complexes were presumed to be arcs, the output complexes irregular multi-arc complexes with the arcs bound end to end or in some cases interlocking. Figure 4.8 is quantified in Section 5.5.3.

4.4 Photobleaching of CDC complexes

4.4.1 Brief introduction to photobleaching

Photobleaching is the irreversible destruction of the fluorescent mechanism of a fluorophore under excitation (typically by reaction of the fluorophore with singlet reactive oxygen species, which are created by the interaction of excited fluorophores with molecular oxygen) [70–72]. In a fluorescence experiment, each time a fluorophore is excited there is a chance it will photobleach, rather than undergoing the desirable fluorescence de-excitation pathway. As there is a small constant probability that the fluorophore will photobleach at each excitation, the likelihood of photobleaching increases with the number of excitations. A higher number of excitations is caused by imaging with a higher laser power (more excitations per second) or for a longer time. As mentioned in Section 4.2.2, imaging labelled CDC monomers for a long time prior to their assembly into complexes, when the injected protein concentration was low, was undesirable due to the greater chance of photobleaching.

A common technique in single-molecule biophysics is to use photobleaching of fluorophores attached to protein molecules to measure the stoichiometry of multi-subunit assemblies [128–131]. In smTIRF image sequences, photobleaching of a single fluorophore appears as a stepwise drop in intensity to a dark state. When imaging multi-subunit assemblies in which the subunits are each labelled with a fluorophore, the stoichiometry of the complex can be measured by counting the number of stepwise drops in intensity as successive fluorophores photobleach.

4.4.2 Estimating CDC stoichiometry by stepwise photobleaching

Subunit counting by photobleaching was undertaken with lPFO after allowing complexes to assemble in the dark, as illustrated in Figure 4.9. Figure 4.9A

shows that, over the course of imaging, the summed intensity from monomers and complexes gradually decreased. Many bright complexes finished the recording completely dark. Plotting the intensity of complexes over time and then applying a step-finding algorithm to the traces highlighted the stepwise decrements due to photobleaching (Figure 4.9B-F). The step-finding algorithm is further discussed in Section 5.4.3.

The histogram in Figure 4.9G reveals the most common step-size for a photobleaching step (median = -1.4 a.u.). The step-finder was adjusted to only include negative steps, because positive steps could either be due to diffusion of other complexes or monomers across the region of interest, or to 'photoblinking', neither of which would alter the sum of negative steps if the complex ultimately reached a completely dark state. The total range of intensity divided by the average step-size would not be affected by up-steps and would still report stoichiometry. A visual inspection of the number of steps in the photobleaching traces in Figure 4.9C-F, accounting for some double- or triple-steps and some falsely identified steps, suggested a typical number of fluorophores in each complex was 10-13. This value was also obtained by dividing the intensity range by the median step-size.

However, an equivalent analysis was performed on a random position in the bilayer, not containing a bright complex. The intensity range of photobleaching traces in the absence of a complex was around 3-5 a.u., due to the high density of monomers and small complexes diffusing on the bilayer (data not shown, but some of the upwards steps in Figures 4.9D and E are representative). After correcting for the monomer background, the number of fluorophores in the tracked complexes in Figure 4.9 was therefore closer to 5-10. Assuming the labelling ratio of 1:5.5 was approximately accurate, the average number of monomers per complex was 32-65.

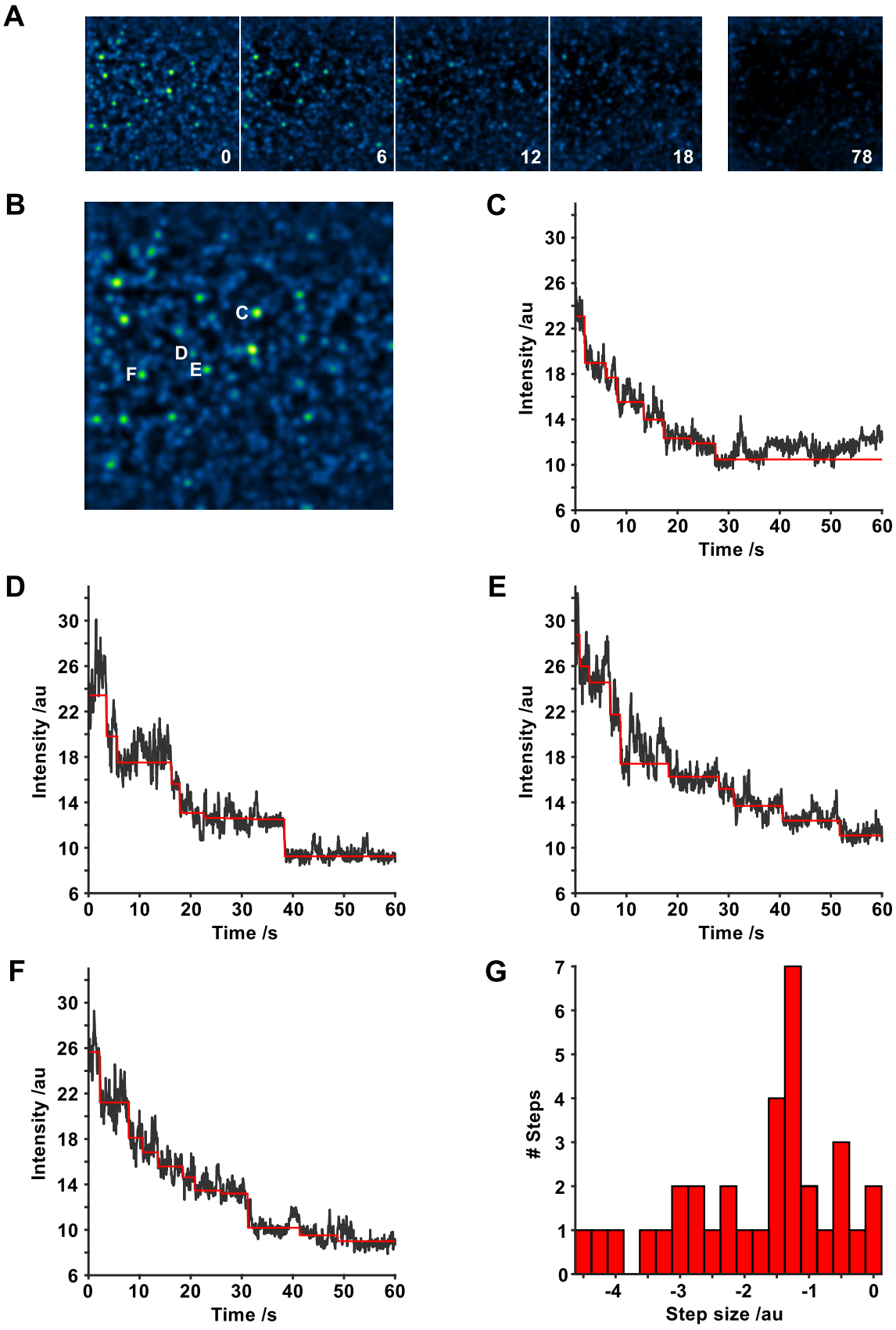

A
0
6
12
18
78
B
C
D
E
F
C
Intensity /au
Time /s
D
Intensity /au
Time /s
E
Intensity /au
Time /s
F
Intensity /au
Time /s
G
Steps
Step size /au

Figure 4.9: Counting subunits in PFO complexes by stepwise photobleaching. 1:5.5 lPFO:rPFO complexes were allowed to assemble in the dark, then imaged by smTIRF with a 0.9 mW laser power at the objective lens back aperture. *A*, A montage illustrating photobleaching of lPFO on a DIB. The frames displayed occurred at the indicated number of seconds after imaging was initiated. *B*, An enlarged image of the 0 s frame in *A*, to highlight the spots selected for further analysis. The labels indicate the spots referred to by subsequent panels in the figure. The images in *A* and *B* have been filtered with a Gaussian function, $\sigma = 1$ pixel. *C*-*F*, Mean intensities, throughout photobleaching, of a small region of interest (4×4 pixels) around the spots indicated in *B*. The result of a step-finding algorithm applied to the traces, with only negative steps included, is overlaid in red. *G*, A histogram of the step-sizes from *C*-*F*, median step-size = -1.4 a.u. After the monomer background correction and calibration for stoichiometry (see text for details), the number of monomers per complex in this image was estimated at 32-65.

4.4.3 Photobleaching with assembly

The analysis in Figure 4.9 is not rigorous. The principal reason for the sparsity of photobleaching data is that stoichiometries necessarily had to be measured after significant assembly of protein complexes on the bilayer had occurred. However, it was common during assembly capture that very shortly after significant assembly occurred, the bilayers ruptured and the droplets burst, preventing any further useful imaging. Experiments were attempted in which assembly was recorded at low laser power, then subsequently the power was increased for photobleaching of assembled complexes; the added complexity of these experiments, combined with the tendency of bilayers to rupture after assembly, made them difficult to optimise and ultimately unfeasible.

Moreover, photobleaching was only useful to determine the stoichiometries of complexes at equilibrium (after assembly had reached completion), whereas for this study a more important quantity was the stoichiometry of complexes during assembly. To estimate stoichiometry during assembly, an estimate of the single-fluorophore intensity at 0.06 mW was required (Section 5.3). Calibrating the single-fluorophore intensity at 0.06 mW with the 0.9 mW estimate would have been challenging, because of the potentially non-linear relationship between laser power density and fluorescence emission of the complexes, and the need to calibrate under exactly equivalent conditions to the assembly experiments.

For the assembly capture experiments, the laser power of 0.06 mW was partly chosen to avoid photobleaching, so stoichiometry was calculated by alternative means (Section 5.3). No photobleaching was apparent at 0.06 mW: monomers were so dim as to be difficult to resolve (Figure 5.4A), and the overall intensity of the bilayers during assembly only increased from the binding of more labelled monomers; there was no decrease in overall intensity due to photobleaching.

4.5 Preliminary results from two-colour imaging of oSCRs and labelled monomers

To complete the set of qualitative results in this chapter, some preliminary experiments exploiting the capacity of DIBs for simultaneous oSCR and smTIRF imaging of labelled protein are presented in this section.

The functionality of pores was investigated by the flux of Ca^{2+} through PFO pores causing SCCaFTs (Section 3.4.3); the Fluo-8 was excited by a blue (474 nm) laser. The extent of oligomerisation, the presence of both monomers and complexes on the bilayer, was investigated by labelling the protein with Alexa Fluor® 647 (a647) to create 1:1 labelled recombinant perfringolysin O, $PFO^{C459A,E167C}$-a647 (lPFO-a647), and imaging the lPFO-a647 with a red (644 nm) laser.

'Two-colour' imaging was possible because the a488 and a647 fluorophores are spectrally distinct; a precise combination of excitation and emission filters and dichroic mirrors allowed simultaneous TIRF in both the red and blue channels, and separated the emission from the two fluorophores. An optosplit (Optosplit II, Cairn Research) directed the two emission channels onto separate halves of the EMCCD.

Preliminary results are presented in Figure 4.10. 1:5.5 lPFO-a647:rPFO was injected into a droplet with a DIB. In accordance with previous results (Section 4.2.3), few insertions were detected by oSCR; repeats typically revealed around one or two SCCaFTs per bilayer. However, as illustrated in Figure 4.10, the 2D

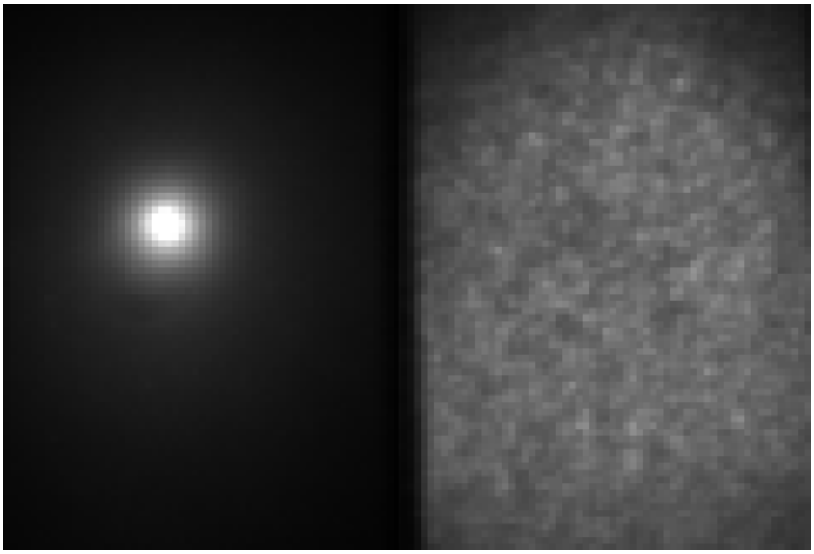


Figure 4.10: Two-colour oSCR and labelled PFO imaging. *Left*, SCCaFT induced by 1:5.5 lPFO-a647:rPFO, imaged by the blue illumination and detection channel. *Right*, A simultaneous smTIRF image of 1:5.5 lPFO-a647:rPFO monomers and oligomers, imaged via the red channel. The pore conductance is detected by the SCCaFT, the geometric arrangement of the PFO population by the labelled monomers. The SNR with the a647 label is weak, and the labelled monomers appear to carpet the bilayer, so it is difficult to resolve individual complexes. This is preliminary data, not yet fully analysed. The images have been filtered with a Gaussian function. This image is a median projection of 300 frames. Data courtesy of C. Monico.

concentration of protein was high, apparently carpeting the bilayer. Individual complexes have been resolved with lPFO-a647/rPFO, but so far SCCaFTs have only occurred at the high 2D concentrations where distinguishing separate complexes in the red channel was difficult. Imaging of the labelled monomers was severely affected by the apparently low photostability of a647.

This type of experiment has not yet been attempted at 37°C. Previous reports suggest that temperature has a significant impact on the ability of monomers in the prepore state to insert a pore [9, 24]. We anticipate that conducting experiments at 37°C will increase the number of observed insertions, and that some of these pores will be detected in both channels.

The goal of these experiments is to further understand the relationship between the number of assembled complexes and the number of inserted pores. Furthermore, by capturing assembly with two-colour imaging, the insertion of pores could be time-resolved with respect to oligomerisation. Such an experiment would reveal the

average time spent in the prepore state before insertion, for example. This result would also be significant from a technical perspective: the ability to study protein conformation and function simultaneously using labelled subunits and oSCRs is desirable in applications beyond CDCs.

In summary, this chapter presented smTIRF videos of CDC assembly. The videos represented in Figure 4.2 provide the first real-time observation of individual CDC complex assembly at temporal resolution higher than minutes. The sacrifice in achieving high temporal resolution was a reduction in spatial resolution, relative to the recent AFM experiments that also addressed the dynamics of assembly [25, 27]. This chapter provided a qualitative interpretation of assembly, by comparing assembly at different 2D protein concentrations, observing an irregular mechanism of assembly, and measuring stoichiometry of complexes by stepwise photobleaching. The next chapter describes analysis of the smTIRF videos of assembly, to discriminate between potential assembly mechanisms and to detail the kinetics of CDC assembly.

Chapter 5

Quantifying cholesterol-dependent cytolysin assembly

Chapter 4 presented the first video frame-rate real-time recordings of the assembly of individual CDC complexes. This chapter investigates the assembly mechanism of the CDCs using these videos. On their own, the videos provide a qualitative idea of the timescale for assembly and they corroborate the EM and AFM observations of irregular multi-arc complexes. To extract more information from the videos, the protein population and the individual complexes were characterised quantitatively, which required single particle tracking of the complexes.

5.1 Single particle tracking

Single-particle tracking (SPT) is a common technique in the analysis of biophysical sm-fluorescence images [132]. It is used to understand the biological function of labelled molecules by their motion or diffusion. In this study, SPT was applied to single CDC complexes and monomers. The algorithms used to identify and link spots in consecutive frames were supplied by the TrackMate plugin for Fiji (ImageJ) [133–135].

Before applying the tracking algorithm, videos were processed to correct for

artefacts, such as uneven illumination, that would corrupt the intensity values. Even in the complete absence of any incident light on the EMCCD camera (closed shutter in the dark), the reported average pixel intensity was a non-zero value. This background value was subtracted from the videos of CDC assembly. The videos were then divided by a median intensity projection of a number of frames (typically 50 frames) from the same bilayer, in which there were no stationary spots and as few labelled monomers as possible (prior to assembly). This median projection correction accounted for the non-uniform illumination profile in the videos: the laser was uneven across the field of view, because of the inherently Gaussian profile of a laser beam, and dust particles and filter surfaces causing the laser light to refract and interfere [136]. Dividing by the median ensured a uniform background in the assembly videos, and allowed separate bilayers to be compared directly.

The corrected videos were subjected to the TrackMate algorithm [133], which identifies spots by producing two Gaussian filtered versions of the original frame, with different standard deviations used for each Gaussian kernel. The image with the large standard deviation kernel is subtracted from that with the small standard deviation kernel, resulting in a smoothed image with sharp maxima at spot locations. Spurious spots are filtered out by the 'quality' parameter, which reflects SNR. Tracking was performed using the linear assignment problem framework in TrackMate [132]; a matrix is created containing cost values for both linking and not linking spots in consecutive frames (gaps can also be dealt with), for all possible links. This matrix is then solved to minimise the total cost and determine the actual links.

Figure 5.1 highlights some representative tracks obtained using TrackMate. The input parameters to track spots included maximum frame-to-frame linking distance, estimated spot diameters, and the number of frames a spot could be absent within a track before the track was separated into two. The parameters were adjusted until the spots were tracked most accurately as assessed by eye, though work is under

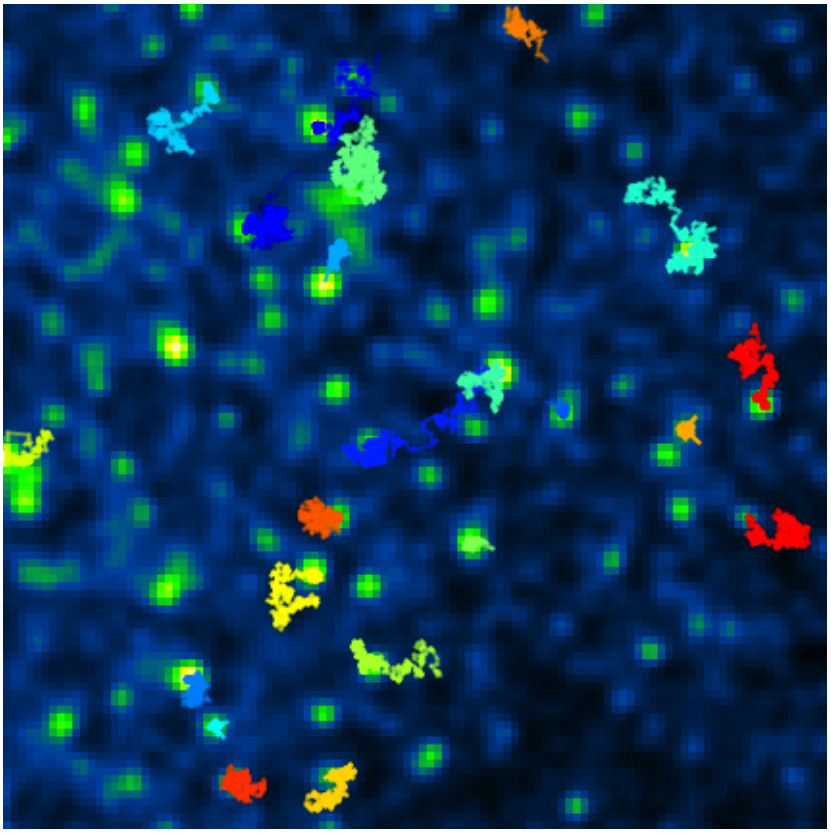


Figure 5.1: Frame from smTIRF assembly recording with superposed tracks. Representative output from TrackMate superposed on a frame from the rPFO/lPFO assembly video in Figure 4.2A (the video was subsequently filtered with a Gaussian function, $\sigma = 1$ pixel). Only a few tracks of the >100 detected within the video have been displayed for clarity.

way in our lab to automate the statistically optimal choice of tracking parameters. (Tracking parameters were as follows: Detector: LoG, Estimated blob diameter = 3 pixels, Threshold = 0.067 a.u., Median filter: no, Sub-pixel localisation: yes, Tracker: Simple LAP tracker, Linking max distance = 2.5 pixels, Gap-closing max distance = 2.8 pixels, Gap-closing max frame gap = 2 frames. 1 pixel = 0.4 μm.)

The track coordinates outputted by the TrackMate algorithm were stored and could be plotted separately, as illustrated in Figure 5.2. These coordinates are used in the next section to extract intensities for the tracked spots. All subsequent analysis was performed with bespoke code and inbuilt functions in Matlab, unless otherwise stated.

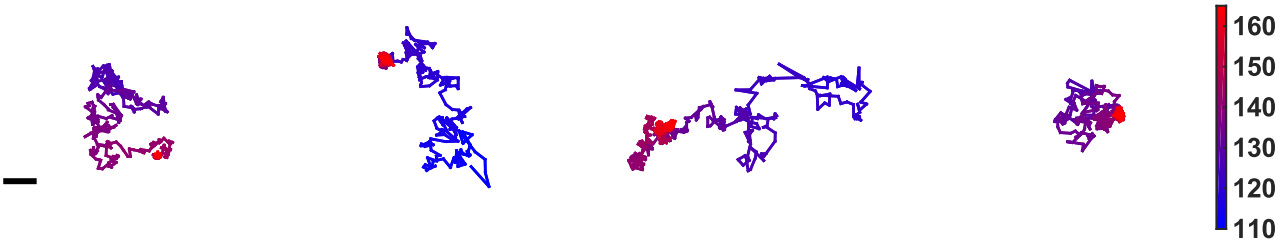


Figure 5.2: Motion of CDC complexes revealed by single particle tracking. The output coordinates from TrackMate for four representative assembling complexes from the rPFO/lPFO assembly video in Figure 4.2A. Scale bar, 1 µm. Colour bar indicates time in seconds since injection of protein into the 138 nl droplet.

5.2 Intensity extraction

To quantify the assembly of the complexes that appear as bright spots in Figure 4.2, it was necessary to extract their intensity over time. Intensity is analogous to stoichiometry via a calibration factor, discussed in Section 5.3. However, because the EMCCD is comprised of discrete pixels, the detected light corresponding to a spot was spatially discretised in the recorded images. The maximum pixel intensity of a tracked spot is one representation of the amount of light originating from a particular fluorophore or collection of fluorophores, but it does not consider all the relevant photons, only those from the brightest pixel (Figure 5.3).

The psf of a point source such as a fluorophore in a 2D image is approximated by a symmetric 2D Gaussian function [123]. To overcome the spatially discretised intensity, and to provide a higher SNR by accounting for all of the photons from a tracked complex that were incident on the detector, the tracked spots were fitted with a 2D Gaussian function. The fitted function is given by Equation 5.1, it was fitted to a 5 × 5 pixel grid around each coordinate in a track.

$$f(x,y) = \boldsymbol{c} + \boldsymbol{A}\exp\left(-\left(\frac{(x-\boldsymbol{x_0})^2}{2\boldsymbol{\sigma}^2} + \frac{(y-\boldsymbol{y_0})^2}{2\boldsymbol{\sigma}^2}\right)\right) \tag{5.1}$$

In Equation 5.1, c is an effective background, A is the amplitude of the function, x_0 and y_0 are the position of the maximum relative to the 5 × 5 grid, and σ is the standard deviation of the symmetrical function. The symbols in bold in Equation

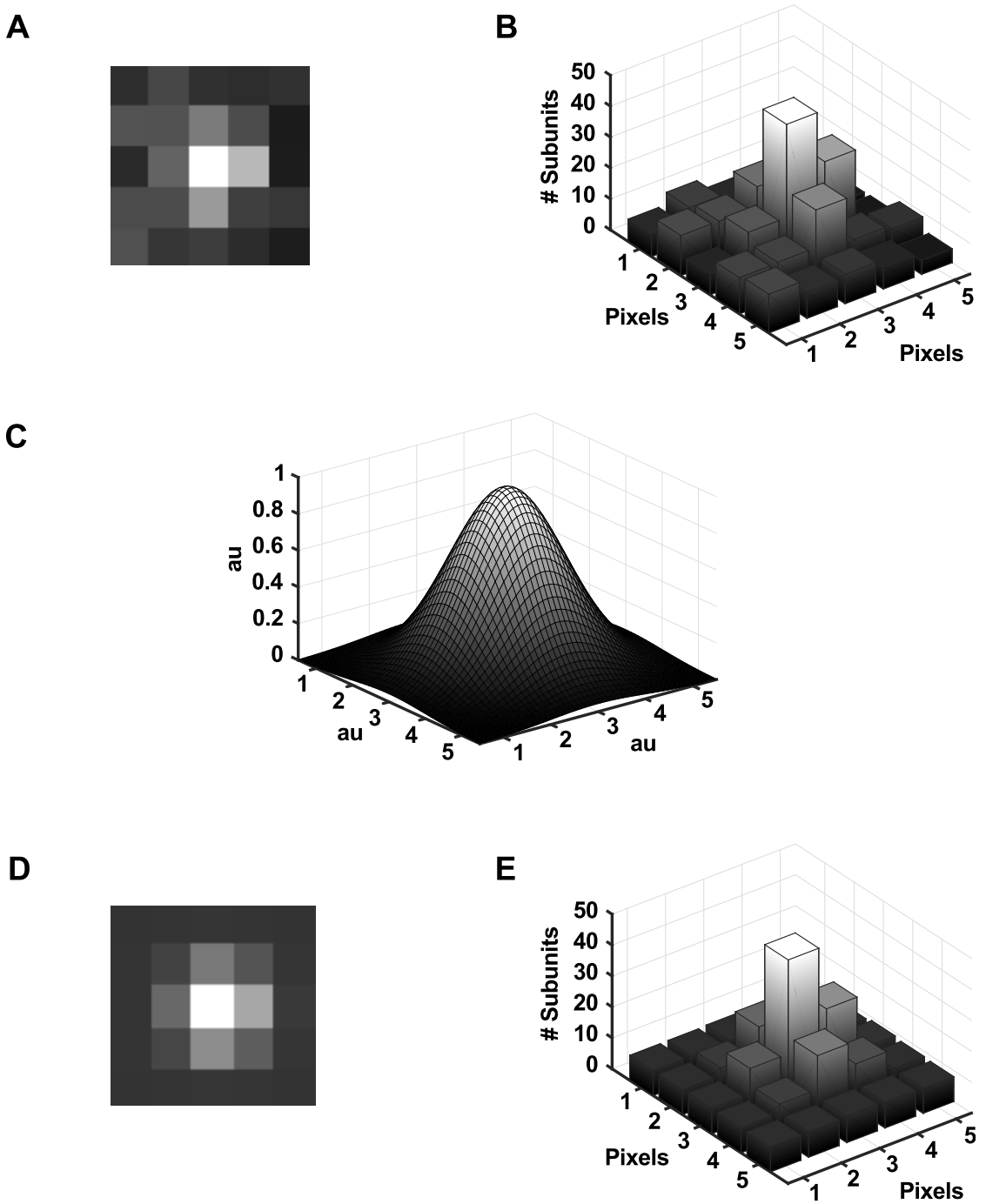


Figure 5.3: Intensity of bright spots estimated by Gaussian approximation. *A*, A representative spot from the second track in Figure 5.2. *B*, 3D rendering of the spot in *A*. *C*, To obtain a reliable and accurate value for the intensity of a complex, a symmetric Gaussian function (Equation 5.1) was fitted to the spatially discretised spot exemplified in *B*. *D-E*, To verify the accuracy of the fitted function, the theoretical equivalent representations to *A* and *B* were derived by feeding the fitted parameters back into Equation 5.1 and plotting the result on a discrete grid. The fitted results accurately capture the raw data in *A* and *B*.

5.1 represent free parameters in the fit (c, A, x_0, y_0, σ). The free parameters were bounded to ensure sensible fitting: $\min(x_0, y_0) = 0$ pixels, $\max(x_0, y_0) = 5$ pixels;

$\min(c) = 0.01$ a.u., $\max(c) = 1$ a.u. (after dividing by the median projection, average background intensity is 1); $\min(A) = 0.01$ a.u., $\max(A) = 1.3 \times$ {maximum pixel intensity in grid} a.u.; $\min(\sigma) = 0.5$ pixels (effective minimum width 1 pixel), $\max(\sigma) = 3$ pixels (effective maximum width 6 pixels).

The fit was performed using the *lsqnonlin* function in Matlab, which minimised the sum of squared residuals between the fitted function and the raw data. The amplitude A of the fitted Gaussian was used to represent the amount of light originating from a labelled monomer or complex, it was the value accepted for the intensity of a spot. The fitting principle is illustrated in Figure 5.3. The stoichiometry of the complexes was subsequently calculated from the intensity of their corresponding bright spots.

5.3 Estimating stoichiometry of CDC complexes during assembly

To determine the assembly kinetics of PFO, the stoichiometry of complexes over the course of the assembly process was estimated. To determine the stoichiometry of individual complexes, the intensity of the spot was first divided by the intensity of a single fluorophore, to estimate the number of fluorophores in the complex. The ratio of lPFO:rPFO on the bilayer was 1:5.5, so one fluorophore actually represented 6.5 monomers. The estimated number of fluorophores per complex was multiplied by 6.5 to estimate the number of monomers per complex. There was therefore an inherent minimum error in the stoichiometry estimates of $\pm$ 5.5.

The actual number of monomers per complex is of course not always 6.5 times greater than the number of fluorophores; the stoichiometry distribution calculated will be broader than the actual stoichiometry due to the stochastic nature of lPFO incorporation into complexes. This variation in stoichiometry is alleviated by averaging over many complexes, such as for the kinetics outlined in Section 5.6.

Previously, when measuring stoichiometry by the intensity of labelled subunits, others have accommodated partial labelling by fitting the stoichiometry distributions with a binomial distribution [131, 137]. However, these studies were investigating low-stoichiometry complexes (typically 3-4 subunits) where a binomial distribution of labelled subunits within a complex was appropriate. For the significantly higher stoichiometries of CDCs in this study, a simple linear calibration factor (multiplying by 6.5) was deemed sufficient.

The single-fluorophore intensity and therefore the time-dependent stoichiometry of complexes was estimated by more than one method, detailed below. The different approaches, though not robust individually, were consistent with one another and strongly suggested that the intensity value obtained for a single fluorophore was a fair estimate. In the future, the 'number and brightness' method, which can combine fluorescence correlation spectroscopy with wide-field imaging [81], will be investigated as it may provide useful information regarding the intensity of single fluorophores in this study.

5.3.1 Photobleaching estimates

The subunit-counting by photobleaching method [128–131] was applied to a few assembled rPFO/lPFO complexes in Section 4.4. This analysis suggested that the complexes at equilibrium contained around 32-65 subunits. However, because the analysis was performed at the higher 0.9 mW laser power, and only at equilibrium after assembly had reached completion, it did not help with measuring stoichiometry during assembly (as discussed in Section 4.4.3). Moreover, this method could not be used to calibrate stoichiometry for all iterations of protein injection and assembly, as often the bilayers ruptured before equilibrium was reached. However, the stoichiometries estimated by photobleaching were used to verify the stoichiometries estimated by other methods in this section, and the two were found to approximately agree with each other.

5.3.2 Tracking of single monomers

The single-fluorophore intensity was first estimated from single labelled monomers, tracked early in the assembly videos when few of them were bound to the bilayer. Tracking parameters were adjusted to track the dimmer single fluorophores. The low intensity of these spots is apparent in Figure 5.4A, therefore maximum pixel intensity was used to measure these spots' intensities (not Gaussian fitting). The maximum pixel intensities of all the tracked single-fluorophore spots were plotted in a histogram, Figure 5.4B. The histogram was fitted with a 1D log-normal function and the single-fluorophore intensity estimated by the position of the peak.

The single-fluorophore intensity estimated from the peak position in Figure 5.4B was approximately 3 a.u. (after subtracting the mean background intensity = 1 a.u.). This value was used to estimate the number of fluorophores in a complex from its intensity. The resulting distribution of stoichiometries from this single-fluorophore value is displayed later in Figures 5.13, 5.15 and 5.16. Furthermore, the stoichiometries listed in Figure 4.2 were calculated using this value. Briefly, a modal stoichiometry for assembled complexes was around 30-40, with some exceptionally high stoichiometries present as discussed in Section 4.3.4. This result agrees with the expected stoichiometry for PFO complexes [41, 42], and is within the range of stoichiometries suggested by photobleaching in Section 4.4.2.

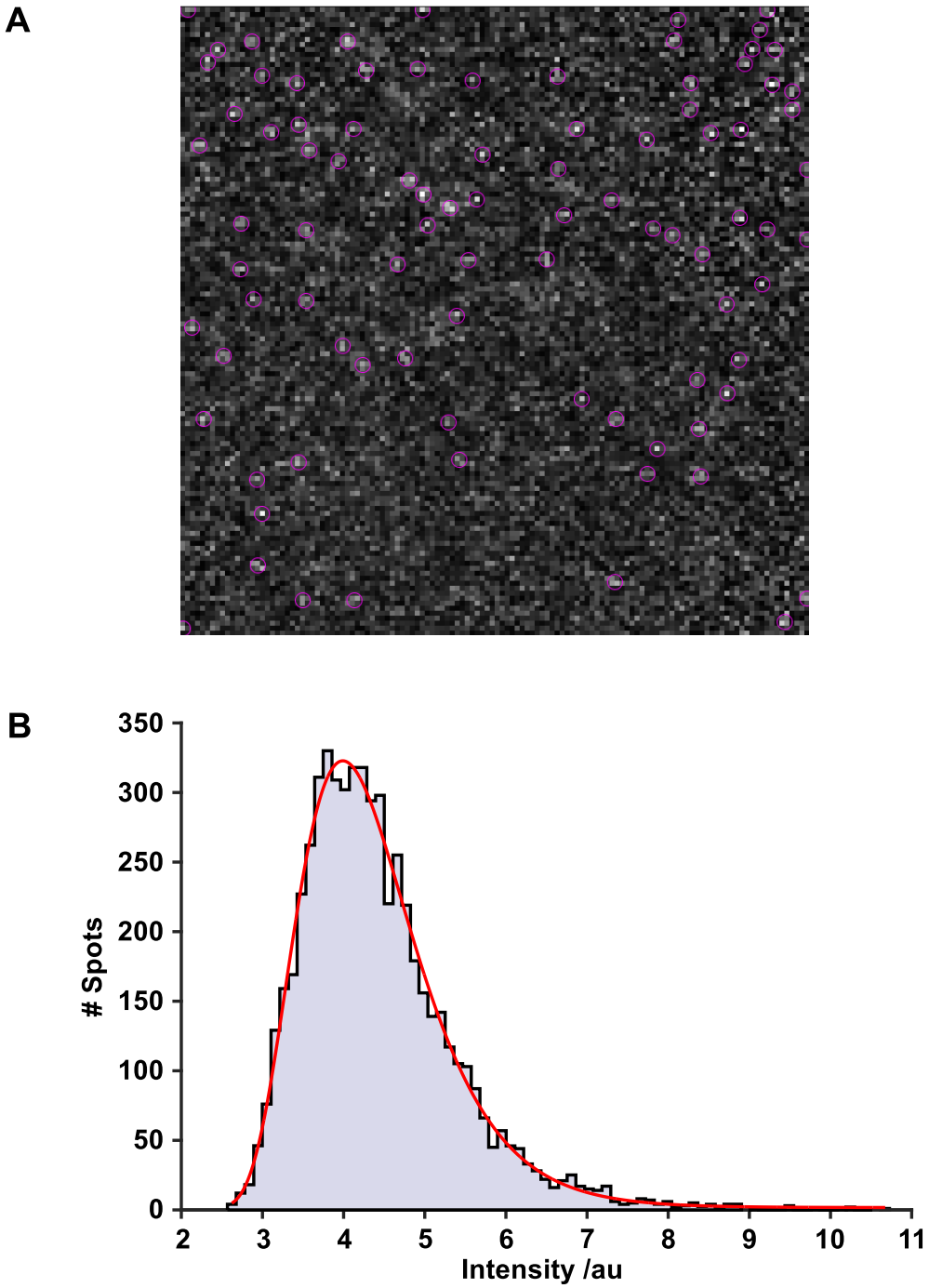


Figure 5.4: Estimating single-fluorophore intensity by tracking single labelled monomers. *A*, Single labelled monomers diffusing on a bilayer before enough were bound to initiate oligomerisation. This frame is from the video in Figure 4.2A. The SNR is low because of low laser power (0.06 mW), which allowed complexes to be resolved but avoided photobleaching, hence some monomers were not detected. The monomers were tracked and marked with purple circles using TrackMate. The variation in intensity of the spots comes from pixel noise, which also caused some bright pixels to be detected as spots. The 'quality' parameter in TrackMate, which reflects SNR, was used to filter out the spurious spots, and those that were retained were confirmed by eye to be monomers by examining their diffusion. *B*, A histogram of maximum pixel intensities from the detected monomer spots in a 50-frame window (one of the frames is shown in *A*) preceding significant assembly in the video from Figure 4.2A. The histogram was fitted with a log-normal function and the position of the peak was used as the value of intensity for a single fluorophore. Using the fitted amplitude of a bounded Gaussian instead of maximum pixel intensity yielded a similar distribution.

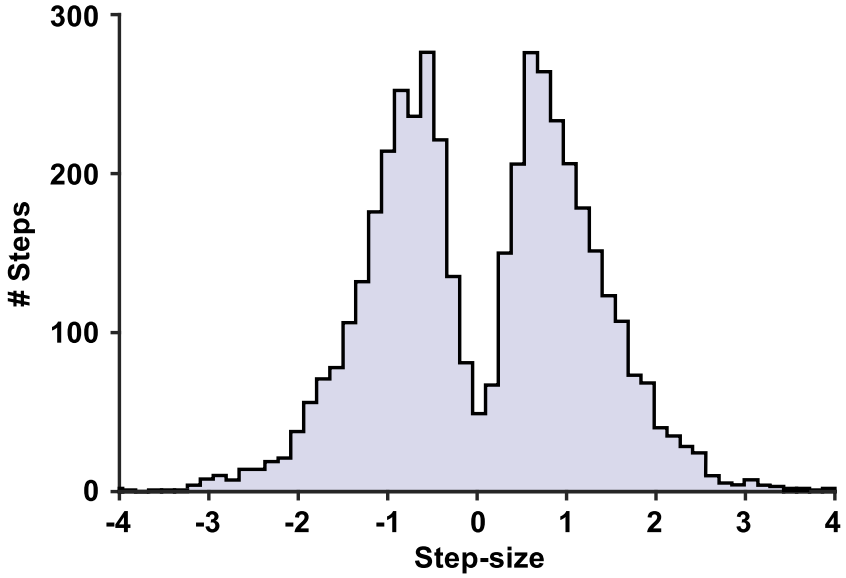


Figure 5.5: Common step-size in assembly traces validates single-fluorophore intensity estimate. A histogram of step-sizes after applying a step-finding algorithm to individual assembly traces (Figure 5.8). Raw intensities were divided by the single-fluorophore intensity, so a step-size of 1 indicates a single labelled monomer causing a step-change in the intensity of a complex. The medians of the two peaks in the histogram are ± 0.9 'single-fluorophore intensities'. To avoid false steps from a lack of time points, the assembly traces were filtered to be over 6 seconds in duration.

5.3.3 Verification by steps in assembly traces

After the calibration of intensity to stoichiometry based on the single-fluorophore intensity of 3 a.u. derived in Section 5.3.2, a step-finding algorithm (discussed in Section 5.4.3) was applied to traces of stoichiometry over time for assembling complexes ('assembly traces'), and also to background regions, and found steps corresponding to single monomers. This finding further validated the 3 a.u. estimate for single-fluorophore intensity. A histogram of the step-sizes is shown in Figure 5.5.

The step-sizes in Figure 5.5 are in units of 'single-fluorophore intensities': the raw intensities of spots were divided by the single-fluorophore intensity 3 a.u. derived in Section 5.3.2, but not multiplied by the labelling ratio. A median step-size of ± 1 would therefore suggest that single labelled monomers were the most common cause of positive and negative steps in the assembly traces, and would justify the 3 a.u. value for single-fluorophore intensity. The actual median step-size derived from the histogram in Figure 5.5 was ± 0.9 'single-fluorophore intensities', approximately validating the 3 a.u. estimate. The physical mechanism behind these positive and

negative steps is discussed in Section 5.5.

In summary, the 3 a.u. value for single-fluorophore intensity provided stoichiometry estimates that agreed with the known stoichiometry of PFO, and that were approximately supported by both the photobleaching analysis and the most common step-size from the step-finding algorithm. This value was therefore used in further analysis, along with the labelling ratio, to calibrate raw intensity to stoichiometry for assembling complexes.

5.4 Assembly and diffusion of individual CDC complexes

5.4.1 Individual stoichiometry traces

In Section 5.3, the intensity of individual assembling complexes was calibrated with stoichiometry using the ratio of labelled to unlabelled protein and the intensity of a single fluorophore. Section 5.1 described the tracking of individual complexes. Combining these efforts revealed the time-dependent stoichiometry of individual assembling CDC complexes.

Figure 5.6 examines the assembly of four representative complexes that were selected from Figure 4.2A. The same complexes were tracked in Figure 5.2. The four columns in Figure 5.6 correspond to the four individual complexes. The tracks in Figure 5.6A show that the complexes diffuse, but Figure 5.6B, which shows the time-dependent change in intensity of these complexes, centres each image at the location of the fluorescent spot. The diffusion of individual complexes is discussed in Section 5.4.2.

Assembling complexes, once resolvable above the background monomer population, appeared to persist and grow larger over time; no clear examples of complexes that grew to a significant stoichiometry and subsequently disassembled

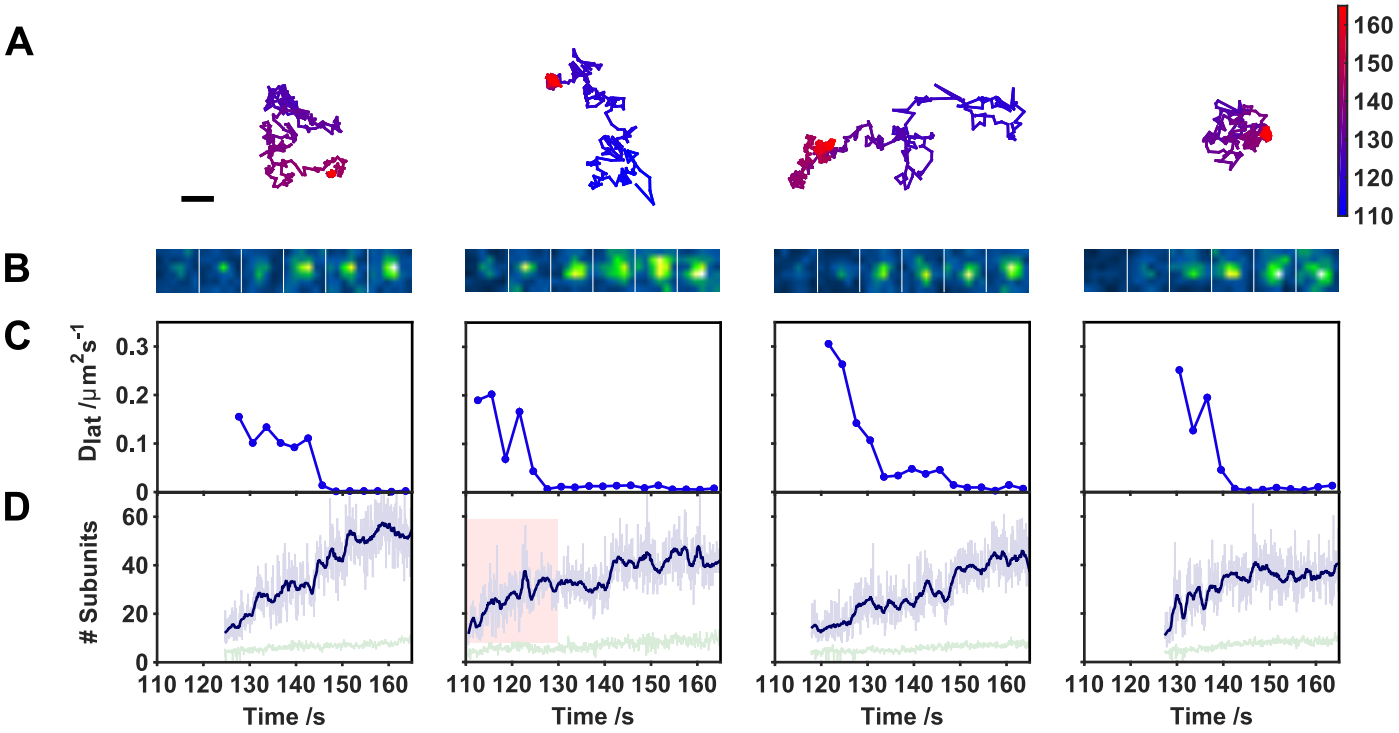


Figure 5.6: Assembly and diffusion of individual CDC complexes. Each column represents a different protein complex, from the video in Figure 4.2A. *A*, The coordinates of the complex over time, as reported by TrackMate (Figure 5.2, redrawn here to compare with other properties of the complexes). Colour bar indicates time in seconds since injection of protein into the 138 nl droplet. Scale bar 1 μm. *B*, The appearance of the complex at 110, 120...160 seconds after injection of protein into the 138 nl droplet, with re-centring in each frame. Some of the spots appear asymmetrical, which is caused by the complex not being positioned at the centre of a pixel, by the brightness and contrast settings causing some pixels with different amplitudes to appear the same colour, and by the fluctuating background signal caused by diffusing monomers and pixel noise. *C*, Time-dependent diffusion of the complex, calculated from the coordinates displayed in *A*. *D*, Stoichiometry of the complex, calibrated in Section 5.3. Light blue: raw data; dark blue: running average, calculated using the smooth function in Matlab (Savitzky-Golay filter, span = 21 frames, 1.26 seconds). The offset of the fitted Gaussian function (Section 5.2), the effective background signal, was also calibrated to stoichiometry and is included in these plots in green. The red highlighted section is used in Figure 5.8.

were found. Figure 5.6D demonstrates that oligomerisation was overall monotonic, but that fluctuations were present in the assembly traces. The implications of these fluctuations for the mechanism of assembly is discussed in Section 5.5; they could either be caused by reversible assembly of the complex or simply by labelled monomers diffusing in the vicinity of the complex but not interacting with it.

5.4.2 Diffusion of assembling CDC complexes

Figure 5.6C shows that a single average diffusion coefficient for assembling complexes would be misleading. The diffusion coefficient for the individual complexes changed significantly over time. The average monomer diffusion coefficient of 1.5 $\mu m^2 s^{-1}$ was reported in Section 4.3.1. For complexes, time-dependent lateral diffusion coefficients $D_{\mathrm{lat}}(t)$ were calculated at 3 second (50 frame) intervals.

For each interval within a track of a diffusing complex, $D_{\mathrm{lat}}(t)$ was calculated as follows. The mean squared displacement (MSD) for every consecutive, non-overlapping sub-track of length 1 frame was calculated and the average taken, $\langle \mathrm{MSD} \rangle_1$. The MSD for every consecutive, non-overlapping sub-track of length 2 was calculated and the average taken, $\langle \mathrm{MSD} \rangle_2$, and so on up to $\langle \mathrm{MSD} \rangle_{10}$ (not more than 20 % of the length of the time interval in frames, to ensure at least 5 separate MSD values were used to calculate a more reliable average).

The average MSDs were plotted against their respective sub-track lengths, after converting pixels to μm and frames to seconds, and fitted with a straight line through zero by minimising the squared residuals. According to $\langle r^2 \rangle = 4Dt$, the gradient of the line was divided by 4 to obtain the average diffusion coefficient for the 3 second interval. The MSD plots were generally well-captured by a linear trend, suggesting Brownian diffusion ($\langle r^2 \rangle = 4Dt$) was a reasonable assumption for diffusing complexes.

Assembling complexes showed a marked decrease in diffusion coefficient over time, exemplified in Figure 5.6C. The decrease in diffusion coefficient generally correlated with an increase in stoichiometry. Often the diffusivity of large complexes experienced a rapid stepwise drop, which could be explained by a part of the complex inserting into the bilayer; membrane spanning regions could cause a complex to become immobile by interacting with the underlying hydrogel, particularly when the hydrogel was dehydrated (as exploited previously [101]). Furthermore, the approach of the diffusion coefficient to zero often coincided with a plateau in the

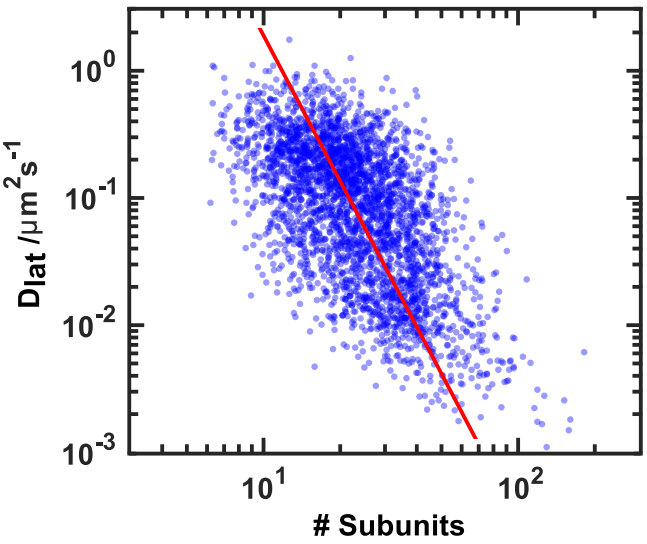


Figure 5.7: Negative correlation between diffusion and stoichiometry. The diffusion coefficient at 1.2 second intervals for over 500 tracks (all tracks greater than 1.2 seconds in duration) was plotted against average stoichiometry at the corresponding time point. The shorter time intervals in this plot, relative to Figure 5.6C, provided more data points but each data point had a higher error. The gradient of the approximately linear trend on the log-log plot, fitted by orthogonal least-squares, was -3.8.

stoichiometry of the complex, consistent with ring closure or insertion (though as discussed in Section 4.2.3, few insertions were detected by electrophysiology relative to the number of assembled complexes detected by smTIRF).

The relationship between diffusion and stoichiometry was further examined by plotting $D_{\text{lat}}(t)$ against stoichiometry for 1.2 second intervals in every track. Figure 5.7 illustrates the result on log-log axes. The data was fitted with a straight line using an orthogonal least squares method in Matlab, which revealed a gradient of approximately -3.8, suggesting that $D_{\text{lat}} \propto \text{Stoichiometry}^{-3.8}$. Orthogonal least squares was appropriate because the variables of both axes were subject to error (unlike plots where one axis was time, for example). A more detailed model of diffusion would be necessary to explain this particular power-law relationship, but the negative correlation between stoichiometry and diffusion is evident in Figure 5.7. Overall, diffusion coefficients for monomers and complexes were consistent with diffusing proteins [124, 125].

5.4.3 Resolving steps in assembly

A detailed inspection of the assembly traces represented in Figure 5.6D revealed step-like features: putatively labelled monomers, by some mechanism, adding and subtracting from the measured intensity of the tracked complex. A step-finding algorithm created by researchers at the University of North Carolina at Chapel Hill was applied to the assembly traces (Credit: 'CISMM at UNC-CH, supported by the NIH NIBIB (NIH 5-P41-RR02170)') . The algorithm convolved a derivative-of-Gaussian kernel with the raw data to produce maxima or minima as appropriate at the step edges [138]. Some example track segments with the identified steps overlaid are presented in Figure 5.8.

Figure 5.8 shows that some segments of the assembly traces were well-captured by the step-finding algorithm, while others were not. Theoretically, the minimum possible step-size in the assembly traces was 6.5, because 6.5 monomers were represented by a single fluorophore due to the unlabelled protein fraction. A histogram of the step-sizes was used to validate the estimated single-fluorophore intensity in Figure 5.5: the median step-size approximately corresponded to a single labelled monomer.

The spots corresponding to complexes were an order of magnitude larger in diameter than the complexes themselves (Section 4.1), so there was ample room for many labelled monomers to diffuse in the vicinity of a tracked complex and contribute to its apparent intensity, without necessarily interacting with it. Labelled monomers diffusing nearby were a possible source of the up- and down-steps in the assembly traces, rather than reversible assembly (see Section 5.5 for further discussion). However, the appearance of protein complexes on the bilayer over time (Figure 4.2) confirmed that at least some of the observed upwards steps were caused by labelled monomers joining a growing complex by oligomerisation.

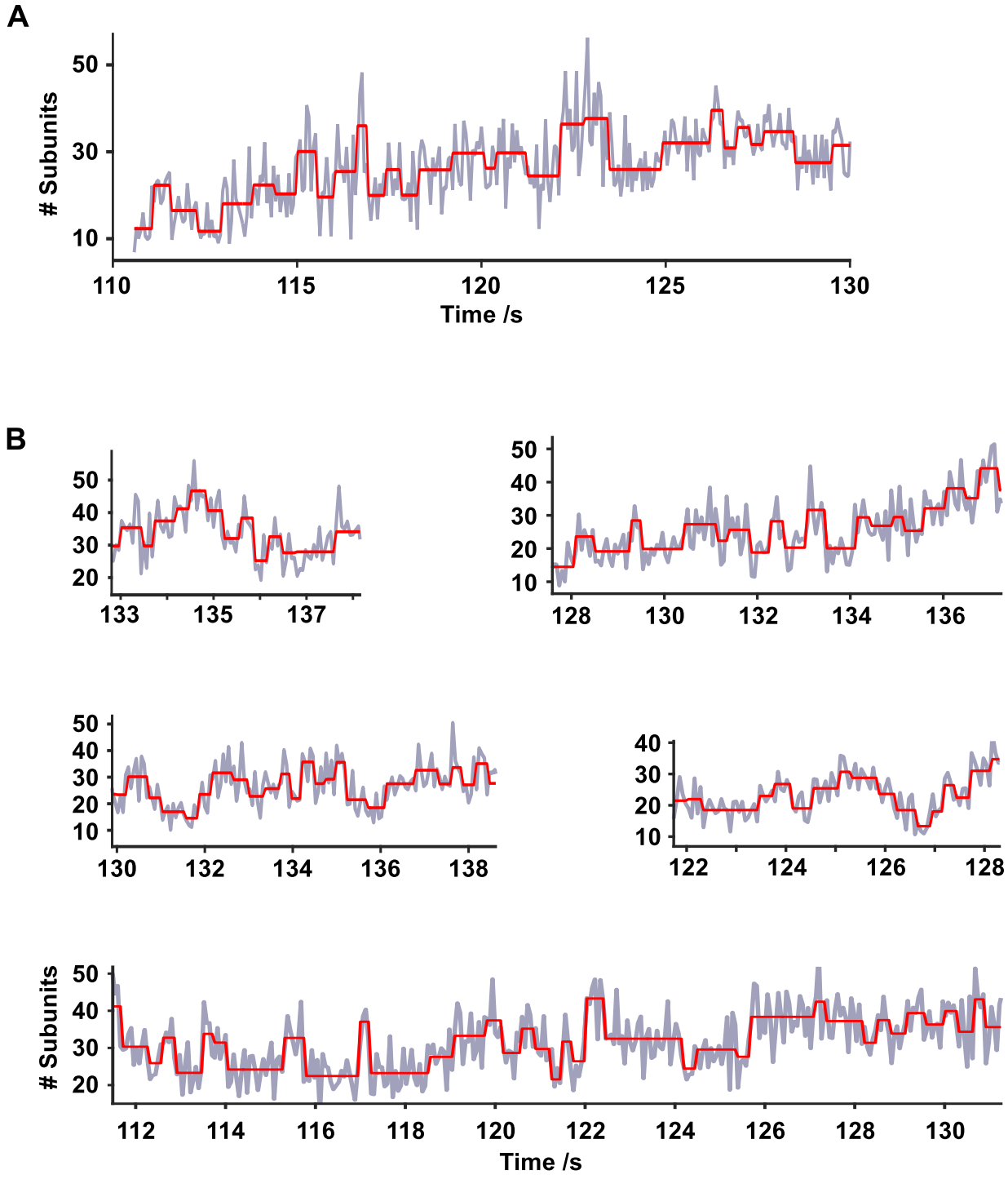


Figure 5.8: Detecting steps in individual assembly traces. A step-finding algorithm based on a convolution of a derivative-of-Gaussian kernel with the raw data highlighted step-like features in the assembly of individual complexes (Credit: 'CISMM at UNC-CH, supported by the NIH NIBIB (NIH 5-P41-RR02170)') [138]. Given the appearance of complexes in assembly videos, at least some of the up-steps in these traces must be due to labelled monomers joining the tracked complex. *A*, The red-highlighted region from Figure 5.6D, second column, rescaled and overlaid with the identified steps. *B*, Example segments from several other assembly traces. 6.5 monomers were represented by 1 fluorophore in smTIRF images of rPFO/lPFO, so 6.5 is theoretically the minimum possible step-size in these traces.

5.5 Assembly mechanism

The assembly traces illustrated in Figure 5.6 were a convolution of the assembling complex and any labelled monomers or small oligomers diffusing on the bilayer within approximately 0.84 μm of the position of the complex ($3\bar{\sigma}$ from the Gaussian fit, Figure 5.10). This section attempts to understand the mechanism of assembly by deconstructing these contributions and thereby determining the source of the fluctuations in assembly traces. The two key mechanisms to discriminate between were reversible and irreversible assembly: the source of fluctuations in assembly traces had to be attributed to either reversible assembly or to diffusing monomers or small oligomers in the vicinity of the tracked complex.

5.5.1 Noise from fluorophores accounts for fluctuations in assembly

To analyse the source of the fluctuations in assembly, the standard deviation of the stoichiometry (σ_{stoich}) in individual assembly traces was calculated at 1.2 second intervals and plotted against the corresponding average stoichiometry for the 1.2 second interval. A complex with many monomers, and therefore many fluorophores, was expected to have a high σ_{stoich}, as the noise from each fluorophore accumulates. This is observed in the overall trend in Figure 5.9.

Furthermore, any extra source of noise or fluctuations on a different timescale, such as reversible assembly, would increase σ_{stoich} for a complex, beyond that caused by random diffusion of monomers and fluorophore noise. Comparing two regions, one with an assembling complex and one with a similar number of separate non-interacting monomers, σ_{stoich} would be the same in the case of irreversible assembly, but would be displaced higher for the region containing the complex in the case of reversible assembly.

As a standard against which to compare, the relationship between σ_{stoich} and

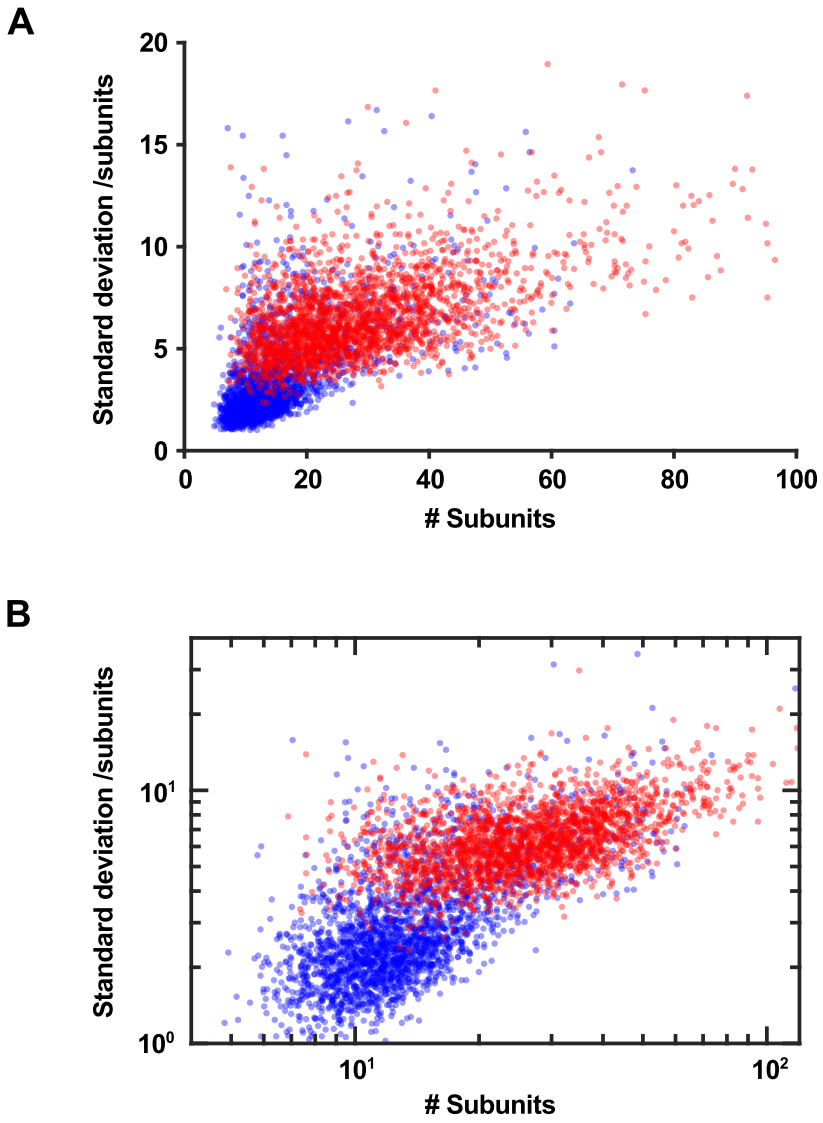


Figure 5.9: Fluctuations in assembly are explained by noise from a greater number of fluorophores. *A*, Standard deviation of the stoichiometry was calculated for 1.2 second intervals for all the individual assembly traces and plotted against the corresponding average stoichiometry for the interval. As expected, standard deviation is proportional to stoichiometry, because more fluorophores cause more noise in the intensity of a spot. If reversible assembly were present, the standard deviation for complexes (red) would potentially be displaced higher from that for a random position on the bilayer (effectively the background, blue). Instead, the relationship for complexes appears as a continuation of the relationship for random positions, at least within the sensitivity of this analysis. To ensure tracks were long enough for a time-dependent standard deviation to be relevant, tracks were filtered to be over 6 seconds in duration. *B*, Equivalent plot to *A* on a log-log scale to highlight the trend.

stoichiometry was calculated for the background signal. Effective background 'stoichiometry' values were obtained as follows: for each time-point in each assembly trace, the maximum intensity of a 5×5 grid displaced 8 pixels from the tracked complex was recorded, and this intensity calibrated in the normal way

to stoichiometry. If complexes assembled irreversibly, such that all fluctuations were caused by diffusing monomers or noise from fluorophores, then the relationship between σ_{stoich} and stoichiometry for complexes would be expected to map onto the same relationship for the background signal. If complexes assembled reversibly, such that there was an extra source of fluctuations on a potentially different timescale, σ_{stoich} would be expected to be displaced higher than the corresponding values for background.

As illustrated in Figure 5.9, no such displacement was evident. Rather, the relationship between σ_{stoich} and stoichiometry appeared to continue smoothly from diffusing monomers (effective background, blue) to tracked complexes (red). However, it may be that reversible assembly created an effect on the σ_{stoich}-stoichiometry relationship that was too small to detect in this analysis.

5.5.2 Timescale of fluctuations in assembly matches monomer diffusion

The step-finding algorithm from Section 5.4.3 was exploited to determine the lag time between fluctuations. The step-finder characterised the fluctuations in terms of up-steps and down-steps and it was trivial to extract the time-delays in between. The lag times between steps were compared with the time expected for labelled monomers to diffuse across a region of interest encompassing the area of the tracked spot. A distance of $R_\sigma = 6\bar{\sigma}$, 6 times the median standard deviation of all Gaussian-fitted spots, was used as the diffusion distance. Elsewhere in the thesis, the stated spatial resolution of 550 nm in sm-fluorescence experiments equates to approximately $2\bar{\sigma}$, the separation at which spots were individually resolvable. A histogram of standard deviation values from all fitted spots is shown in Figure 5.10A - spikes are present at either end of the histogram because the permitted values of the fitted parameter were bounded.

Figure 5.10B shows a histogram of lag times taken for single labelled monomers

to cross a distance of R_σ. An example frame from the video of tracked single monomers is also shown. Figure 5.10C shows an equivalent plot and frame, but for single labelled monomers with intact fluorescence after a photobleaching experiment; prior to photobleaching, complexes could be resolved on the bilayer. Figure 5.10C demonstrates the diffusion time to cross R_σ at a protein concentration sufficient for oligomerisation to occur, a concentration more similar to the assembly videos from Figure 4.2 than the sparse single monomers in Figure 5.10B, in case 2D monomer density affected the lag times.

Figure 5.10D shows a histogram of all lag times between consecutive steps in the assembly traces, up or down, as reported by the step-finding algorithm (Figure 5.8). Evidently the timescale for diffusion of monomers across R_σ, highlighted in Figures 5.10B and C, was essentially equal to the timescale for consecutive steps in the assembly traces. The equal lag times do not conclusively show that the fluctuations in assembly traces must be due to diffusing monomers, but that diffusing monomers (or small oligomers), rather than reversible assembly, are a likely cause of the fluctuations. Similar to the previous analysis in this section, however, it is possible that the dissociation of monomers by reversible assembly was also on the same timescale as monomer diffusion, and was contributing to the fluctuations.

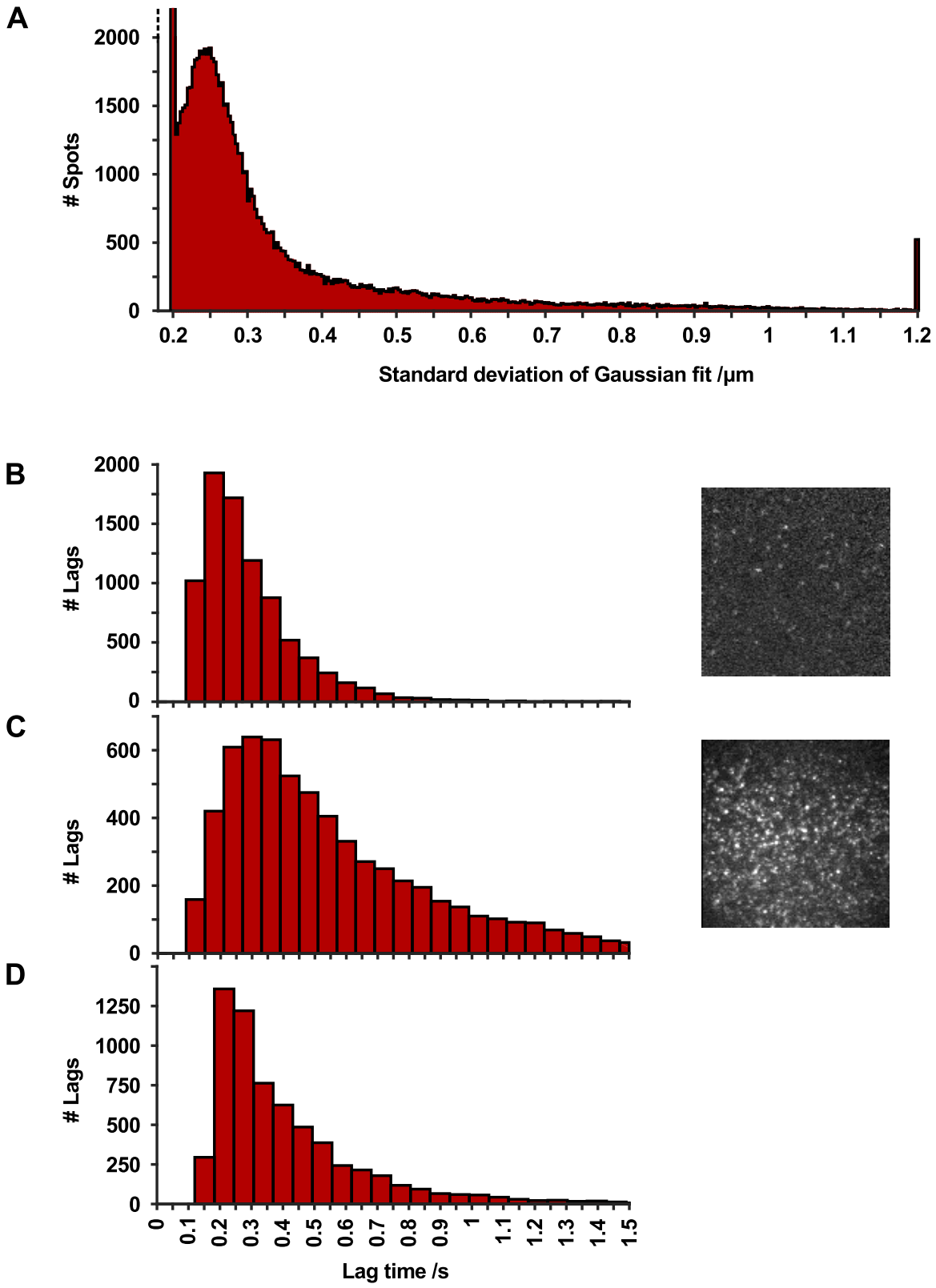

A
Spots
2000
1500
1000
500
0
0.2
0.3
0.4
0.5
0.6
0.7
0.8
0.9
1
1.1
1.2
Standard deviation of Gaussian fit /µm
B
Lags
2000
1500
1000
500
0
C
Lags
600
400
200
0
D
Lags
1250
1000
750
500
250
0
0
0.1
0.2
0.3
0.4
0.5
0.6
0.7
0.8
0.9
1
1.1
1.2
1.3
1.4
1.5
Lag time /s

Figure 5.10: Lag time for steps in assembly traces matches monomer diffusion. *A*, A histogram of standard deviations, σ from Equation 5.1, of the fitted Gaussian functions from every spot of every track. The median standard deviation, $\bar{\sigma} = 0.28$ μm, was multiplied by 6, as $\pm 3\sigma$ contains 99.7 % of the area under a Gaussian function. This provided a diffusion distance, $R_\sigma = 1.68$ μm. *B*, A histogram of all the lag times taken for single molecules at low density to diffuse across R_σ. A frame from the tracked video, the same video as Figure 4.3, is shown for reference. *C*, A histogram of all the lag times taken for single molecules at a more relevant density, tracked after the photobleaching of complexes, to cross R_σ. *D*, A histogram of all the lag times between consecutive steps identified in assembly traces (Figure 5.8). The lag times between steps closely correspond to the time taken for single monomers and small oligomers to diffuse across the area of a tracked complex, represented by R_σ. To avoid artifactual lag times from short tracks, tracks were filtered to be over 6 seconds in duration.

In summary, the analysis presented so far in this section suggests the fluctuations in assembly traces could be entirely and accurately explained by single labelled monomers and small oligomers diffusing in the vicinity of the tracked complexes. An irreversible stepwise monomer-addition mechanism of assembly for PFO is expected based on the size of the pore (Section 6.2.2), and has been suggested by others [25, 49], and the fluctuations observed in assembly traces in Figure 5.6 do not contradict this theory, as demonstrated in this section.

5.5.3 Oligomer-based assembly

Assembly of PFO rings by the addition of small oligomeric complexes (dimers and trimers, for example) could be missed in these experiments due to the unlabelled fraction of protein. However, it is unlikely that small oligomer addition contributed significantly to the assembly of complexes because the oligomers are a small minority relative to the large population of monomers: an oligomer is always more likely to encounter a monomer than another oligomer, and as discussed in Section 5.6.3, only a small fraction of collisions are successful.

A second oligomer-oligomer assembly mechanism is the joining of arcs to make irregular protein complexes, as discussed in Section 4.3.4. These irregular complexes have been repeatedly observed in AFM and EM studies (Figures 1.9C [27] and 1.8D [25], for example). This mechanism does not lead to regular ring-shaped pores, but is still relevant as it leads to functional pore-forming complexes, sometimes

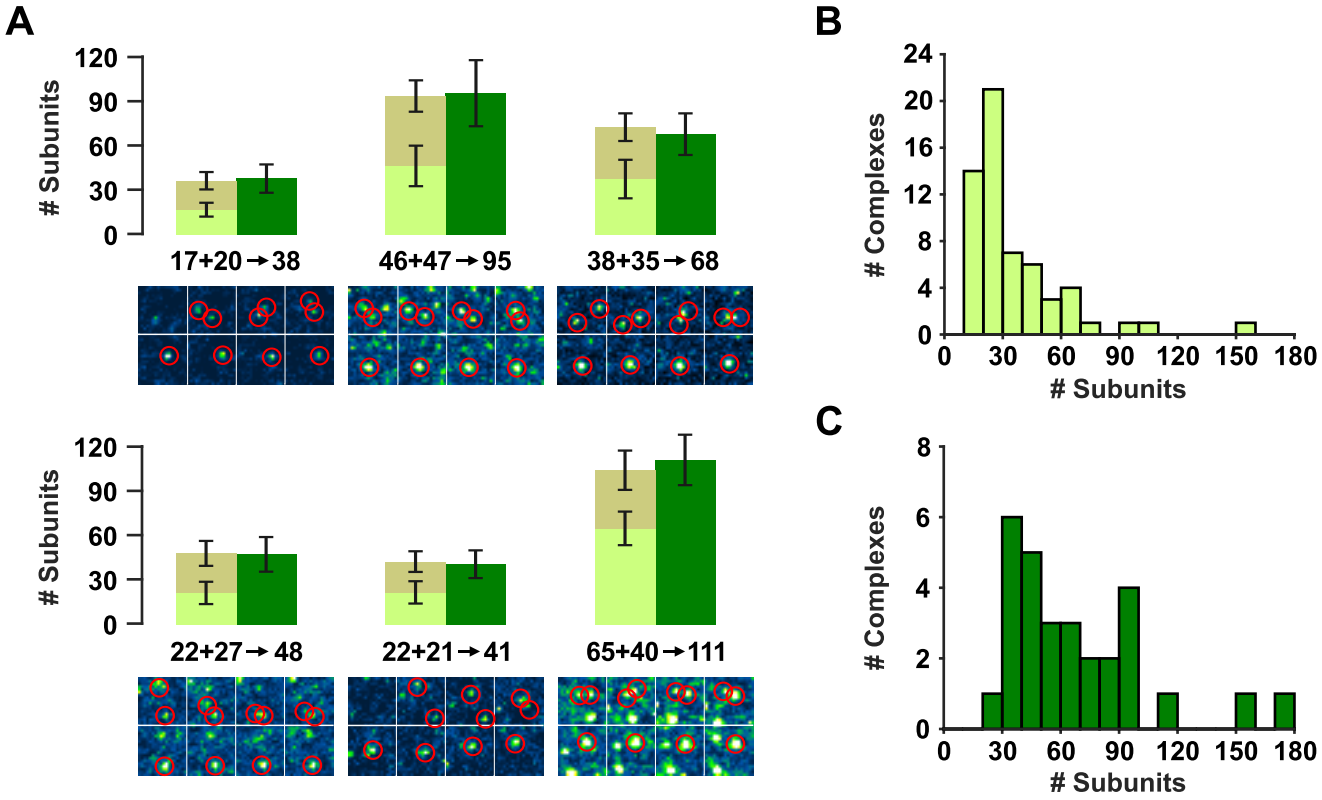


Figure 5.11: Quantitative oligomer-oligomer assembly. *A*, Complexes that were partially formed were observed binding together to form larger complexes; 30 such events were analysed for their stoichiometries, before (light green/brown) and after (dark green) the binding event. The 6 individual examples presented here were introduced in Figure 4.8. The stoichiometries are averages calculated from the 50 frames before and after the merging event. The complexes that bind and the resulting complexes are highlighted in the montages below, the frames displayed being taken at -10, -5, -2.5, -1.25, 0, 1.25, 2.5 and 5 seconds relative to the binding event. *B*, Histogram of complex stoichiometries before the binding event, median = 26. *C*, Histogram of complex stoichiometries after the binding event, median = 58.

causing larger membrane lesions than those of a regular shaped pore, and highlights the adaptability of CDC proteins [25, 27].

Figure 4.8 presented putative examples of arcs binding together, observed by smTIRF. After calibrating intensity with stoichiometry in Section 5.3, the stoichiometries of the multi-subunit complexes involved in this mechanism were quantified, as exemplified in Figure 5.11A. The output stoichiometries match the sum of the input stoichiometries to within error.

Histograms for the input and output stoichiometries of complexes are presented in Figure 5.11B and 5.11C respectively. The median input stoichiometry was 26, the median output stoichiometry was 58. The histograms suggest that there was a

typical size at which the complexes encountered each other, potentially caused by a simple characteristic collision frequency, or a consistent point at which the local monomer concentration was insufficient for ring completion. The most common instances were of two putative arcs joining to form a complex similar in stoichiometry to a typical PFO ring, but slightly higher.

In total, 30 of these binding events were identified (30 input data points, 15 output); the process is not yet automated, but it was difficult to find more of these events by eye. The total number of tracked complexes in this analysis that started below 20 subunits (filtered to ensure early assembly was included) yet reached over 26 subunits (the median of the input stoichiometries) was over 500. It seems likely, therefore, that this mode of assembly was an off-pathway bonus feature related to the CDCs' ability to form pores from arc complexes, but was not the principal mechanism for assembly.

The remodelling of LLO in Figure 1.9, with arcs able to accommodate other arcs and subsequently form a ring, may also provide an explanation for traces observed in this study where assembly seemed to continue after putative membrane insertion (some complexes appeared to grow brighter after becoming immobile). However, others have commented that oligomerisation occurs entirely before membrane penetration [25]. An opposing argument might be that the plastic nature of LLO was related to its pH sensitivity [27], but Nelson et al. have also shown that PFO exhibits pH sensitivity [117].

5.6 Dissecting CDC assembly kinetics

Building on the previous analysis in this chapter, this section investigates the kinetics of PFO assembly. Assembly is quantified for a single complex and a population of complexes.

5.6.1 Rate of complex appearance

To determine the approximate timescale for assembly of PFO, the number of complexes in a field of view was plotted over time; Figure 5.12 displays this result for the three assembly recordings in Figure 4.2. The number of detected spots represents the number of complexes within a frame, because the tracking parameters used here did not include monomer tracking (the parameters are listed in Section 5.1). After the protein sample was injected, the number of complexes followed a sigmoidal trend over time, but with an apparently linear increase after the inflexion point rather than a plateau. The initial lag-phase was presumably caused by the 2D monomer population increasing to a threshold density at which the encounter frequency was sufficient for oligomerisation.

The average intensity of the bilayer in the field of view increased linearly with time throughout the assembly videos, suggesting that labelled monomers were continuously binding to the bilayer at a constant rate. This observation explains the linear increase in the number of complexes at longer timescales in Figure 5.12. The overall sigmoidal trend is characteristic of the kinetics of pore formation [13, 14].

A rate constant was difficult to interpret for the assembly of complexes because monomers were continuously binding to the bilayer over the course of assembly. An attempt is made in Section 5.6.2. Moreover, Figure 5.12 only plots complexes observed in the field of view; other complexes on the bilayer and also any monomers or complexes bound to the monolayer of the droplet could not be accounted for. Nevertheless, the important timescale to note from Figure 5.12 is the 20 seconds taken for the period of rapid complex formation, and the 40 seconds taken for the rate of complex formation to settle to the steady linear regime. For the purpose of differentiating their relative kinetics, arcs and rings could not be discriminated in this analysis: only an estimate of stoichiometry for each complex was possible.

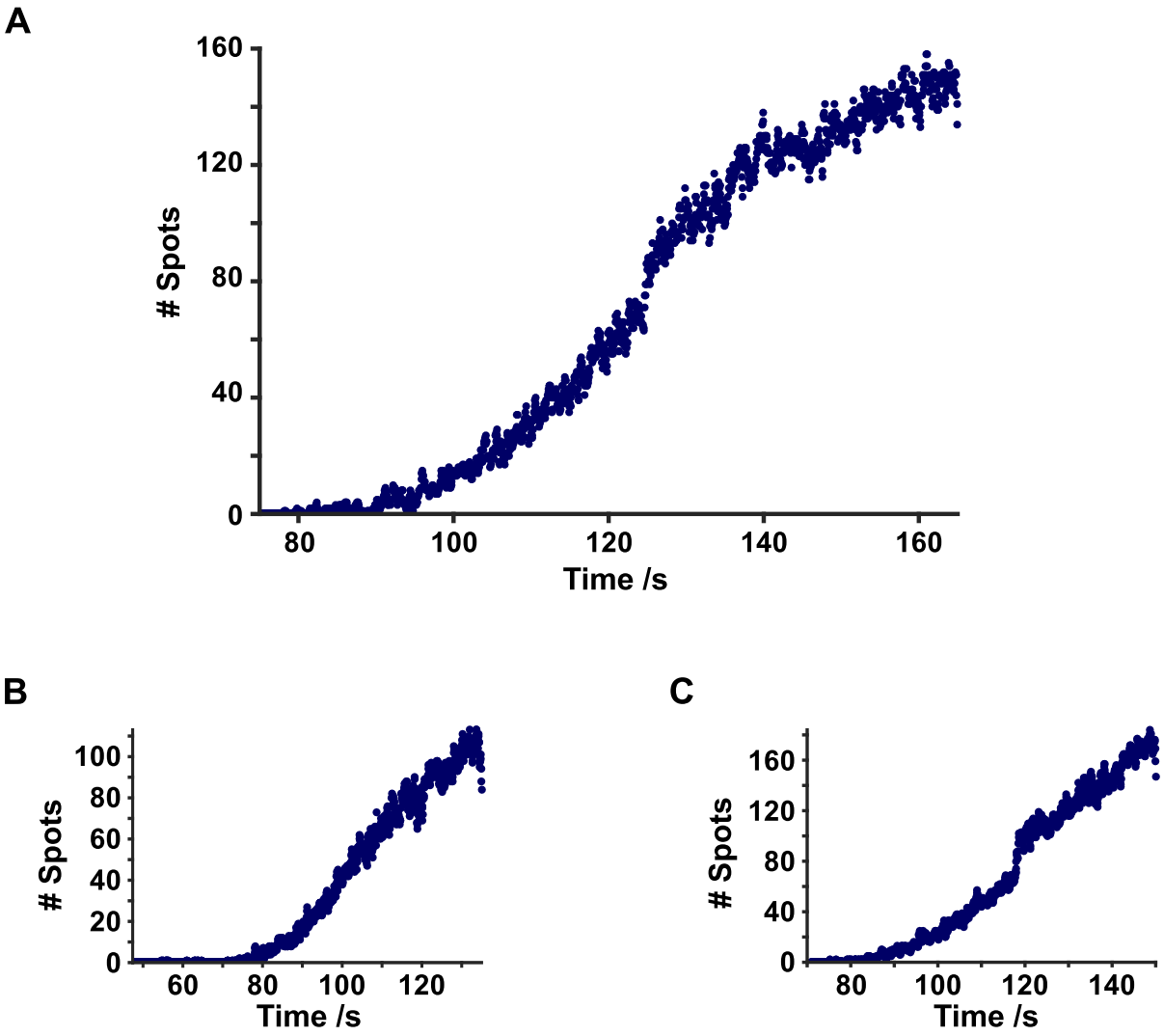


Figure 5.12: Rate of complex appearance. Spots were detected with TrackMate and correspond to PFO complexes: either arcs, complete rings or large irregular complexes. The number of complexes forming over time is one measure of assembly kinetics. *A*, *B* and *C* are equivalent iterations of protein injection and PFO assembly on different bilayers, and correspond to *A*, *B* and *C* in Figure 4.2. One data point = one frame, 0.06 s per frame.

5.6.2 Average rate of assembly for a single PFO complex

A significant benefit of resolving individual complexes was the ability to synchronise the complexes at a point in their assembly without the need for any external chemical modification. This opportunity was exploited to measure the average rate of assembly for a single complex.

Figures 5.13 reports the median assembly rate for the same recordings as Figures 4.2 and 5.12. For each recording of assembly, the individual traces of assembling

complexes' stoichiometry over time were filtered, with those that began under 20 subunits retained, to ensure early assembly was captured. The traces were aligned at their point of first detection, effectively synchronised *in silico*, and plotted together (Figure 5.13, light blue). The median stoichiometry for every time point was calculated (Figure 5.13, dark blue spots). For comparison, the equivalent traces and median for the offset parameter of the Gaussian fitting (c from Equation 5.1), calibrated to stoichiometry, was plotted as a measure of background (Figure 5.13, green). Due to the difficulty in tracking dimmer spots, many low stoichiometry tracks are short: the average stoichiometry was computed from hundreds of tracks at early times, and from a minimum of 8 tracks at the last time point for which it is reported in Figure 5.13.

The median assembly trace, dark blue in Figure 5.13, represents the average rate of assembly for a single PFO complex. A period of rapid growth precedes a slower extension of the complex. In good agreement with the timescale for assembly from the overall rate of complex formation, Figure 5.12, the average complex took around 40 seconds to form, and reached a stoichiometry of around 40 subunits (Figure 5.13A and B).

This timescale was dependent on protein concentration, as illustrated qualitatively in Sections 4.3.1 and 4.3.2, but it was not possible to quantify the dependency with this technique, for reasons discussed in Section 4.3.1. Cholesterol content in the bilayer would also affect the timescale; the cholesterol dependency was not quantified, but the effect of varying cholesterol content would manifest as a variation in 2D protein concentration. The relationship between protein binding and cholesterol content has been characterised previously [10, 117, 118, 139].

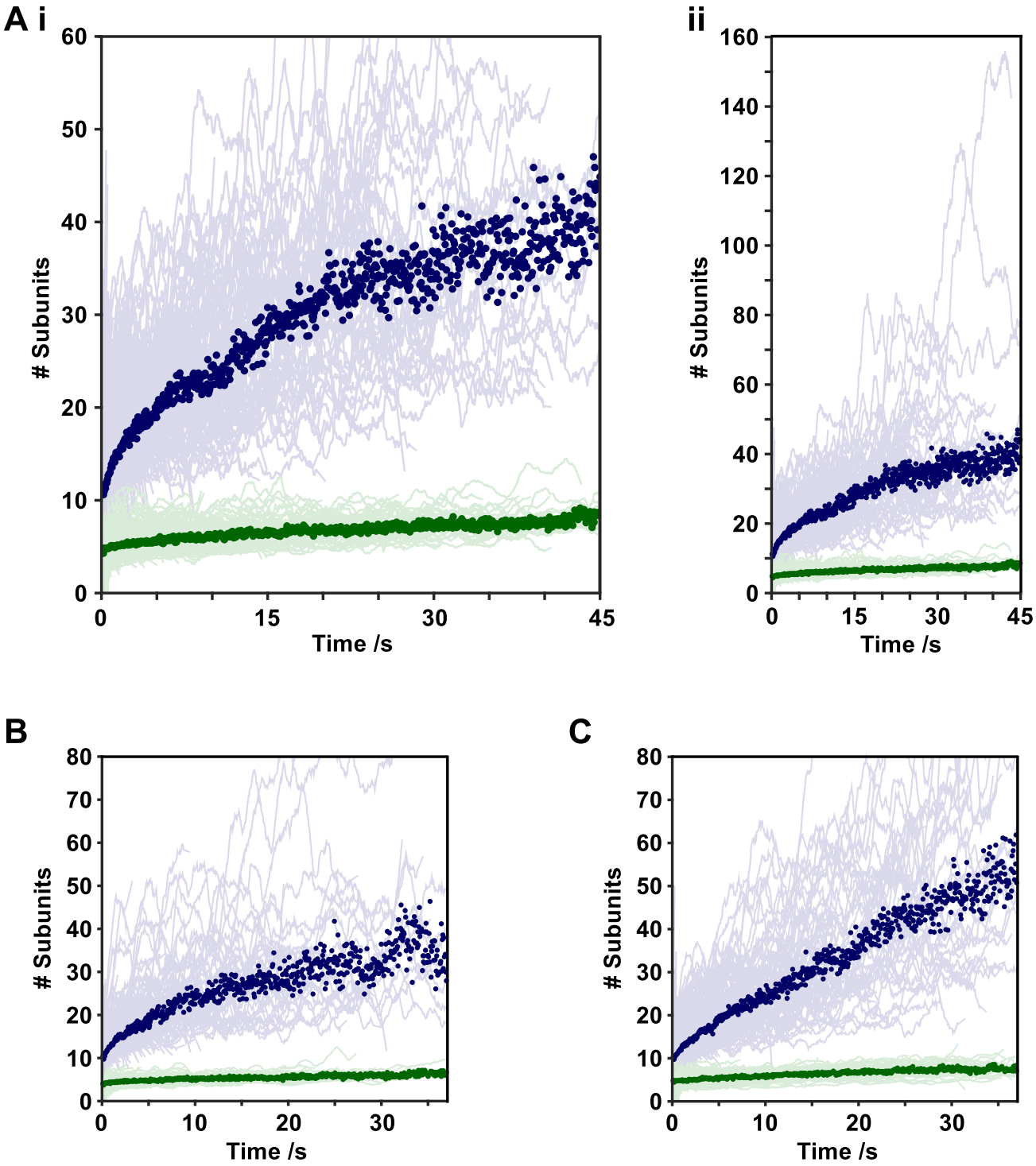

A i
ii
B
C
Subunits
Time /s
0
10
20
30
40
50
60
70
80
100
120
140
160
15
45

Figure 5.13: Average rate of assembly for a single PFO complex. *Ai*, Individual assembly traces aligned at their point of first detection were plotted (light blue) and the median for each time point superposed (dark blue). The traces were filtered to begin below 20 subunits, to more accurately represent early assembly. The equivalent plot for background signal, from the Gaussian fitting offset, c from Equation 5.1, is shown in green. The median was calculated from the raw stoichiometry traces (light blue in Figure 5.6D), but for clarity the aligned tracks in light blue are equivalent to the smoothed stoichiometry trace in dark blue from Figure 5.6D. The minimum detectable stoichiometry was 6.5, because 6.5 monomers were represented by 1 fluorophore via the stoichiometry calibration; for the same reason, the complexes were generally only detected at over 10 subunits (after calibration, or approximately two single-fluorophore intensities). *Aii*, A rescaled version of *Ai* to highlight the maximum stoichiometry of over 100 subunits reached by some complexes. *A*, *B* and *C* are equivalent iterations of protein injection and PFO assembly on different bilayers, and correspond to *A*, *B* and *C* in Figure 4.2.

Figure 5.13Aii is equivalent to 5.13Ai except for the scale. At the reduced scale, the maximum stoichiometry reached by some complexes is revealed. Certain complexes reached an estimated stoichiometry of over 100 subunits. These complexes were generally the result of two or more separate complexes either binding to create a larger irregular complex, as per the mechanism described in Section 5.5.3, or residing in roughly the same location but not necessarily interacting, and subsequently being tracked as a single complex. The bilayer in Figure 5.13C exhibited a relatively high number of such cases, due to a higher 2D protein concentration (Figure 4.2C), which affected the shape of its median assembly curve.

The median assembly curve from Figure 5.13A was fitted with different functions, by minimising the squared residuals, to determine the type of relationship that most accurately captured the dependency of stoichiometry on time (Figure 5.14). The three functions trialled, based on the general shape of the median assembly curve, were a single-exponential, a sigmoid and a double-exponential (green, purple, and red respectively in Figure 5.14). A reduced-χ^2 comparison of the fits proved ineffective as the variance in stoichiometry was not known *a priori*, and the R^2 metric suggested that the fits captured the data equally well (0.9221, 0.9230 and 0.9226 for the single-exponential, sigmoid and double-exponential fits respectively). A visual inspection of the fits, highlighted in the inset in Figure 5.14, suggested that a double-exponential fit (red) potentially captured the early assembly regime most

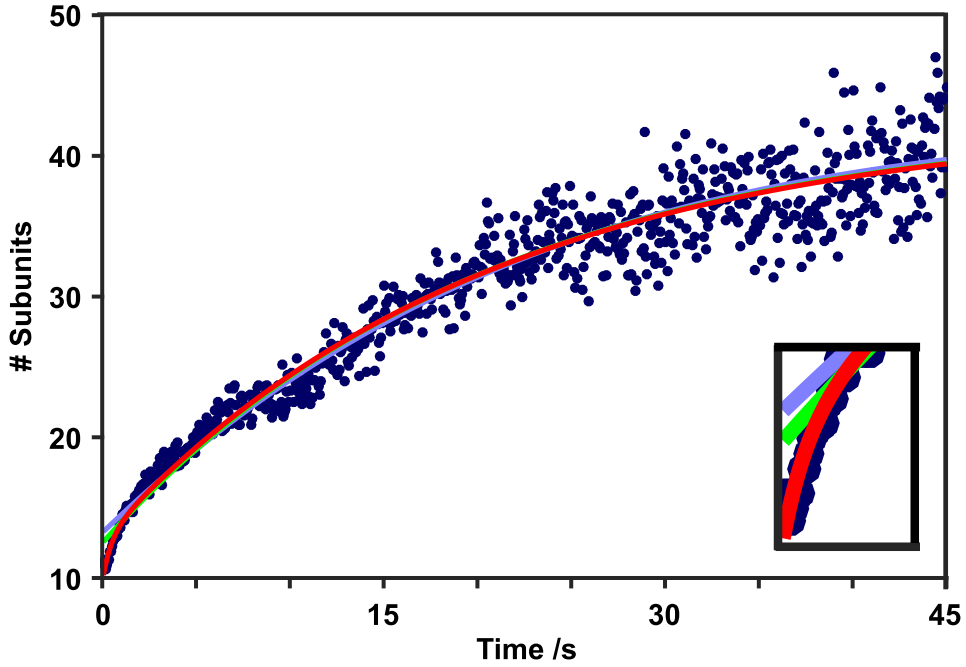


Figure 5.14: Fitting the single-complex median assembly curve. The median assembly curve from Figure 5.13Ai was fitted with single-exponential (green), sigmoid (purple) and double-exponential (red) functions by minimising the squared residuals. Though all fits accurately captured late assembly, the inset starting at 0 s shows that early assembly was potentially captured most accurately by a double-exponential.

accurately.

5.6.3 Monomer and oligomer collision rates

The average rate of assembly for a single complex seemed to exhibit an early period of rapid assembly followed by a slower extension of the complex, and was accurately described by a double-exponential function (Figures 5.13A and 5.14), given in Equation 5.2 with the fitted parameters in bold.

$$f(x) = \boldsymbol{c} - \boldsymbol{A}\exp\left(-\boldsymbol{k_1}(x+\boldsymbol{d})\right) - (\boldsymbol{c}-\boldsymbol{A})\exp\left(-\boldsymbol{k_2}(x+\boldsymbol{d})\right) \tag{5.2}$$

The rates defining the red double-exponential curve in Figure 5.14 were $k_{\text{fast}} = 2.2$ s^{-1} and $k_{\text{slow}} = 0.05$ s^{-1}. Of the two terms describing the fast and slow phases of assembly, the slow dominated with a coefficient of 31, compared to 12 for the fast phase (72 % slow phase, 28 % fast phase). k_{slow} also corroborated the timescale

for the overall rate of complex formation in Figure 5.12A. (k_{slow} was approximately equal to the rate derived for the single-exponential.)

The rate derived from the assembly curve represented successful oligomerisation: the number of successful collisions with monomers for a single complex per second. The number of complexes per area was difficult to estimate because complexes were constantly forming, therefore the time with the highest rate of formation (125 seconds after injection, the inflexion point in Figure 5.12A) was taken as a reference point. At the reference point the density of complexes was 0.03 μm^{-2}. The rate of successful collisions between monomers and complexes was $K_{\text{success}} = 0.03 \times 0.05 = 0.0015\ \mu m^{-2}s^{-1}$.

The total number of collisions between monomers (diffusing quickly) and complexes (diffusing slower) was estimated using Smoluchowski's theory, applied to reactions between a dilute species and static sinks in two dimensions (see Keizer's review [140]). The theory is summarised in Equation 5.3.

$$\begin{aligned} K_{\text{total}} &= \bar{\rho}_{\text{mon}}\bar{\rho}_{\text{complex}} r^{\text{obs}} \\ &= \bar{\rho}_{\text{mon}}\bar{\rho}_{\text{complex}} \left(\frac{2\pi D_{\text{mon}}}{\ln(b/R) - \gamma + \ln(\sqrt{2})} \right) \end{aligned} \tag{5.3}$$

The diffusion coefficient for single monomers, $D_{\text{mon}} = 1.5\ \mu m^2 s^{-1}$, was calculated using the video from Figure 4.3 and custom software created within our research group, based on MSD fitting; the 2D density of complexes, $\bar{\rho}_{\text{complex}} = 0.03\ \mu m^{-2}$, was calculated from the number of complexes at the inflexion point in Figure 5.12A; the 2D density of monomers, $\bar{\rho}_{\text{mon}} = 14\ \mu m^{-2}$, was calculated using the overall intensity of the bilayer (the total amount of bound protein) at the inflexion point, and the stoichiometry calibration; $b \equiv \sqrt{(\pi\bar{\rho}_{\text{mon}})^{-1}}$; the nominal encounter radius within which a collision was deemed to have occurred, $R = 3$ nm, was chosen to roughly match the radius of a PFO monomer [22]; $\gamma = 0.577$ is the Euler-Mascheroni constant. r^{obs} is the rate constant and K_{total} the reaction rate. The total rate of

collisions between monomers and complexes was therefore estimated to be $K_{\text{total}} = 0.60\ \mu m^{-2}s^{-1}$.

Under the experimental conditions for the assembly of PFO in Figure 4.2A, only one in $0.60/0.0015 = 400$ collisions between monomers and complexes were successful and resulted in the growth of a complex. The equivalent result for αHL, that 1 in 10^7 collisions were successful [67], supports the argument for a different assembly mechanism for PFO. Where αHL could assemble reversibly as discussed in Section 6.2.2, PFO is more likely to assemble irreversibly, because far fewer collisions were required for assembly. This finding agrees with the analysis in Section 5.5.

5.6.4 Stoichiometric evolution of a PFO population

Figure 5.13A presented the average rate of assembly for a single complex, for one particular protein population added to a DIB, calculated by aligning assembly traces for individual complexes at their point of first detection. An alternative view of assembly for the *in silico*-synchronised population of PFO is presented in Figure 5.15. A histogram of stoichiometry for the aligned traces (light blue in Figure 5.13A) was made for each 5 second interval in synchronised time (along the x-axis of Figure 5.13A), from 5 to 45 seconds (blue to red, respectively, in Figure 5.15). Figure 5.15 succinctly captures the whole assembly process: starting from a multitude of monomers and proceeding all the way to oligomers of around 30-40 subunits at late synchronised time.

The number of low-stoichiometry complexes and monomers in the first 5 seconds was so high (192×10^2) relative to the later peaks because of the excess of monomers on the bilayer, and because at low stoichiometry the complexes were hard to track, causing an abundance of short-duration, low-stoichiometry tracks at early time in the assembly process. The tracking parameters for this analysis were adjusted to include monomers, to provide a more complete picture of the stoichiometric evolution of the PFO population. The sacrifice for allowing monomer tracking was an increased

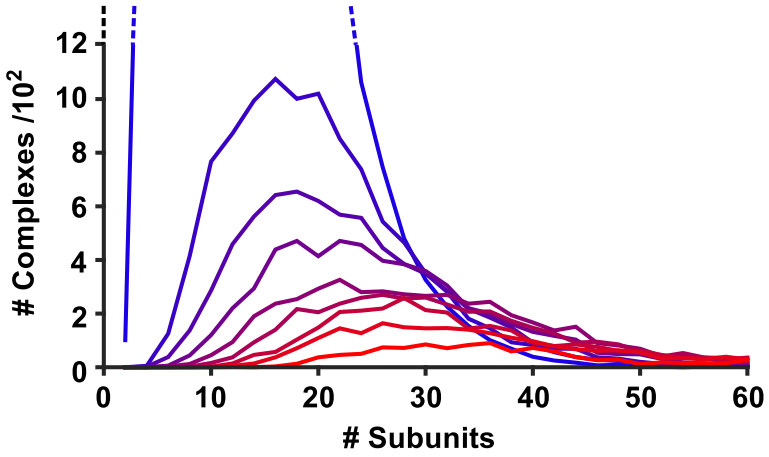


Figure 5.15: Stoichiometric evolution of the *in silico*-synchronised PFO population. Tracking parameters were adjusted to also track monomers (as opposed to complexes only, as in previous figures), tracks were aligned as in Figure 5.13, and histograms of stoichiometry were made for all the spots in a given 5 second interval. Similarly to Figure 5.13, the traces were first filtered to begin below 20 subunits, to more accurately represent early assembly after synchronisation. The time range extends from the first 5 seconds (blue) to 45 seconds (red), along the x-axis of Figure 5.13A. The histogram peaks position shifts over synchronised 'assembly time' due to monomers and small oligomers assembling into larger complexes. The monomer/small oligomer peak in the first 5 seconds reached 192×10^2, the reason for the large value is given in the text. The bins are 2 subunits wide and centred on even stoichiometries. The video of assembly used for this analysis is represented in Figure 4.2A.

likelihood of inaccurate tracks for complexes, but tracking errors were alleviated by representing many tracks in the stoichiometry distribution for each time point in Figure 5.15. (The tracking parameters replaced from Section 5.1 were the following: Threshold = 0.047 a.u., Linking max distance = 3 pixels, Gap-closing max distance = 3 pixels. 1 pixel = 0.4 μm.)

In Figure 5.16, the synchronisation step was removed and a histogram of stoichiometry for all the PFO proteins present on the bilayer was plotted, not relative to the assembly time of an average complex, but every 10 s as the experiment progressed from 85 (blue) to 165 (red) seconds after injection of the protein sample. The time range is equivalent to Figure 5.12A. The monomer peak grew larger with time, representing more monomers binding to the bilayer. The monomer peak also shifted to higher apparent stoichiometry over time, because eventually the labelled monomers were sufficiently dense that more than one was detected within

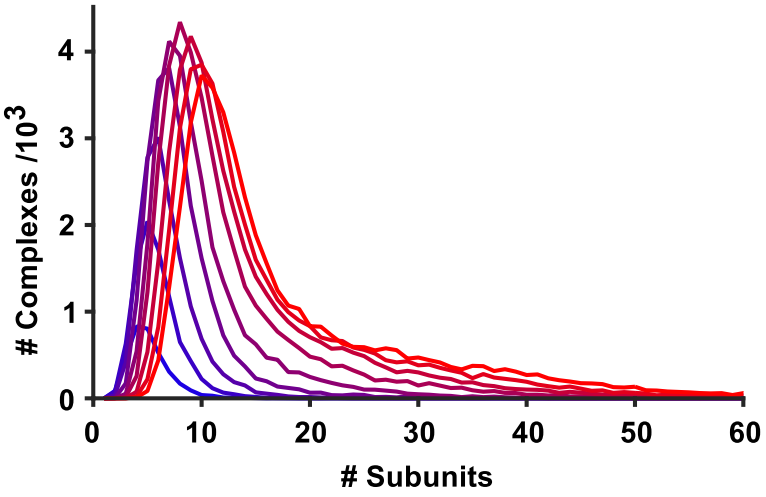


Figure 5.16: Stoichiometric evolution of the PFO population, over real time. Including monomers (see text for new tracking parameters), histograms were made of the distribution of spot sizes over time, without aligning tracks at their start. The time intervals are 10 seconds, from 85 seconds after injection (blue) to 165 seconds (red). The low stoichiometry peak gets larger as more monomers bind to the bilayer, while the extending tail of the distribution captures the formation of larger complexes at later times (see text for details). The bins are 1 subunit wide and centred on integer stoichiometries. The video of assembly used for this analysis is shown in Figure 4.2A.

an 'estimated spot diameter' when tracking them. The monomer peak did not occur at 1 due to the labelling ratio (1 fluorophore = 6.5 monomers). Over time, the tail of the peak elongated as complexes with higher stoichiometry formed. However, there were always more monomers on the bilayer than complexes, hence the low-stoichiometry peak dominated the high-stoichiometry tail of the histogram. Figure 5.16 is effectively a graphical form of the montage in Figure 4.2A.

5.7 Discussion

This chapter examined the nature of PFO assembly that was observed in the smTIRF images presented in Chapter 4, with the aim of quantifying assembly. First, single assembling complexes were tracked using TrackMate. The intensity of the tracked complexes was then extracted using bespoke code and inbuilt functions in Matlab to fit a Gaussian function to the spots representing the complexes.

A significant effort was made to calibrate the intensity of complexes with their stoichiometry. Several analytical methods were employed and ultimately the

calibration factor seemed internally consistent. The calibration was used to plot the stoichiometry of individual complexes over time. The complexes displayed stoichiometric fluctuations during assembly, and the source of these fluctuations was investigated in order to understand the mechanism of assembly. The fluctuations were attributable to diffusing monomers and small oligomers in the vicinity of the tracked complexes. The governing mechanism of assembly was therefore predicted to be stepwise irreversible addition of monomers, with the exception of the few cases where oligomer-oligomer assembly occurred.

Finally, the kinetics of assembly were determined by synchronising the individual assembly traces. To recap the important values estimated from the assembly data: the timescale for assembly was around 20 seconds for the 2D concentration analysed ($\bar{\rho}_{\text{mon}} = 14\ \mu\text{m}^{-2}$, $\bar{\rho}_{\text{complex}} = 0.03\ \mu\text{m}^{-2}$), the total number of collisions between monomers and complexes was estimated from theory to be $0.60\ \mu\text{m}^{-2}\text{s}^{-1}$, and based on experimentally determined successful collisions only 1 in 400 of the total collisions were successful. SmTIRF combined with the DIB technique provided new insight into the kinetics of assembly and corroborated previous best estimates on the mechanism of assembly [25, 49].

Chapter 6

Conclusions

The foremost aim of this study was to image the assembly of individual CDC pores with high temporal resolution. This aim was met, and as a result the average assembly of a single PFO complex was characterised and its kinetics were outlined. Definitively elucidating the principal mechanism of oligomerisation was another key target. The statistical analysis of assembly traces shed further light on this topic, supporting an irreversible stepwise monomer-addition mechanism, but the mechanism could not be directly discriminated due to the nature of the recorded images.

6.1 Summary of results

The final results concerning the kinetics of CDC assembly were made possible by work described in the early chapters. Chapter 2 described the synthesis of a protein sample that could accurately represent assembly and was suitable for single-molecule imaging. Standard molecular biology techniques were employed to clone the PLY gene to support purification, to express PLY in bacteria, to label it with a fluorophore and to purify it by exploiting various characteristics. The labelled PLY sample was characterised by haemolysis, absorbance and SDS-PAGE.

Chapter 3 detailed the protocol for creating the model-membrane, the DIB, and

for imaging it by smTIRF after addition of labelled protein. The functionality of the protein in a DIB was confirmed by electrophysiological methods and by oSCRs. The ability of the protein to form complexes on a DIB was confirmed by smTIRF in Chapter 4. Chapter 4 also presented images, recorded at millisecond frame-rate, of CDC monomers assembling into complexes. Some of the complexes were characterised for stoichiometry in a demonstration of the subunit counting by photobleaching technique.

Finally, Chapter 5 described several analytical methods to extract information from the videos of assembly. The complexes were tracked and their stoichiometry was estimated based on intensity. Individual complexes were assessed for their diffusion and assembly properties. The fluctuations in the assembly traces were interrogated statistically to determine their origin. The 'off-pathway' case of oligomeric complexes binding together was examined, and finally the kinetics of assembly were measured for a representative average single complex and for the PFO population.

6.2 Interpretation of results

6.2.1 DIBs and smTIRF are powerful techniques

Chapter 2 and a large part of Chapter 3 described the application of established techniques to experiments with CDCs. The first novel finding was the demonstration that CDCs were able to assemble and insert a β-barrel into a DIB, by SCR. The number of functional insertions was less than expected, especially compared to the extent of oligomerisation observed by smTIRF. The most likely reason for the lack of insertions is the fact that experiments were conducted at room temperature rather than 37°C, but this remains to be tested; other explanations include some feature of the DIB, a lower cholesterol content than expected, or a biologically relevant phenomenon whereby very few complexes that reach sufficient stoichiometry for

insertion actually undergo the final membrane penetration step.

Nevertheless, PLY and PFO were proven to be functional in a DIB. This was an essential step for validating the identity of the protein aggregates that assembled in two dimensions on the bilayer as biologically relevant CDC oligomers. Moreover, it supports the use of DIBs for studying CDCs in the future. DIBs have a lot to offer the field of CDCs, primarily because of their capacity for simultaneous electrophysiology, oSCRs and smTIRF imaging of labelled protein. They are also stable and versatile. The results presented herein are evidence that DIBs are a viable choice of bilayer for investigating CDCs.

The functionality and the capture of assembly of CDCs support the diagnostic potential of DIBs. DIBs have proved to be a useful tool for measuring the behaviour of membrane proteins on several occasions [67,100–102,104]; their compatibility with wide-field smTIRF and the facility to create an array of droplet bilayers allows high-throughput measurements [106]. The capture of assembly in this study is pertinent in this respect: the detection of intermediate stoichiometries allows further insight into the effect of any external influence on the CDCs, such as mutations, crosslinking or inhibition by temperature or other molecules, which might subtly affect the rate of oligomerisation.

The introduction of sm-fluorescence to the field of CDC molecular mechanisms seems to be a novel development. The results of this study support the further use of sm-fluorescence as a source of dynamic information, which should be appreciated for a full understanding of CDC mechanisms. Sm-fluorescence is now a well established technique in biophysics; it could potentially open up new avenues in the field of CDCs.

6.2.2 Insight into CDC assembly mechanism and kinetics

The kinetics outlined in this study could benefit from further investigation, but as a first approximation they provide a useful and interesting insight into the dynamic

steps in assembly. Understanding reaction and successful collision rates may be useful in the optimisation of inhibitors of the CDCs. CDCs are commonly referred to as vaccine targets due to their role as primary virulence factors [19, 29, 58, 141, 142]; it is fair to assume that the development or optimisation of inhibitors might be desirable. Furthermore, the rates discussed here may serve as useful references in future studies of CDCs, to compare the authenticity of *in vitro* oligomerisation. The dominating rate constant from the average single-complex assembly curve was $k_{\text{slow}} = 0.05\ \text{s}^{-1}$. This timescale of $1/0.05 = 20$ s might seem long for a molecular process, but is plausible given the large size of CDC complexes: the growing complexes must effectively wait for monomers to arrive at their location.

The results determined from individual assembling complexes are entirely consistent with an irreversible stepwise monomer-addition model of assembly. The amplitude of fluctuations for complexes was consistent with the noise expected of a greater number of fluorophores, and the timescale for fluctuations matched that for diffusing monomers. However, the analysis does not completely rule out reversible monomer addition that was not detected due to a lack of sensitivity; unfortunately monomer dissociation could be masked by non-interacting diffusing monomers.

Other qualitative observations support the irreversible mechanism: it was difficult to find instances of oligomers that did not either persist at the same size or proceed to larger complexes. Once complexes were identified above the level of monomer background, they continued to assemble and did not dissociate. This observation could be explained within reversible assembly if the monomer concentration was sufficiently high, but at a density on the order of $\bar{\rho}_{\text{mon}} = 14\ \mu\text{m}^{-2}$ at the maximum rate of assembly (Section 5.6.3), this explanation is tenuous: the monomers are not so dense that there is permanently a monomer available to join the oligomer. The observation is more plausible within an irreversible assembly mechanism.

The ratio of successful collisions to unsuccessful was found to be 1 in 400. Success

in this context meant that the colliding monomer contributed to the final oligomer. The ratio for PFO supports a different mechanism of assembly to αHL, for which the equivalent ratio was 1 in 10^7 [67]. The higher proportion of successful collisions suggests that the association constant for PFO is significantly higher than for αHL, and is consistent with irreversible assembly for PFO versus reversible assembly for αHL. The number of successful collisions may also depend on temperature.

In summary, though no individual result provides a robust answer to the question of assembly mechanism, the evidence for irreversible assembly is internally consistent.

6.2.3 Comparison with previous findings

Besides the new insight offered by dynamic information, the observations of CDC assembly herein are consistent with previous investigations. The irreversible mechanism has been suggested previously [25, 49], and is expected for a complex that requires many monomers at the same location to facilitate on-pathway ring-shaped pore formation, particularly at low concentration. The efficacy of CDCs at limiting concentration is partially satisfied by their ability to form pores with arcs, but irreversible assembly of the arcs and pores would serve the same purpose.

The mechanism seems inconsistent with αHL based on collision rates, but this is unsurprising given their disparate structures. Under a reversible mechanism αHL only requires 7 subunits to persist in the same location for longer than the timescale for monomer dissociation, an exponentially more challenging feat for 30-50 subunits. Moreover, the potential mechanisms for αHL based on its rapid assembly included an activation step with irreversible monomer addition [67], besides the reversible mechanism.

The distribution of complexes on the bilayer in smTIRF images must be interpreted carefully, because the diffraction limited spots representing the complexes are an order of magnitude larger in diameter than the complexes themselves.

Nonetheless, the general distribution of complexes on the bilayer appears to be consistent with the haphazard arrangement observed by EM [20–22]. Moreover, complexes with effective stoichiometry far exceeding that of a single ring-shaped pore were occasionally detected, consistent with the large multi-arc complexes observed by AFM and EM [22, 25, 27].

Finally, cases of oligomeric complexes binding together were observed, putatively adding a dynamic element to the formation of interlocking arcs or multi-arc/ring complexes, and again consistent with structural data. Such events are relevant to assembly since the complexes were shown to form functional pores [25, 27]. The initial complexes in these cases seemed to have a modal stoichiometry, perhaps suggestive of exhaustion of local monomer concentration or a characteristic collision frequency for assembling complexes. In total, hundreds of individual assembly events were captured in this study, across several protein injection and assembly iterations on different bilayers. The process is not automated yet, but after thorough searching only around 30 oligomer-oligomer assembly events were found. Given the ability of these proteins to form membrane lesions with arcs, presumably to improve their efficacy for a wider range of conditions and concentration, the irregular oligomer-oligomer assembly mechanism appears to be an off-pathway bonus side effect. It will be interesting to see to what extent arcs and multi-arc complexes form functional pores in real cell membranes in a natural environment.

6.3 Outlook

6.3.1 Mathematical modelling of assembly

It has not gone unnoticed that the results presented herein lend themselves favourably to a mathematical model of CDC assembly, as has been offered by others [25]. We have recently developed a detailed model for reversible αHL assembly (Lee et al. [143], in press), and have begun working on an equivalent model for PFO.

(This model is still in the early development stage, hence no results from the model are presented in this thesis.) The PFO model will have to replicate the number of complexes appearing over time, the constant binding of monomers to the bilayer and the average assembly curve for a single complex as a minimum. Moreover, the assembly videos are conducive to a reaction-diffusion type model.

6.3.2 Simultaneous measurements of function and assembly

This thesis focused on smTIRF assembly data, with relatively little attention given to the functional information provided by oSCR. However, the demonstration of assembly capture by smTIRF warrants revisiting oSCR. The simultaneous application of smTIRF and oSCR could yield significant information regarding the time-resolved insertion of the β-barrel. It would be interesting to quantify the delay between stabilised oligomer stoichiometry and membrane penetration. Moreover, with more intricate sm-fluorescence methods such as simultaneous single-molecule Förster resonance energy transfer and oSCR, the insertion of the β-barrel could be detected both structurally and functionally.

6.3.3 New techniques for the study of CDCs

The difficulty in making robust conclusions regarding irreversible assembly, described above, is to some extent inevitable. Any direct observation of monomers assembling into complexes on a bilayer will inherently include both diffusing monomers close to but not interacting with complexes, and monomers joining the complex. Extremely high spatial and temporal resolution would be required to distinguish between these cases, yet high resolution in space and time are not generally compatible. Arguably, a definitive answer to the question of assembly mechanism will require a collection of indirect evidence, potentially including ensemble measurements of artificially synchronised CDCs, rather than direct observation at the single-complex level.

The future study of *in vivo* CDC function is a prime example of where sm-fluorescence could be employed to great effect. Some examples of conventional sm-fluorescence applied to MACPF/CDC function have already been presented, including perforin translocation of granzymes [144] and raft aggregation by LLO [32]. However, the rapidly expanding field of super-resolution has the capacity to resolve dynamic CDC function at the 10 nm scale [66]. Molecular mechanistic details may still be beyond the dynamic range of super-resolution techniques, but CDC-induced cellular effects may not. Super-resolution microscopy is an ideal tool with which to study the location and long-term movements and effects of CDCs in cells: LLO facilitating the internalisation of *L. monocytogenes* or PLY disrupting the integrity of the plasma membrane, for example. It is envisaged that super-resolution microscopy will contribute to future studies of the CDCs.

For future mechanistic studies of dynamic single-complex CDC assembly, a combination of AFM for spatial resolution and smTIRF for temporal resolution seems a promising approach. New instrument development in either of these fields, or the development of new imaging techniques altogether, will hopefully improve our understanding of the dynamic CDC assembly mechanism.

Bibliography

[1] A. P. Heuck, P. C. Moe, and B. B. Johnson, *Cholesterol Binding and Cholesterol Transport Proteins*, ch. The cholesterol-dependent cytolysin family of gram-positive bacterial toxins, pp. 551–577. Springer, 2010.

[2] R. A. Hirst, A. Kadioglu, C. O'callaghan, and P. W. Andrew, "The role of pneumolysin in pneumococcal pneumonia and meningitis," *Clinical & Experimental Immunology*, vol. 138, no. 2, pp. 195–201, 2004.

[3] G. Sierig, C. Cywes, M. R. Wessels, and C. D. Ashbaugh, "Cytotoxic effects of streptolysin O and streptolysin S enhance the virulence of poorly encapsulated group a streptococci.," *Infection and Immunity*, vol. 71, no. 1, pp. 446–455, 2003.

[4] S. K. B. Cassidy and M. X. D. O'Riordan, "More than a pore: the cellular response to cholesterol-dependent cytolysins.," *Toxins*, vol. 5, no. 4, pp. 618–636, 2013.

[5] R. Ramachandran, R. K. Tweten, and A. E. Johnson, "Membrane-dependent conformational changes initiate cholesterol-dependent cytolysin oligomerization and intersubunit β-strand alignment," *Nature Structural & Molecular Biology*, vol. 11, no. 8, pp. 697–705, 2004.

[6] D. L. Stevens and A. E. Bryant, "The role of clostridial toxins in the pathogenesis of gas gangrene.," *Clinical Infectious Diseases*, vol. 35, no. Suppl 1, pp. S93–S100, 2002.

[7] A. P. Heuck and A. E. Johnson, "Pore-forming protein structure analysis in membranes using multiple independent fluorescence techniques," *Cell Biochemistry and Biophysics*, vol. 36, no. 1, pp. 89–101, 2002.

[8] L. A. Shepard, A. P. Heuck, B. D. Hamman, J. Rossjohn, M. W. Parker, K. R. Ryan, A. E. Johnson, and R. K. Tweten, "Identification of a membrane-spanning domain of the thiol-activated pore-forming toxin Clostridium perfringens perfringolysin O: an α-helical to β-sheet transition identified by fluorescence spectroscopy," *Biochemistry*, vol. 37, no. 41, pp. 14563–14574, 1998.

[9] L. A. Shepard, O. Shatursky, A. E. Johnson, and R. K. Tweten, "The mechanism of pore assembly for a cholesterol-dependent cytolysin: formation

of a large prepore complex precedes the insertion of the transmembrane β-hairpins," *Biochemistry*, vol. 39, no. 33, pp. 10284–10293, 2000.

[10] A. P. Heuck, E. M. Hotze, R. K. Tweten, and A. E. Johnson, "Mechanism of membrane insertion of a multimeric β-barrel protein: perfringolysin O creates a pore using ordered and coupled conformational changes," *Molecular Cell*, vol. 6, no. 5, pp. 1233–1242, 2000.

[11] O. Shatursky, A. P. Heuck, L. A. Shepard, J. Rossjohn, M. W. Parker, A. E. Johnson, and R. K. Tweten, "The mechanism of membrane insertion for a cholesterol-dependent cytolysin: a novel paradigm for pore-forming toxins," *Cell*, vol. 99, no. 3, pp. 293–299, 1999.

[12] E. M. Hotze, A. P. Heuck, D. M. Czajkowsky, Z. Shao, A. E. Johnson, and R. K. Tweten, "Monomer-monomer interactions drive the prepore to pore conversion of a β-barrel-forming cholesterol-dependent cytolysin," *Journal of Biological Chemistry*, vol. 277, no. 13, pp. 11597–11605, 2002.

[13] R. W. Harris, P. J. Sims, and R. K. Tweten, "Evidence that Clostridium perfringens theta-toxin induces colloid-osmotic lysis of erythrocytes.," *Infection and Immunity*, vol. 59, no. 7, pp. 2499–2501, 1991.

[14] A. Bernheimer, "Comparative kinetics of hemolysis induced by bacterial and other hemolysins," *Journal of General Physiology*, vol. 30, no. 4, pp. 337–353, 1947.

[15] J. Rossjohn, S. C. Feil, W. J. McKinstry, R. K. Tweten, and M. W. Parker, "Structure of a cholesterol-binding, thiol-activated cytolysin and a model of its membrane form," *Cell*, vol. 89, no. 5, pp. 685–692, 1997.

[16] G. Polekhina, K. S. Giddings, R. K. Tweten, and M. W. Parker, "Insights into the action of the superfamily of cholesterol-dependent cytolysins from studies of intermedilysin," *Proceedings of the National Academy of Sciences*, vol. 102, no. 3, pp. 600–605, 2005.

[17] L. Xu, B. Huang, H. Du, X. C. Zhang, J. Xu, X. Li, and Z. Rao, "Crystal structure of cytotoxin protein suilysin from Streptococcus suis," *Protein & Cell*, vol. 1, no. 1, pp. 96–105, 2010.

[18] J. E. Marshall, B. H. A. Faraj, A. R. Gingras, R. Lonnen, M. A. Sheikh, M. El-Mezgueldi, P. C. E. Moody, P. W. Andrew, and R. Wallis, "The crystal structure of pneumolysin at 2.0 Å resolution reveals the molecular packing of the pre-pore complex.," *Scientific Reports*, vol. 5, p. 13293, 2015.

[19] S. L. Lawrence, S. C. Feil, C. J. Morton, A. J. Farrand, T. D. Mulhern, M. A. Gorman, K. R. Wade, R. K. Tweten, and M. W. Parker, "Crystal structure of Streptococcus pneumoniae pneumolysin provides key insights into early steps of pore formation.," *Scientific Reports*, vol. 5, p. 14352, 2015.

[20] S. Bhakdi, J. Tranum-Jensen, and A. Sziegoleit, "Mechanism of membrane damage by streptolysin-O.," *Infection and Immunity*, vol. 47, no. 1, pp. 52–60, 1985.

[21] P. J. Morgan, S. C. Hyman, O. Byron, P. W. Andrew, T. J. Mitchell, and A. J. Rowe, "Modeling the bacterial protein toxin, pneumolysin, in its monomeric and oligomeric form.," *Journal of Biological Chemistry*, vol. 269, no. 41, pp. 25315–25320, 1994.

[22] A. Olofsson, H. Hebert, and M. Thelestam, "The projection structure of perfringolysin O (Clostridium perfringens θ-toxin)," *FEBS Letters*, vol. 319, no. 1-2, pp. 125–127, 1993.

[23] N. Sekino-Suzuki, M. Nakamura, K.-i. Mitsui, and Y. Ohno-Iwashita, "Contribution of individual tryptophan residues to the structure and activity of θ-toxin (perfringolysin O), a cholesterol-binding cytolysin," *European Journal of Biochemistry*, vol. 241, no. 3, pp. 941–947, 1996.

[24] S. J. Tilley, E. V. Orlova, R. J. Gilbert, P. W. Andrew, and H. R. Saibil, "Structural basis of pore formation by the bacterial toxin pneumolysin," *Cell*, vol. 121, no. 1, pp. 247–256, 2005.

[25] C. Leung, N. V. Dudkina, N. Lukoyanova, A. W. Hodel, I. Farabella, A. P. Pandurangan, N. Jahan, M. P. Damaso, D. Osmanovic, C. F. Reboul, M. A. Dunstone, P. W. Andrew, R. Lonnen, M. Topf, H. R. Saibil, and B. W. Hoogenboom, "Stepwise visualization of membrane pore formation by suilysin, a bacterial cholesterol-dependent cytolysin," *Elife*, vol. 3, p. e04247, 2014.

[26] D. M. Czajkowsky, E. M. Hotze, Z. Shao, and R. K. Tweten, "Vertical collapse of a cytolysin prepore moves its transmembrane β-hairpins to the membrane.," *The EMBO Journal*, vol. 23, no. 16, pp. 3206–3215, 2004.

[27] M. Podobnik, G. Anderluh, M. Dalla Serra, L. Lunelli, M. Marchioretto, M. Zanetti, A. Bavdek, M. Kisovec, and M. M. Cajnko, "Plasticity of listeriolysin O pores and its regulation by pH and unique histidine," *Scientific Reports*, vol. 5, p. 9623, 2015.

[28] A. Mayer-Scholl, R. Hurwitz, V. Brinkmann, M. Schmid, P. Jungblut, Y. Weinrauch, and A. Zychlinsky, "Human neutrophils kill Bacillus anthracis," *PLoS Pathogens*, vol. 1, no. 3, p. e23, 2005.

[29] E. AlonsoDeVelasco, A. F. Verheul, J. Verhoef, and H. Snippe, "Streptococcus pneumoniae: virulence factors, pathogenesis, and vaccines.," *Microbiology and Molecular Biology Reviews*, vol. 59, no. 4, pp. 591–603, 1995.

[30] J. C. Madden, N. Ruiz, and M. Caparon, "Cytolysin-mediated translocation (CMT): a functional equivalent of type III secretion in gram-positive bacteria," *Cell*, vol. 104, no. 1, pp. 143–152, 2001.

[31] N. Magassa, S. Chandrasekaran, and M. G. Caparon, "Streptococcus pyogenes cytolysin-mediated translocation does not require pore formation by streptolysin O," *EMBO Reports*, vol. 11, no. 5, pp. 400–405, 2010.

[32] N. O. Gekara, T. Jacobs, T. Chakraborty, and S. Weiss, "The cholesterol-dependent cytolysin listeriolysin O aggregates rafts via oligomerization," *Cellular Microbiology*, vol. 7, no. 9, pp. 1345–1356, 2005.

[33] B. B. Bonev, R. J. C. Gilbert, P. W. Andrew, O. Byron, and A. Watts, "Structural analysis of the protein/lipid complexes associated with pore formation by the bacterial toxin pneumolysin," *Journal of Biological Chemistry*, vol. 276, no. 8, pp. 5714–5719, 2001.

[34] M. A. Hamon, E. Batsché, B. Régnault, T. N. Tham, S. Seveau, C. Muchardt, and P. Cossart, "Histone modifications induced by a family of bacterial toxins," *Proceedings of the National Academy of Sciences*, vol. 104, no. 33, pp. 13467–13472, 2007.

[35] S. Verherstraeten, E. Goossens, B. Valgaeren, B. Pardon, L. Timbermont, F. Haesebrouck, R. Ducatelle, P. Deprez, K. R. Wade, and R. Tweten, "Perfringolysin O: the underrated Clostridium perfringens toxin?," *Toxins*, vol. 7, no. 5, pp. 1702–1721, 2015.

[36] M. A. Hamon, D. Ribet, F. Stavru, and P. Cossart, "Listeriolysin O: the swiss army knife of Listeria," *Trends in Microbiology*, vol. 20, no. 8, pp. 360–368, 2012.

[37] R. W. Bourdeau, E. Malito, A. Chenal, B. L. Bishop, M. W. Musch, M. L. Villereal, E. B. Chang, E. M. Mosser, R. F. Rest, and W.-J. Tang, "Cellular functions and x-ray structure of anthrolysin O, a cholesterol-dependent cytolysin secreted by Bacillus anthracis," *Journal of Biological Chemistry*, vol. 284, no. 21, pp. 14645–14656, 2009.

[38] E. M. Hotze, E. M. Wilson-Kubalek, J. Rossjohn, M. W. Parker, A. E. Johnson, and R. K. Tweten, "Arresting pore formation of a cholesterol-dependent cytolysin by disulfide trapping synchronizes the insertion of the transmembrane β-sheet from a prepore intermediate," *Journal of Biological Chemistry*, vol. 276, no. 11, pp. 8261–8268, 2001.

[39] P. J. Morgan, S. C. Hyman, A. J. Rowe, T. J. Mitchell, P. W. Andrew, and H. R. Saibil, "Subunit organisation and symmetry of pore-forming, oligomeric pneumolysin," *FEBS Letters*, vol. 371, no. 1, pp. 77–80, 1995.

[40] R. J. Gilbert, J. L. Jiménez, S. Chen, I. J. Tickle, J. Rossjohn, M. Parker, P. W. Andrew, and H. R. Saibil, "Two structural transitions in membrane pore formation by pneumolysin, the pore-forming toxin of Streptococcus pneumoniae," *Cell*, vol. 97, no. 5, pp. 647–655, 1999.

[41] M. A. Dunstone and R. K. Tweten, "Packing a punch: the mechanism of pore formation by cholesterol dependent cytolysins and membrane attack complex/perforin-like proteins," *Current Opinion in Structural Biology*, vol. 22, no. 3, pp. 342–349, 2012.

[42] E. M. Hotze and R. K. Tweten, "Membrane assembly of the cholesterol-dependent cytolysin pore complex," *Biochimica et Biophysica Acta (BBA) - Biomembranes*, vol. 1818, no. 4, pp. 1028–1038, 2012.

[43] A. J. Farrand, S. LaChapelle, E. M. Hotze, A. E. Johnson, and R. K. Tweten, "Only two amino acids are essential for cytolytic toxin recognition of cholesterol at the membrane surface," *Proceedings of the National Academy of Sciences*, vol. 107, no. 9, pp. 4341–4346, 2010.

[44] A. Kacprzyk-Stokowiec, M. Kulma, G. Traczyk, K. Kwiatkowska, A. Sobota, and M. Dadlez, "Crucial role of perfringolysin O D1 domain in orchestrating structural transitions leading to membrane-perforating pores, a hydrogen-deuterium exchange study," *Journal of Biological Chemistry*, vol. 289, no. 41, pp. 28738–28752, 2014.

[45] C. E. Soltani, E. M. Hotze, A. E. Johnson, and R. K. Tweten, "Structural elements of the cholesterol-dependent cytolysins that are responsible for their cholesterol-sensitive membrane interactions," *Proceedings of the National Academy of Sciences*, vol. 104, no. 51, pp. 20226–20231, 2007.

[46] T. Jacobs, M. D. Cima-Cabal, A. Darji, F. J. Méndez, F. Vázquez, A. A. C. Jacobs, Y. Shimada, Y. Ohno-Iwashita, S. Weiss, and R. Juan, "The conserved undecapeptide shared by thiol-activated cytolysins is involved in membrane binding," *FEBS Letters*, vol. 459, no. 3, pp. 463–466, 1999.

[47] K. S. Giddings, J. Zhao, P. J. Sims, and R. K. Tweten, "Human CD59 is a receptor for the cholesterol-dependent cytolysin intermedilysin," *Nature Structural & Molecular Biology*, vol. 11, no. 12, pp. 1173–1178, 2004.

[48] K. J. Dowd, A. J. Farrand, and R. K. Tweten, "The cholesterol-dependent cytolysin signature motif: a critical element in the allosteric pathway that couples membrane binding to pore assembly.," *PLoS Pathogens*, vol. 8, no. 7, p. e1002787, 2012.

[49] E. M. Hotze, E. Wilson-Kubalek, A. J. Farrand, L. Bentsen, M. W. Parker, A. E. Johnson, and R. K. Tweten, "Monomer-monomer interactions propagate structural transitions necessary for pore formation by the cholesterol-dependent cytolysins," *Journal of Biological Chemistry*, vol. 287, no. 29, pp. 24534–24543, 2012.

[50] R. Ramachandran, A. P. Heuck, R. K. Tweten, and A. E. Johnson, "Structural insights into the membrane-anchoring mechanism of a cholesterol-dependent cytolysin," *Nature Structural & Molecular Biology*, vol. 9, no. 11, pp. 823–827, 2002.

[51] R. Ramachandran, R. K. Tweten, and A. E. Johnson, "The domains of a cholesterol-dependent cytolysin undergo a major fret-detected rearrangement during pore formation," *Proceedings of the National Academy of Sciences*, vol. 102, no. 20, pp. 7139–7144, 2005.

[52] K. Mitsui, T. Sekiya, S. Okamura, Y. Nozawa, and J. Hase, "Ring formation of perfringolysin O as revealed by negative stain electron microscopy," *Biochimica et Biophysica Acta (BBA)-Biomembranes*, vol. 558, no. 3, pp. 307–313, 1979.

[53] A. F.-P. Sonnen, J. M. Plitzko, and R. J. Gilbert, "Incomplete pneumolysin oligomers form membrane pores," *Open Biology*, vol. 4, no. 4, 2014.

[54] A. P. Heuck, R. K. Tweten, and A. E. Johnson, "Assembly and topography of the prepore complex in cholesterol-dependent cytolysins," *Journal of Biological Chemistry*, vol. 278, no. 33, pp. 31218–31225, 2003.

[55] R. J. Gilbert, M. Mikelj, M. Dalla Serra, C. J. Froelich, and G. Anderluh, "Effects of MACPF/CDC proteins on lipid membranes," *Cellular and Molecular Life Sciences*, vol. 70, no. 12, pp. 1–16, 2012.

[56] R. G. El-Rachkidy, N. W. Davies, and P. W. Andrew, "Pneumolysin generates multiple conductance pores in the membrane of nucleated cells," *Biochemical and Biophysical Research Communications*, vol. 368, no. 3, pp. 786–792, 2008.

[57] R. J. C. Gilbert, "Inactivation and activity of cholesterol-dependent cytolysins: what structural studies tell us," *Structure*, vol. 13, no. 8, pp. 1097–1106, 2005.

[58] R. Gilbert, *Proteins Membrane Binding and Pore Formation*, vol. 677, ch. Cholesterol-dependent cytolysins, pp. 56–66. Springer, 2010.

[59] C. J. Rosado, A. M. Buckle, R. H. Law, R. E. Butcher, W.-T. Kan, C. H. Bird, K. Ung, K. A. Browne, K. Baran, T. A. Bashtannyk-Puhalovich, N. G. Faux, W. Wong, C. J. Porter, R. N. Pike, A. M. Ellisdon, M. C. Pearce, S. P. Bottomley, J. Emsley, A. I. Smith, J. Rossjohn, E. L. Hartland, I. Voskoboinik, J. A. Trapani, P. I. Bird, M. A. Dunstone, and J. C. Whisstock, "A common fold mediates vertebrate defense and bacterial attack," *Science*, vol. 317, no. 5844, pp. 1548–1551, 2007.

[60] M. A. Hadders, D. X. Beringer, and P. Gros, "Structure of C8α-MACPF reveals mechanism of membrane attack in complement immune defense," *Science*, vol. 317, no. 5844, pp. 1552–1554, 2007.

[61] C. J. Rosado, S. Kondos, T. E. Bull, M. J. Kuiper, R. H. P. Law, A. M. Buckle, I. Voskoboinik, P. I. Bird, J. A. Trapani, J. C. Whisstock, and M. A. Dunstone, "The MACPF/CDC family of pore-forming toxins," *Cellular Microbiology*, vol. 10, no. 9, pp. 1765–1774, 2008.

[62] C. Zheng, N. Heintz, and M. E. Hatten, "Cns gene encoding astrotactin, which supports neuronal migration along glial fibers.," *Science*, vol. 272, no. 5260, pp. 417–419, 1996.

[63] L. M. Stevens, H. G. Frohnhöfer, M. Klingler, and C. Nüsslein-Volhard, "Localized requirement for torso-like expression in follicle cells for development of terminal anlagen of the drosophila embryo," *Nature*, vol. 346, no. 6285, pp. 660–663, 1990.

[64] J.-R. Martin, A. Raibaud, and R. Ollo, "Terminal pattern elements in drosophila embryo induced by the torso-like protein," *Nature*, vol. 367, no. 6465, pp. 741–745, 1994.

[65] N. Kodera, D. Yamamoto, R. Ishikawa, and T. Ando, "Video imaging of walking myosin v by high-speed atomic force microscopy," *Nature*, vol. 468, no. 7320, pp. 72–6, 2010.

[66] M. J. Senior and M. I. Wallace, *MACPF/CDC Proteins - Agents of Defense, Attack and Invasion*, ch. Fluorescence imaging of MACPF/CDC proteins: new techniques and their application, pp. 293–319. Springer, 2014.

[67] J. R. Thompson, B. Cronin, H. Bayley, and M. I. Wallace, "Rapid assembly of a multimeric membrane protein pore," *Biophysical Journal*, vol. 101, no. 11, pp. 2679–2683, 2011.

[68] V. T. Nguyen, Y. Kamio, and H. Higuchi, "Single-molecule imaging of cooperative assembly of γ-hemolysin on erythrocyte membranes," *The EMBO Journal*, vol. 22, no. 19, pp. 4968–4979, 2003.

[69] J. W. Lichtman and J.-A. Conchello, "Fluorescence microscopy," *Nature Methods*, vol. 2, no. 12, pp. 910–919, 2005.

[70] E. M. Stennett, M. A. Ciuba, and M. Levitus, "Photophysical processes in single molecule organic fluorescent probes," *Chemical Society Reviews*, vol. 43, no. 4, pp. 1057–1075, 2014.

[71] M. S. Dillingham and M. I. Wallace, "Protein modification for single molecule fluorescence microscopy," *Organic & Biomolecular Chemistry*, vol. 6, no. 17, pp. 3031–3037, 2008.

[72] R. S. Fischer, Y. Wu, P. Kanchanawong, H. Shroff, and C. M. Waterman, "Microscopy in 3D: a biologist's toolbox," *Trends in Cell Biology*, vol. 21, no. 12, pp. 682–691, 2011.

[73] J. Xiao, *Handbook of Single-Molecule Biophysics*, ch. Single-molecule imaging in live cells, pp. 43–93. Springer, 2009.

[74] C. Würth, M. Grabolle, J. Pauli, M. Spieles, and U. Resch-Genger, "Relative and absolute determination of fluorescence quantum yields of transparent samples," *Nature Protocols*, vol. 8, no. 8, pp. 1535–1550, 2013.

[75] D. M. Shotton, "Confocal scanning optical microscopy and its applications for biological specimens," *Journal of Cell Science*, vol. 94, no. 2, pp. 175–206, 1989.

[76] D. Axelrod, "Cell-substrate contacts illuminated by total internal reflection fluorescence.," *The Journal of Cell Biology*, vol. 89, no. 1, pp. 141–145, 1981.

[77] D. Axelrod, "Total internal reflection fluorescence microscopy in cell biology," *Traffic*, vol. 2, no. 11, pp. 764–774, 2001.

[78] T. Xia, N. Li, and X. Fang, "Single-molecule fluorescence imaging in living cells," *Annual Review of Physical Chemistry*, vol. 64, pp. 459–480, 2013.

[79] M. Fernández-Suárez and A. Y. Ting, "Fluorescent probes for super-resolution imaging in living cells," *Nature Reviews Molecular Cell Biology*, vol. 9, no. 12, pp. 929–943, 2008.

[80] G. Shtengel, J. A. Galbraith, C. G. Galbraith, J. Lippincott-Schwartz, J. M. Gillette, S. Manley, R. Sougrat, C. M. Waterman, P. Kanchanawong, and M. W. Davidson, "Interferometric fluorescent super-resolution microscopy resolves 3D cellular ultrastructure," *Proceedings of the National Academy of Sciences*, vol. 106, no. 9, pp. 3125–3130, 2009.

[81] J. R. Unruh and E. Gratton, "Analysis of molecular concentration and brightness from fluorescence fluctuation data with an electron multiplied ccd camera," *Biophysical Journal*, vol. 95, no. 11, pp. 5385–5398, 2008.

[82] S. E. Gelber, J. L. Aguilar, K. L. Lewis, and A. J. Ratner, "Functional and phylogenetic characterization of vaginolysin, the human-specific cytolysin from gardnerella vaginalis," *Journal of Bacteriology*, vol. 190, no. 11, pp. 3896–3903, 2008.

[83] S. E. Wickham, E. M. Hotze, A. J. Farrand, G. Polekhina, T. L. Nero, S. Tomlinson, M. W. Parker, and R. K. Tweten, "Mapping the intermedilysin-human CD59 receptor interface reveals a deep correspondence with the binding site on CD59 for complement binding proteins c8α and C9," *Journal of Biological Chemistry*, vol. 286, no. 23, pp. 20952–20962, 2011.

[84] P. Mueller, D. O. Rudin, H. T. Tien, and W. C. Wescott, "Methods for the formation of single bimolecular lipid membranes in aqueous solution," *The Journal of Physical Chemistry*, vol. 67, no. 2, pp. 534–535, 1963.

[85] H. Bayley, B. Cronin, A. Heron, M. A. Holden, W. L. Hwang, R. Syeda, J. Thompson, and M. Wallace, "Droplet interface bilayers," *Molecular BioSystems*, vol. 4, no. 12, pp. 1191–1208, 2008.

[86] M. Montal and P. Mueller, "Formation of bimolecular membranes from lipid monolayers and a study of their electrical properties," *Proceedings of the National Academy of Sciences*, vol. 69, no. 12, pp. 3561–3566, 1972.

[87] R. Syeda, M. A. Holden, W. L. Hwang, and H. Bayley, "Screening blockers against a potassium channel with a droplet interface bilayer array," *Journal of the American Chemical Society*, vol. 130, no. 46, pp. 15543–15548, 2008.

[88] G. S. Pulcu, E. Mikhailova, L.-S. Choi, and H. Bayley, "Continuous observation of the stochastic motion of an individual small-molecule walker," *Nature Nanotechnology*, vol. 10, no. 1, pp. 76–83, 2015.

[89] D. Rodriguez-Larrea and H. Bayley, "Multistep protein unfolding during nanopore translocation," *Nature Nanotechnology*, vol. 8, no. 4, pp. 288–295, 2013.

[90] M. Tanaka and E. Sackmann, "Polymer-supported membranes as models of the cell surface," *Nature*, vol. 437, no. 7059, pp. 656–663, 2005.

[91] N. Monteiro, A. Martins, R. L. Reis, and N. M. Neves, "Liposomes in tissue engineering and regenerative medicine," *Journal of The Royal Society Interface*, vol. 11, no. 101, 2014.

[92] A. A. Brian and H. M. McConnell, "Allogeneic stimulation of cytotoxic T cells by supported planar membranes," *Proceedings of the National Academy of Sciences*, vol. 81, no. 19, pp. 6159–6163, 1984.

[93] P. Bartsch, C. Walter, P. Selenschik, A. Honigmann, and R. Wagner, "Horizontal bilayer for electrical and optical recordings," *Materials*, vol. 5, no. 12, pp. 2705–2730, 2012.

[94] A. D. Bangham, M. M. Standish, and J. C. Watkins, "Diffusion of univalent ions across the lamellae of swollen phospholipids," *Journal of Molecular Biology*, vol. 13, no. 1, pp. 238–252, 1965.

[95] A. Kunze, M. Bally, F. Höök, and G. Larson, "Equilibrium-fluctuation-analysis of single liposome binding events reveals how cholesterol and ca2+ modulate glycosphingolipid trans-interactions.," *Scientific Reports*, vol. 3, p. 1452, 2013.

[96] D. W. Tank, C. Miller, and W. W. Webb, "Isolated-patch recording from liposomes containing functionally reconstituted chloride channels from torpedo electroplax.," *Proceedings of the National Academy of Sciences*, vol. 79, no. 24, pp. 7749–7753, 1982.

[97] M. Watanabe, T. Tomita, and T. Yasuda, "Membrane-damaging action of staphylococcal alpha-toxin on phospholipid-cholesterol liposomes," *Biochimica et Biophysica Acta (BBA) - Biomembranes*, vol. 898, no. 3, pp. 257–265, 1987.

[98] F. G. Van der Goot, F. Pattus, K. R. Wong, and J. T. Buckley, "Oligomerization of the channel-forming toxin aerolysin precedes insertion into lipid bilayers," *Biochemistry*, vol. 32, no. 10, pp. 2636–2642, 1993.

[99] S. Leptihn, O. K. Castell, B. Cronin, E.-H. Lee, L. C. M. Gross, D. P. Marshall, J. R. Thompson, M. Holden, and M. I. Wallace, "Constructing droplet interface bilayers from the contact of aqueous droplets in oil.," *Nature Protocols*, vol. 8, no. 6, pp. 1048–1057, 2013.

[100] J. R. Thompson, A. J. Heron, Y. Santoso, and M. I. Wallace, "Enhanced stability and fluidity in droplet on hydrogel bilayers for measuring membrane protein diffusion," *NanoLetters*, vol. 7, no. 12, pp. 3875–3878, 2007.

[101] S. Huang, M. Romero-Ruiz, O. K. Castell, H. Bayley, and M. I. Wallace, "High-throughput optical sensing of nucleic acids in a nanopore array," *Nature Nanotechnology*, vol. 10, no. 11, pp. 986–991, 2015.

[102] A. J. Heron, J. R. Thompson, B. Cronin, H. Bayley, and M. I. Wallace, "Simultaneous measurement of ionic current and fluorescence from single protein pores," *Journal of the American Chemical Society*, vol. 131, no. 5, pp. 1652–1653, 2009.

[103] E. E. Weatherill and M. I. Wallace, "Combining single-molecule imaging and single-channel electrophysiology," *Journal of Molecular Biology*, vol. 427, no. 1, pp. 146–157, 2015.

[104] S. Leptihn, J. R. Thompson, J. C. Ellory, S. J. Tucker, and M. I. Wallace, "In vitro reconstitution of eukaryotic ion channels using droplet interface bilayers," *Journal of the American Chemical Society*, vol. 133, no. 24, pp. 9370–9375, 2011.

[105] G. de Wit, J. S. Danial, P. Kukura, and M. I. Wallace, "Dynamic label-free imaging of lipid nanodomains," *Proceedings of the National Academy of Sciences*, vol. 112, no. 40, pp. 12299–12303, 2015.

[106] O. K. Castell, J. Berridge, and M. I. Wallace, "Quantification of membrane protein inhibition by optical ion flux in a droplet interface bilayer array," *Angewandte Chemie International Edition*, vol. 51, no. 13, pp. 3134–3138, 2012.

[107] B. M. Venkatesan and R. Bashir, "Nanopore sensors for nucleic acid analysis," *Nature Nanotechnology*, vol. 6, no. 10, pp. 615–624, 2011.

[108] S. Gräslund, P. Nordlund, J. Weigelt, J. Bray, O. Gileadi, S. Knapp, U. Oppermann, C. Arrowsmith, R. Hui, and J. Ming, "Protein production and purification," *Nature Methods*, vol. 5, no. 2, pp. 135–146, 2008.

[109] J. M. Berg, J. L. Tymoczko, and L. Stryer, *Biochemistry.* W H Freeman, 2002.

[110] F. K. Saunders, T. J. Mitchell, J. A. Walker, P. W. Andrew, and G. J. Boulnois, "Pneumolysin, the thiol-activated toxin of Streptococcus pneumoniae, does not require a thiol group for in vitro activity.," *Infection and Immunity*, vol. 57, no. 8, pp. 2547–2552, 1989.

[111] G. J. Boulnois, J. C. Paton, T. J. Mitchell, and P. W. Andrew, "Structure and function of pneumolysin, the multifunctional, thiol-activated toxin of Streptococcus pneumoniae," *Molecular Microbiology*, vol. 5, no. 11, pp. 2611–2616, 1991.

[112] A. S. Solovyova, M. Nöllmann, T. J. Mitchell, and O. Byron, "The solution structure and oligomerization behavior of two bacterial toxins: pneumolysin and perfringolysin O," *Biophysical Journal*, vol. 87, no. 1, pp. 540–552, 2004.

[113] J. S. Braun, O. Hoffmann, M. Schickhaus, D. Freyer, E. Dagand, D. Bermpohl, T. J. Mitchell, I. Bechmann, and J. R. Weber, "Pneumolysin causes neuronal cell death through mitochondrial damage," *Infection and Immunity*, vol. 75, no. 9, pp. 4245–4254, 2007.

[114] R. J. C. Gilbert, J. Rossjohn, M. W. Parker, R. K. Tweten, P. J. Morgan, T. J. Mitchell, N. Errington, A. J. Rowe, P. W. Andrew, and O. Byron, "Self-interaction of pneumolysin, the pore-forming protein toxin of Streptococcus pneumoniae," *Journal of Molecular Biology*, vol. 284, no. 4, pp. 1223–1237, 1998.

[115] M. Cooper, A. Ebner, M. Briggs, M. Burrows, N. Gardner, R. Richardson, and R. West, "Cy3B^{TM}: improving the performance of cyanine dyes," *Journal of Fluorescence*, vol. 14, no. 2, pp. 145–150, 2004.

[116] Y. Kim, S. O. Ho, N. R. Gassman, Y. Korlann, E. V. Landorf, F. R. Collart, and S. Weiss, "Efficient site-specific labeling of proteins via cysteines," *Bioconjugate Chemistry*, vol. 19, no. 3, pp. 786–791, 2008.

[117] L. D. Nelson, A. E. Johnson, and E. London, "How interaction of perfringolysin O with membranes is controlled by sterol structure, lipid structure, and physiological low pH: insights into the origin of perfringolysin O-lipid raft interaction," *Journal of Biological Chemistry*, vol. 283, no. 8, pp. 4632–4642, 2008.

[118] J. J. Flanagan, R. K. Tweten, A. E. Johnson, and A. P. Heuck, "Cholesterol exposure at the membrane surface is necessary and sufficient to trigger perfringolysin O binding," *Biochemistry*, vol. 48, no. 18, pp. 3977–3987, 2009.

[119] C. Chen, S. W. Smye, M. P. Robinson, and J. A. Evans, "Membrane electroporation theories: a review," *Medical and Biological Engineering and Computing*, vol. 44, no. 1-2, pp. 5–14, 2006.

[120] H. Lindsey, N. O. Petersen, and S. I. Chan, "Physicochemical characterization of 1, 2-diphytanoyl-sn-glycero-3-phosphocholine in model membrane systems," *Biochimica et Biophysica Acta (BBA)-Biomembranes*, vol. 555, no. 1, pp. 147–167, 1979.

[121] B. B. Johnson, P. C. Moe, D. Wang, K. Rossi, B. L. Trigatti, and A. P. Heuck, "Modifications in perfringolysin O domain 4 alter the cholesterol concentration threshold required for binding," *Biochemistry*, vol. 51, no. 16, pp. 3373–3382, 2012.

[122] L. A. Campos, J. Liu, X. Wang, R. Ramanathan, D. S. English, and V. Muñoz, "A photoprotection strategy for microsecond-resolution single-molecule fluorescence spectroscopy," *Nature Methods*, vol. 8, no. 2, pp. 143–146, 2011.

[123] A. Small and S. Stahlheber, "Fluorophore localization algorithms for super-resolution microscopy," *Nature Methods*, vol. 11, no. 3, pp. 267–279, 2014.

[124] J. D. Knight, M. G. Lerner, J. G. Marcano-Velázquez, R. W. Pastor, and J. J. Falke, "Single molecule diffusion of membrane-bound proteins: window into lipid contacts and bilayer dynamics," *Biophysical Journal*, vol. 99, no. 9, pp. 2879–2887, 2010.

[125] S. Ramadurai, A. Holt, V. Krasnikov, G. van den Bogaart, J. A. Killian, and B. Poolman, "Lateral diffusion of membrane proteins," *Journal of the American Chemical Society*, vol. 131, no. 35, pp. 12650–12656, 2009.

[126] S. Tilley and H. Saibil, "The mechanism of pore formation by bacterial toxins," *Current Opinion in Structural Biology*, vol. 16, no. 2, pp. 230–236, 2006.

[127] K. S. Giddings, A. E. Johnson, and R. K. Tweten, "Redefining cholesterol's role in the mechanism of the cholesterol-dependent cytolysins," *Proceedings of the National Academy of Sciences*, vol. 100, no. 20, pp. 11315–11320, 2003.

[128] M. H. Ulbrich and E. Y. Isacoff, "Subunit counting in membrane-bound proteins," *Nature Methods*, vol. 4, no. 4, pp. 319–321, 2007.

[129] M. C. Leake, J. H. Chandler, G. H. Wadhams, F. Bai, R. M. Berry, and J. P. Armitage, "Stoichiometry and turnover in single, functioning membrane protein complexes," *Nature*, vol. 443, no. 7109, pp. 355–358, 2006.

[130] S. K. Das, M. Darshi, S. Cheley, M. I. Wallace, and H. Bayley, "Membrane protein stoichiometry determined from the step-wise photobleaching of dye-labelled subunits," *ChemBioChem*, vol. 8, no. 9, pp. 994–999, 2007.

[131] M. A. Baker, N. Rojko, B. Cronin, G. Anderluh, and M. I. Wallace, "Photobleaching reveals heterogeneous stoichiometry for equinatoxin ii oligomers," *ChemBioChem*, vol. 15, no. 14, pp. 2139–2145, 2014.

[132] M. J. Saxton and K. Jacobson, "Single-particle tracking: applications to membrane dynamics," *Annual Review of Biophysics and Biomolecular Structure*, vol. 26, no. 1, pp. 373–399, 1997.

[133] K. Jaqaman, D. Loerke, M. Mettlen, H. Kuwata, S. Grinstein, S. L. Schmid, and G. Danuser, "Robust single-particle tracking in live-cell time-lapse sequences," *Nature Methods*, vol. 5, no. 8, pp. 695–702, 2008.

[134] C. A. Schneider, W. S. Rasband, and K. W. Eliceiri, "NIH image to imagej: 25 years of image analysis," *Nature Methods*, vol. 9, no. 7, pp. 671–675, 2012.

[135] J. Schindelin, I. Arganda-Carreras, E. Frise, V. Kaynig, M. Longair, T. Pietzsch, S. Preibisch, C. Rueden, S. Saalfeld, B. Schmid, J.-Y. Tinevez, D. J. White, V. Hartenstein, K. Eliceiri, P. Tomancak, and A. Cardona, "Fiji: an open-source platform for biological-image analysis," *Nature Methods*, vol. 9, no. 7, pp. 676–682, 2012.

[136] J. C. Waters and T. Wittmann, *Quantitative Imaging in Cell Biology*, vol. 123, ch. Concepts in quantitative fluorescence microscopy, pp. 1–18. Academic Press, 2014.

[137] Y. Subburaj, K. Cosentino, M. Axmann, E. Pedrueza-Villalmanzo, E. Hermann, S. Bleicken, J. Spatz, and A. J. García-Sáez, "Bax monomers form dimer units in the membrane that further self-assemble into multiple oligomeric species," *Nature Communications*, vol. 6, p. 8042, 2015.

[138] J. Canny, "A computational approach to edge detection," *Pattern Analysis and Machine Intelligence, IEEE Transactions on*, vol. PAMI-8, no. 6, pp. 679–698, 1986.

[139] Q. Lin and E. London, "Transmembrane protein (perfringolysin O) association with ordered membrane domains (rafts) depends upon the raft-associating properties of protein-bound sterol," *Biophysical Journal*, vol. 105, no. 12, pp. 2733–2742, 2013.

[140] J. Keizer, "Diffusion effects on rapid bimolecular chemical reactions," *Chemical Reviews*, vol. 87, no. 1, pp. 167–180, 1987.

[141] P. Neeson, Z. K. Pan, and Y. Paterson, "Listeriolysin O is an improved protein carrier for lymphoma immunoglobulin idiotype and provides systemic protection against 38c13 lymphoma," *Cancer Immunology, Immunotherapy*, vol. 57, no. 4, pp. 493–505, 2008.

[142] R. Cockeran, R. Anderson, and C. Feldman, "Pneumolysin as a vaccine and drug target in the prevention and treatment of invasive pneumococcal disease," *Archivum Immunologiae et Therapiae Experimentalis - English Edition*, vol. 53, no. 3, pp. 189–198, 2005.

[143] A. A. Lee, M. J. Senior, M. I. Wallace, T. E. Woolley, and I. M. Griffiths, "Dissecting the self-assembly kinetics of multimeric pore-forming toxins," *Journal of The Royal Society Interface*, In press.

[144] J. Thiery, D. Keefe, S. Boulant, E. Boucrot, M. Walch, D. Martinvalet, I. S. Goping, R. C. Bleackley, T. Kirchhausen, and J. Lieberman, "Perforin pores in the endosomal membrane trigger the release of endocytosed granzyme B into the cytosol of target cells," *Nature Immunology*, vol. 12, no. 8, pp. 770–777, 2011.